

E-525

Pion-Nuclei Interactions at 200 GeV

by

Myau-Yin Lee

A dissertation submitted in partial fulfillment
of the requirements for the degree of

Doctor of Philosophy

University of Washington

1978

Approved by _____
(Chairperson of Supervisory Committee)

Program Authorized
to Offer Degree _____

Date _____

AC:OF
1-614

UNIVERSITY OF WASHINGTON

March 20, 1978
Date: _____

We have carefully read the dissertation entitled Pion-Nuclei Interactions at
200 GeV

submitted by
Myau-Yin Lee in partial fulfillment of
the requirements of the degree of Doctor of Philosophy
and recommend its acceptance. In support of this recommendation we present the following
joint statement of evaluation to be filed with the dissertation.

Myau-Yin Lee has completed an experimental investigation of nuclear interactions of very high energy pions in heavy nuclei targets. The experiments, conducted in the Fermi National Accelerator Laboratory 200 Gev pion beam, were made with unusually small targets (10 to 20 micrometers in diameter) embedded in nuclear track emulsions. The small targets made it possible to detect all of the charged particles emitted in pion collisions with very pure heavy elements. This experiment represents the first time that, with the exception of heavy nuclear recoil fragments, all of the charged particles emitted in high energy pion collisions could be detected in targets as heavy as tungsten.

The angular distributions and multiplicities of high energy charged particles, n_s , and lower energy evaporation and recoil nuclei, N_h , were measured for targets of tungsten and chromium and compared with earlier results in hydrogen and the nuclear track emulsion mixture of elements. The linearity of $\langle n_s \rangle$ as a function of N_h was established for pure heavy elements at pion energies of high energy. The angular distribution of emitted shower particles shows that corrections have to be made in earlier counter experiments having poor efficiencies for large angle particles. Evidence for a more complicated structure in the angular distribution was found in earlier experiments with nuclear emulsion targets. In this thesis it is shown that the effect is associated with the nature of the interaction and not due to observations with targets consisting of mixtures of elements.

Angular distributions and multiplicity distributions were compared with current theories. Since theoretical models for collisions in heavy nuclei are in a state of development at the present time, it is difficult to make definitive comparisons with experiment. However, the thesis results are in agreement with

the modified form of the Energy Flux Model as well as the improved form of the Two Component and Multiperipheral Models, and the recent form with the Parton Model. The results serve to direct attention to aspects of theory which are incorrect and those which need to be changed.

Ms. Lee's thesis reports new results and can be considered a worthy contribution to the understanding of high energy particle physics.

DISSERTATION READING COMMITTEE:

Jere J. Lord

Jere J. Lord

Joseph H. Weis

Joseph Weis

Kenneth L. Young

Kenneth Young

DOCTORAL DISSERTATION

In presenting this dissertation in partial fulfillment of the requirements for the Doctoral degree at the University of Washington, I agree that the Library shall make its copies freely available for inspection. I further agree that extensive copying of this dissertation is allowable only for scholarly purposes. Requests for copying or reproduction of this dissertation may be referred to University Microfilms, 300 North Zeeb Road, Ann Arbor, Michigan 48106, to whom the author has granted "the right to reproduce and sell (a) copies of the manuscript in microform and/or (b) printed copies of the manuscript made from microform."

Signature _____

Date _____

University of Washington

Abstract

PION-NUCLEI INTERACTIONS AT 200 GeV

by Myau-Yin Lee

Chairperson of the Supervisory Committee:

Professor Jere J. Lord
Department of Physics

Tungsten and chromium microgranules embedded in emulsion plates were used as targets in exposure to 200 GeV pion beams at Fermi National Accelerator Laboratory.

The multiplicity distributions of the resulting interactions are found to be broader than the Poisson distribution and are also found to exhibit scaling. The relation between the multiplicity ratio R and the average number of collisions \bar{v} falls onto the line $R = \frac{1}{2} + \frac{1}{2} \bar{v}$, which favors the predictions of the modified energy flux cascade and two-phase models as well as the parton models. Average multiplicity is also found to be linearly dependent on the number of heavy tracks.

Comparison of the angular distributions among different sizes of target shows agreement with predictions of the multiperipheral production model.

Two-particle rapidity correlations are strong in the target fragmentation regions. The characteristics of the two-dimensional contour plot of the correlation function

$R(y_1, y_2)$ are very different from those of hadron-hadron interactions; this favors the interaction mechanism proposed in the parton model of N. N. Nikolaev.

TABLE OF CONTENTS

1. Introduction,	1
2. Literature Survey--Review of Hadrodynamics and some General Features of Multiparticle Production.	3
(I) Single-particle inclusive interactions.	4
1: Energy and Transverse Momentum	5
2: Rapidity Distribution and Angular Distribution	6
3: Inclusive Cross Section	11
4: Limiting Fragmentation and Scaling Hypothesis	13
(A) Limiting Fragmentation Hypo- thesis	13
(B) Scaling Hypothesis	15
(C) Discussion	16
5: Multiplicity	17
(II) Two-Particle Rapidity Correlation	20
1: Definition	20
2: Short Range Correlation (SRC) Hypothesis	22
3: General Discussion: Data and Models	24
(A) Data	24
(B) Models	27

3. Theory of Hadron-Nucleus Interaction	34
(I) Models with Independent Collisions with Constituents	35
1: Several Phases Models	35
(A) Energy Flux Cascade (EFC) Model	36
(B) Two-Phase Model (TPM)	41
(C) A Third Model by J. Babbecki <u>et al.</u>	42
2: Multiperipheral Production Model (MPM)	44
3: Parton Models	50
(A) N. N. Nikolaev <u>et al.</u>	51
(B) S. J. Brodsky <u>et al.</u>	52
(II) Models Using Coherent Interactions with Nucleus	56
1: Coherent Tube Model	56
2: A Coherent Interaction Model by G. Bialkowski <u>et al.</u>	60
(III) Some Comments on Models	61
4. Experimental Procedures	67
(I) Research with Nuclear Emulsions	67
1: Introduction	67
2: Chemical Composition and the Mechanism of Track Formation.	68
3: Ionization Loss of Charged Particles and Restricted Ionization Loss in Emulsion	70
4: Special Features	71

(II)	Apparatus Set-Up	73
1:	Size and Material Used	74
2:	Technique	77
3:	Exposure to the 200 GeV π^- Beam	79
4:	Grid Printing and Developing the Plates	79
(III)	Scanning and Measurement	80
1:	Events	80
2:	Scanning	82
3:	Measurement	84
4:	Shrinkage Factor	85
(IV)	Methodology	86
1:	Event Selection	86
2:	Efficiency	87
5.	Results	93
(I)	Multiplicity Distribution	93
1:	Shower Particle Multiplicity	93
2:	Scaled Multiplicity	95
3:	R vs. \bar{v}	103
4:	Heavy Track Particles	107
(II)	Angular Distribution	115
(III)	Two-Particle Pseudo-Rapidity Correlation	121
(IV)	Conclusion	129

BIBLIOGRAPHY	134
APPENDIX I: Measurement of the Tracks	141
APPENDIX II: Scanning Efficiency	147

LIST OF FIGURES

1. A simple picture of the constant cross section contours in phase space at different energies E_1, E_2, E_3 . 7
2. (a) Typical rapidity distribution for hadron-hadron (h-h) collisions at high energy. Regions A, B, and C are
 - A: target fragmentation region
 - B: pionization region
 - C: projectile fragmentation region.

L is the fragmentation length.

(b) Pseudo-rapidity distribution in the CM system at different ISR energies. Solid lines are the fits for data points. 10
3. Total cross section for π^+p , K^+p , $p\bar{p}$, and $\bar{p}p$ interactions. The solid curves are the cross sections predicted by H. Cheng et al. (44). 12
4. Two dimensional plot of $R(y_1, y_2)$: (a) at 102 GeV; (b) at 400 GeV (FNAL data) and (c) at 11 + 11 and (d) at 31 + 31 GeV (ISR data). 25

5. Cluster production in hadronic interactions; each cluster decays into K particles (a) multiperipheral cluster production; (b) diffractive fragmentation production. 29

6. (a) The slices of energy flux (for example, 3) in EFC model for an ideal h-h rapidity distribution. The slice with energy corresponding to a hadron can interact with the downstream nucleons and form the energy flux with rapidity distribution similar to that of h-h interactions.

(b) Rapidity distributions predicted by Gottfried's EFC model with different incident energies E_1 (solid line) and E_2 (dash line), where $E_2 > E_1$.

(c) A comparison of Gottfried's EFC model (solid line) and the modified EFC model (dash line). 38

7. (a) The hadronic matter slices for an ideal rapidity distribution of h-h interactions. The shaded area is a slice of excited hadronic matter acting as a hadron with rapidity length βY and interaction cross section

7(a) $\beta\sigma_t^{\text{inel}}$.

(b) Rapidity distribution for h-A interactions predicted by TPM: n is the number of slices dividing the excited hadronic matter of the first h-h interaction in the target nucleus.

43

8 Predictions of rapidity distribution by Babecki et al.

(a) For different sizes of target (proton, A_1 , and A_2 , where $A_2 > A_1$), target fragmentation rises as the increase of target size; the two-unit difference from projectile rapidity remains unchanged.

(b) For different incident energies, where $E_2 > E_1$.

45

9. The time-space picture for hadronic interaction in MPM.

(a) In h-h interactions, secondary particles are emitted with energies $E_{i+1} = \frac{1}{c} E_i$, where c is a constant.

(b) In h-A interactions, a second chain can be emitted well before the interaction with

9(b) target nucleons and form the nuclear cascade. R_0 is the interaction length. 47

10. Predictions of MPM about rapidity distributions for h-A interactions (solid curve) compared with h-h interactions (dash curve). A larger increase at the target fragmentation region is due to rescattering. Depletion is shown in the projectile fragmentation region. 49

11. The multiplicity ratio R predicted by the parton model of N. N. Nikolaev. 53

12. An illustration for h-A interactions (with 3 collisions in the target nucleus) of the model proposed by Brodsky et al. Rapidities of collisions y_i are uniformly distributed in the central region of a typical h-h rapidity range.

(a) $\langle \text{Target-produced particle multiplicity} \rangle$
 $= \frac{\bar{v}}{2} n_c$.

(b) $\langle \text{Projectile-produced particle multiplicity} \rangle = \frac{\bar{v}}{\bar{v}+1} n_c$.

(c) Total multiplicity = $(\frac{\bar{v}}{2} + \frac{\bar{v}}{\bar{v}+1}) n_c$

12(c) in the central region.	55
13. In CTM, the incident hadron interacts with an array of nucleons lying on its path coherently as a hadron- "hadron" interaction at energy $A^{\frac{1}{3}}E$.	58
14. Predictions of CTM about rapidity distributions	
(a) For different sizes of target, where $A_2 > A_1$, the rapidity distribution rises and expands toward the direction of target fragmentation.	
(b) For different energies, where $E_2 > E_1$, the rapidity distribution expands toward the direction of projectile fragmentation.	59
15. The ratio of the grain density to that at the minimum of ionization loss, derived from K5 emulsion measurements.	72
16. Nuclear emulsion plates with embedded metal granules.	75
17. A picture of a typical pion-nucleus interaction in nuclear emulsion plates.	81
18. Histograms of multiplicity distributions for (a) π -W and (b) π -Cr interactions at 200 GeV.	94

19. Scaled multiplicity distributions, where
 $z = \frac{n_s}{\langle n_s \rangle}$, and $\psi(z) = \langle n_s \rangle p_n$. The solid line is the least square fit of Slattery type function for π -p data, and the dash line is for the W and Cr data from this experiment.

96

20. A comparison of least square fit of Slattery type function for π -p (solid line) and π -nucleus from this experiment (dash line) with Slattery's function (dot line) for p-p interactions.

97

21. Data and linear least fit of data for D vs. $\langle n_s \rangle$ where

$$D = \sqrt{(\langle n_s^2 \rangle - \langle n_s \rangle^2)}$$

π -W and π -Cr data from this experiment is indicated. Others are π -p and π -nucleus data at different energies compiled by W. Busza and Wróblewski (8).

102

22. R vs. \bar{v} : data are shown as indicated. The lines labeled with functions of \bar{v} are predictions from various models, while the line B is the best fit of data from the

22.	counter experiment (2).	106
23.	Histograms of N_h -distributions for (a) π -W and (b) π -Cr interactions at 200 Gev.	109
24.	$\langle n_s \rangle$ vs. N_h data of π -W, π -Cr and π -Em (20) at 200 GeV are as indicated. The linear least square fits for π -Em, π -W and P-Em (19) interaction data are included for comparison.	111
25.	A comparison of $\langle n_s \rangle$ vs. N_h for different projectiles and different targets at different energies, as indicated (19,1,3).	113
26.	Pseudo-rapidity distribution, normalized to that of one event, for (a) π -W and (b) π -Cr interactions at 200 GeV.	116
27.	Comparison of pseudo-rapidity distributions at 200 GeV with the variation of target sizes: π -p (22) and π -Em (21) data are as indicated; the solid histogram is for π -Cr interactions, and the dash histogram is for π -W interactions.	119
28.	Pseudo-rapidity distributions for different ranges of N_h (a) $N_h = 0 \sim 1$;	

28. (b) $N_h = 2 \sim 10$; (c) $N_h \geq 11$ for π -W interactions at 200 GeV. Areas are normalized to the multiplicity for one event. 122

29. Pseudo-rapidity distributions for different ranges of N_h (a) $N_h = 0 \sim 1$; (b) $N_h = 2 \sim 10$; (c) $N_h \geq 11$, for π -Cr interactions at 200 GeV. Areas are normalized to the multiplicity for one event. 123

30. Correlation function $R(\eta_1, \eta_1)$ at several different fixed η_1 for π -W and π -Cr interactions at 200 GeV in the CM system. 125

31. Two-dimensional contour plot of the correlation function $R(\eta_1, \eta_2)$ for π -W interactions at 200 GeV in the CM system. 126

32. Two-dimensional contour plot of the correlation function $R(\eta_1, \eta_2)$ for π -Cr interactions at 200 GeV in the CM system. 127

FIGURES IN APPENDICES

1. The spatial measurement of the primary and a given track. 142

2. The double measurement of tracks in the region where emulsion is very curved:

2. (a) measured with a reference track L' ;
(b) after transform to a new frame where
 L' is considered as a coordinate.

145

LIST OF TABLES

I. Summary of the scanning efficiencies for first and second scannings.	90
II. Coefficients of the least square fit of the functions for scaled multiplicity distribution (after Slattery)	
$\psi(z) = (Az + Bz^3 + Cz^5 + Dz^7) \exp(-EZ)$	
for π -nucleus and π -p interactions at	
200 GeV.	99
III. Some measurements corrected by scanning efficiency.	101
IV. Comparison of $\langle N_h \rangle$ for hadron-nucleus interactions.	110
V. Coefficients of linear least square fit of data regarding	114
$\langle n_s \rangle$ vs. N_h : $\langle n_s \rangle = a + bN_h$	

ACKNOWLEDGEMENTS

I would like to express my deep appreciation to Professor Jere J. Lord, my adviser, for his support and encouragement during my graduate career. His active interest and participation are the major factors in any success we have obtained.

Dr. Joseph Florian contributed his help in preparing the emulsion plates for this experiment. I also benefited from numerous fruitful discussions, as well as enthusiastic assistance and patient guidance, from Dr. James Martin and Dr. Jeffery Wilkes. Similar debts are also owed to Dr. Steven Anderson, Terry Koss, and Robert Rosenbladt.

I also thank Professor Joseph Weis and Professor Kenneth Young for their careful reading of, and many suggestions about, this dissertation.

In addition, Honorine Tepfer devoted much time and energy to the measuring work; and Richard Brzustowicz and James Crisp helped in the scanning.

Finally, I would like to thank my family for their support and encouragement during my student years.

This experiment was supported by the United States Department of Energy and was carried out at the Fermi National Accelerator Laboratory.

This dissertation was prepared and typed with the assistance of Richard Brzustowicz.

CHAPTER I:
INTRODUCTION

This experiment uses nuclear emulsion techniques and accelerator beams to illuminate pion-nucleus interactions at 200 GeV. This is one of a series of experiments which are themselves a branch of an ongoing research program of the Cosmic Ray Laboratory at the University of Washington --a program designed for the investigation of the process of multiparticle production in hadronic interactions.

In high energy hadronic interactions, the nucleus is often regarded as a microscopic laboratory; and it is hoped that a study of hadron-nucleus interactions will reveal more information about the multiparticle production process in hadronic interaction. To understand the production mechanisms, it is important to investigate the intranuclear cascade process as a function of atomic mass A of the target and the incident energy E of the projectile. It is also important to investigate the possible variations caused by the difference in projectile type, in order to study the differences in interaction characteristics. This series of experiments is specifically designed to meet this objective. Using accelerator pion and proton beams, at energies from 200 GeV up to the highest available at Fermi National Accelerator Laboratory (FNAL),

makes it possible to control for beam energy and beam type. The emulsion plate, containing embedded microgranules of several metals, provides a target of known element and precise nuclear size.

In this experiment, several target nuclei in emulsion plates are exposed to π^- beams at 200 GeV. After exposure and development, plates with ^{52}Cr and ^{184}W as targets are subjected to scanning for hadronic multiparticle production events occurring in the metal granules. With the help of the fine spatial resolution and 4π sensitivity of the nuclear emulsion, events are examined and analyzed statistically with respect to multiplicity distributions, angular distributions, and the two-particle correlation of secondary relativistic particles.

This experiment not only accumulates data, but also compares its results with earlier experiments--both previous proton-nucleus experiments in this series (see reference (1), Chapter 5), and results from elsewhere about hadron-nucleus interactions. All of these procedures are aimed at indicating the most promising models of, and thus helping to establish a theory for, the interaction mechanism.

CHAPTER II:

Literature Survey--Review of Hadrodynamics and Some General Features of Multiparticle Production.

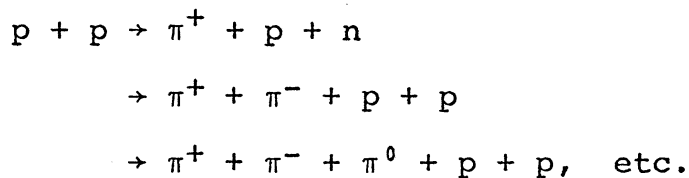
In high energy multiparticle production, the number of secondary particles produced in hadron-hadron interactions increases rapidly with the energy and, thus, as the energy increases, the final state of the reaction becomes very complicated. Data on high energy interactions come mostly from the accelerator at Fermi National Accelerator Laboratory (FNAL) and the Interacting Storage Ring (ISR) at CERN. The synchrotron at FNAL provides high energy particle beams up to 500 GeV for proton beams or 360 GeV for pion beams, while ISR of CERN, with the momentum in the two accelerator rings equal, can reach ~62 GeV in the proton-proton center of mass system, which is equivalent to about 2,000 GeV in the laboratory system. Due to the large multiplicity, defined as the number of particles produced in hadronic interactions, it is impractical to study each individual elastic channel for an understanding of the time-space evolution of the multiparticle production process. However, the single-particle inclusive interaction, which greatly reduces the degree of freedom for the final state study, provides a simpler device for attacking these puzzling problems.

(I) Single-Particle Inclusive Interactions.

With the production and scattering type defined as:

$a + b \rightarrow c + x$, where a = projectile
 b = target
 c = outgoing particle
 of type c
 and x = anything else;

we focus only on particle c among the secondaries, without caring much what accompanies it. It should be noted that the inclusive cross sections are not for any channel but are, instead, for an ensemble of channels. For example, inclusive π^+ production may come about from proton-proton (p-p) interactions via various channels as follows:



The inclusive interaction displays a simple spectrum for any type of particle. Concentrating on the characteristics of the final state of this particular type of particle, which is independent of any other type of particle, we study the dependence of the inclusive cross section on P_ℓ and P_t , the longitudinal and transverse momenta re-

spectively, and other properties of this particular type of outgoing particle.

Within the more detailed discussion of inclusive interactions, definitions of the variables that are often used in hadrodynamics of multiparticle productions are also introduced.

1: Energy and Transverse Momentum

In the inclusive interaction $a + b \rightarrow c + x$, the four momentum of particle c (P_c) is used for describing its energy/momentum, and the square of the center of mass energy (s) is used for describing the energy of the whole system.

$$P_c = (E_c, \bar{P}_c)$$

where E_c and \bar{P}_c are the energy and momentum of c respectively; and

$$s = E_{CM}^2 = (P_a + P_b)^2$$

where E_{CM} = total energy in CM system.

The two components of P_c are used as momentum variables

$$\bar{P}_t = \bar{P}_c \sin \theta$$

$\bar{P}_\ell = \bar{P}_c \cos \theta$ where θ = the outgoing angle of c .

One of the very impressive features in the high energy multiparticle production of the inclusive interaction is the small value of the transverse momentum. The secondaries collimate in the forward direction, and the P_t -distribution of the produced particles is rather narrow, with the average value, which is more or less a constant in relation to changes in the incident energies as well as in type of particle or the multiplicity produced, falling in the momentum range of $.3 \sim .5$ GeV/c (1). Figure 1 shows a simple picture of the constant cross section contour in phase space.

P_t -distribution for p-p collisions at ISR-CERN (2) seems to be constant in the very small P_t region, but drops exponentially around the average P_t . When $P_t > 1.0$ GeV, the distribution function drops more slowly than it does in the mid-range. This very large transverse momentum region has been much studied for evidence about the structure of elementary particles.

2: Rapidity Distribution and Angular Distribution

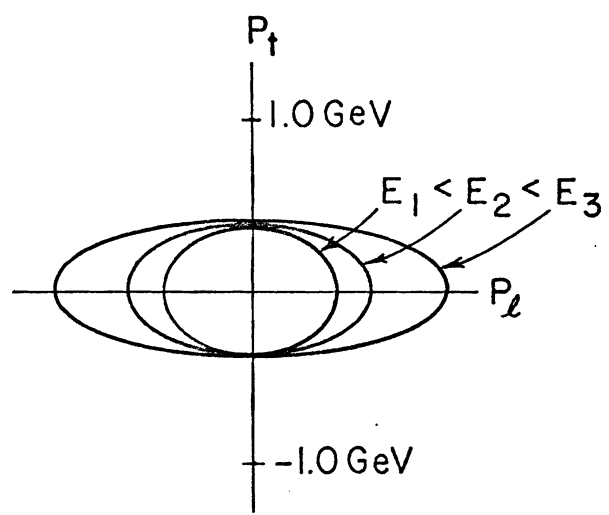
The rapidity (y), defined as

$$y = \frac{1}{2} \ln \frac{E + P_\ell}{E - P_\ell} = \tanh^{-1} \beta ,$$

is a longitudinal variable used in studying high energy

FIGURE 1.

A simple picture of the constant cross section contours in phase space at different energies E_1, E_2, E_3 .



collisions. The advantage of using this formulation is due to its Lorentz invariance under longitudinal Lorentz transformations. For example, the transformation of the rapidity of particle i from the CM system to the lab system is

$$y_i^{\text{lab}} = y_i^{\text{CM}} + c$$

where c is a constant and equal to the target rapidity in the CM system. Thus,

$$c = \frac{1}{2} \ln \frac{E_b^{\text{CM}} + p_{b\ell}^{\text{CM}}}{E_b^{\text{CM}} - p_b^{\text{CM}}} = \ln \frac{E_b^{\text{CM}} + p_{b\ell}^{\text{CM}}}{M_b} = \ln \frac{E_{\text{CM}}}{M_b}$$

with M_b = mass of the target nucleon.

The difference in the description of the Lorentz transformation between the two frames of reference is only a matter of a shift in scale by some constant; the shape of the cross section on rapidity is invariant.

When the interaction energy is high such that $p_t^2 \gg M^2$, all the particles can be considered as massless, and the rapidity is equal to the pseudo-rapidity (η)

$$y = \frac{1}{2} \ln \frac{E + p_\ell}{E - p_\ell} \xrightarrow{p_t^2 \gg M^2} - \ln \tan \frac{\theta}{2}$$

where θ = the angle of outgoing particles with respect to the incident particle.

The quantity $-\ln \tan \frac{\theta}{2}$ is defined as pseudo-rapidity η and differs from y only for the small rapidity region. For example, in the interaction $\pi^-p \rightarrow \pi^-x$ at 147 GeV (3), the y - and η - distributions only have a slight difference between $y = -1 \sim 0$ in the lab system.

η is easy to get from the measurements and is often referred to as angular variable for describing the angular distribution of the secondary particles. Other than this, $\ln \tan \theta$ is also often employed as an angular variable in cosmic ray high energy physics as it provides a way of estimating the primary energy for the interactions: this is the Castagnoli method (4,5).

Hypothetical single-particle inclusive spectrum of the hadron-hadron interaction as a function of rapidity is shown in Figure 2(a) for the laboratory system. It is symmetrical about $y = 0$ in the CM system. As the energy increases, the two fragmentation regions separate and the central plateau (pionization region) develops. For $p-p$ collisions at ISR energies (6), CM pseudo-rapidity distribution (Figure 2(b)) shows an extension of the rapidity plateau and an increase in particle density in the central region.

FIGURE 2.

(a) Typical rapidity distribution for hadron-hadron (h-h) collisions at high energy. Regions A, B, and C are

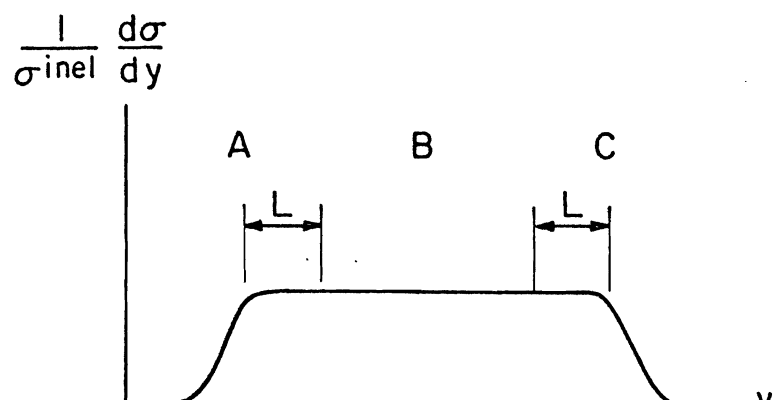
A: target fragmentation region

B: pionization region

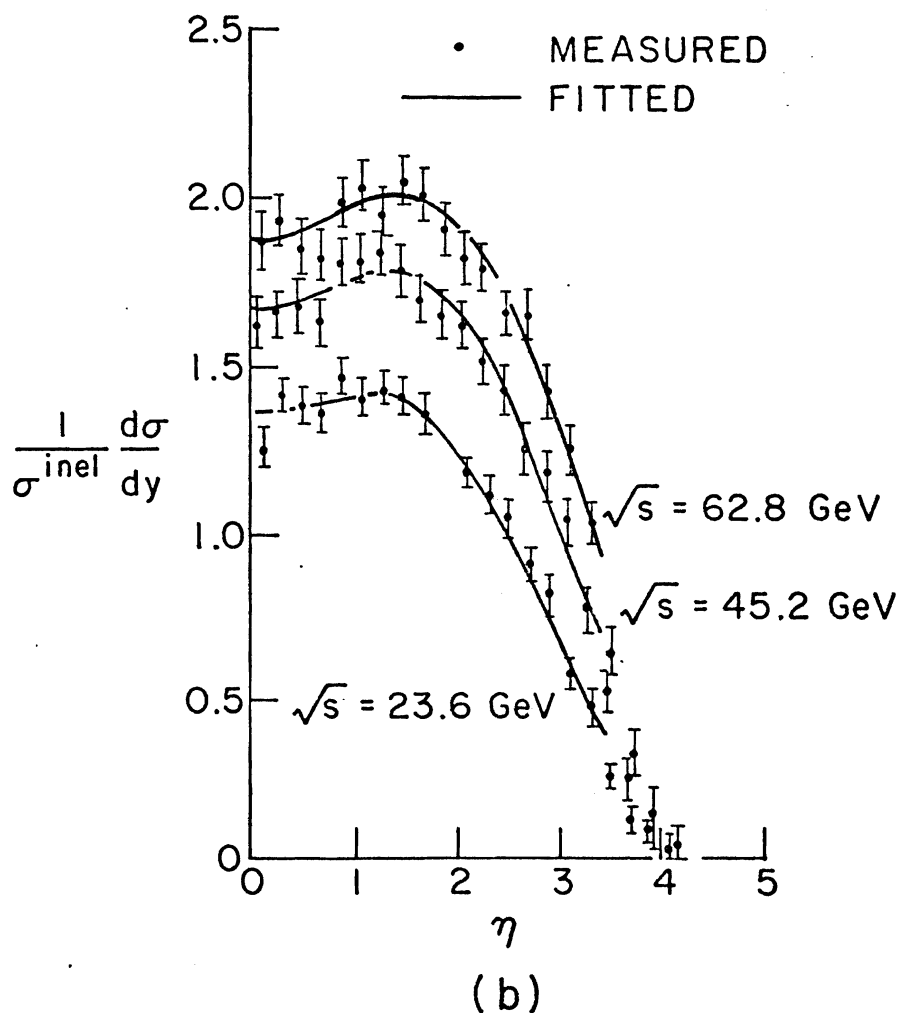
C: projectile fragmentation region.

L is the fragmentation length.

(b) Pseudo-rapidity distribution in the CM system at different ISR energies. Solid lines are the fits for data points.



(a)



3: Inclusive Cross Section

The unpolarized invariant differential cross section for an inclusive inelastic process in phase space can be written as

$$f(\bar{P}, s) = E \frac{d^3\sigma}{d^3P}$$

It is invariant in the sense that $\frac{d^3P}{E}$ is the invariant phase space. The invariant cross section is also related to experimentally observed cross sections in the following forms:

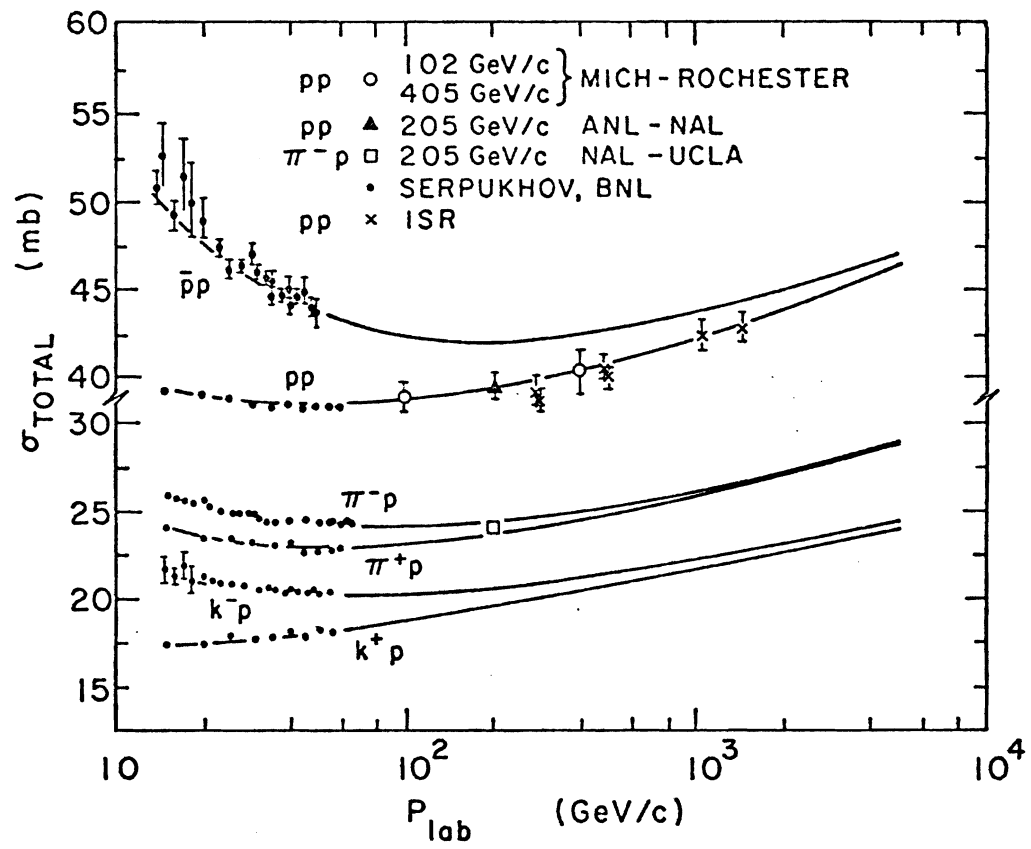
$$\begin{aligned} f &= E \frac{d^3\sigma}{d^3P} = \frac{E}{P^2 d\Omega dP} \frac{d^2\sigma}{dP_\ell dP_t^2} = \frac{E}{\pi} \frac{d^2\sigma}{dP_\ell dP_t^2} = \frac{1}{\pi} \frac{d^2\sigma}{dy dP_t^2} \\ &= \frac{s}{\pi} \frac{d^2\sigma}{dt dM^2} \end{aligned}$$

where y is the rapidity as M^2 is the square of the mass.

The total cross section (σ_t) for some hadronic collisions is shown in Figure 3. It is remarkable that the total cross section of pions, kaons and protons are independent of energy between $20 \sim 200$ GeV. Similar observations for this energy range are also obtained from the hydrogen bubble chamber (HBC) at FNAL. There is, however, an increase for the total cross section measured at ISR above ~ 200 GeV. Yodh, Pal and Trefil (7) also

FIGURE 3.

Total cross section for π^+p , K^+p , $p\bar{p}$, and $\bar{p}p$ interactions. The solid curves are the cross sections predicted by H. Cheng et al. (44).



inferred this effect based on some observations of cosmic ray data. Unfortunately, at presently available energies, the bubble chamber measurements of p-p cross section at FNAL are unable to confirm or disprove this increase.

4: Limiting Fragmentation and Scaling Hypothesis

(A) Limiting Fragmentation Hypothesis

Very similar in spirit to the two-fireball model (8, 9) and the concept of diffractive dissociation (10), is the hypothesis of limiting fragmentation proposed by J. Benecke et al. (11,12), which describes the limiting behavior of the fragmentation of two colliding particles (i.e., projectile and target) in either high energy lepton-hadron collisions or hadron-hadron collisions, in both laboratory (L) and projectile (L') rest frames.

Consider a high energy collision in either L or L' systems: two of the colliding particles may be regarded as two semitransparent bodies. One particle shrinks into a thin disk by Lorentz contraction and passes through and excites the other--or may even break it up after exciting it--during the passage time interval. As the energy increases, the time of passage remains essentially fixed although the incoming particle gets thinner and thinner. The constancy of both the total cross section and of the

elastic scattering cross section suggests that the momentum and quantum number transfers between the excited media do not appreciably change. Thus one expects that the excitation and break-up of the rest particle approaches a limiting distribution. Therefore, for example, in the L system of a high energy collision, fragments from the projectile are emitted with an increasing velocity v as energy increases, while the fragments of the broken-up target remain finite as energy increases and approach a limiting distribution as $s \rightarrow \infty$. For the inclusive spectrum of the particle c in L, $F_c(P_t, P_\ell, s)$, we have

$$F_c(P_t, P_\ell, s) \xrightarrow{s \rightarrow \infty} F_c(P_t, P_\ell)$$

As for the projectile, in L' , where the incoming projectile is at rest, and one expects that the inclusive spectrum $F'(P_t, P_\ell^{L'}, s)$ of the fragments from the projectile approaches limiting as $s \rightarrow \infty$, then

$$F'_c(P_t, P_\ell^{L'}, s) \xrightarrow{s \rightarrow \infty} F'_c(P_t, P_\ell^{L'})$$

where L' indicates the L' system.

The asymptotic limits are in general different for different collisions.

(B) Scaling Hypothesis

The Scaling Hypothesis, proposed by R. P. Feynman (13) in 1969, arose from theoretical studies based on several approaches to high energy hadron collisions. This hypothesis predicts very well the characteristics of inclusive longitudinal-momentum distributions for different extreme energies.

The scaling hypothesis is concerned only with the center of mass (CM) system. The predictions of this hypothesis can be stated as follows: Let f_c be the probability of finding, among all the emitted particles, a particle of type c , with transverse and longitudinal momenta P_t and P_ℓ^{CM} , and Feynman variable x , which is defined as the ratio of longitudinal momentum to the maximum value of longitudinal momentum, which is essentially equal to the incident projectile momenta

$$x = \frac{P_\ell}{P_{\ell \text{ max}}} \xrightarrow{s \rightarrow \infty} \frac{2P_\ell}{\sqrt{s}}$$

As the energy becomes very high, the cross section becomes energy independent, f_c is dependent only on P_t , x , and the type of collision, and is ultimately independent of the energy. Furthermore, as $x \rightarrow 0$, it has a limit independent

of x ; that is

$$f_c(p_t, p_\ell^{\text{CM}}, s) \longrightarrow f_c(p_t, x) \text{ for finite } x;$$

$$\longrightarrow f_c(p_t) \text{ for small } x.$$

By the hypothesis, the asymptotic limits of the inclusive momentum distributions for extreme energies are valid for the whole domain of the Feynman variable $-1 < x < 1$.

The scaling hypothesis also predicts the logarithmic growth of the average multiplicity in multiparticle production (13). Moreover, the scaling hypothesis includes the limiting fragmentation hypothesis for $x \neq 0$. As $x \rightarrow 0$, no prediction is made by the limiting fragmentation hypothesis, since when $x \approx 0$ the momentum is finite only in the CM system.

(C) Discussion

Data within the ISR energy range (2,6) has shown a satisfactory agreement with the scaling hypothesis in the two fragmentation regions in most reactions. As for the central region, the asymptotic increase of the p-p total cross section shown in Figure 3 may violate the scaling hypothesis to some extent, and it would be possible to see the accuracy of the scaling hypothesis only when energy is very high, so that the central region could be

well developed and separate from the fragmentation regions (see the discussion of correlation). Data from ISR, in Figure 2(b), do show non-scaling for the central region, where the rapidity distribution rises as the energy increases.

5: Multiplicity

Charged multiplicity (n_s) of a high energy interaction is defined as the number of charged particles of interest (e.g. type c particles in the interaction $a + b \rightarrow c + X$) produced in each collision. The average multiplicity $\langle n_s \rangle$, which is average over all the events that have occurred, can be derived by integrating the inclusive spectrum over the phase space, or by the summation of the products of all possible multiplicities and their probabilities

$$\langle n_s \rangle = \frac{1}{\sigma_{inel}} \int f_c \frac{d^3p}{E} = \frac{1}{\sigma_{inel}} \sum n \sigma_n$$

It has been noted that the data from cosmic rays or accelerator rays show that the average multiplicity of hadronic interactions is low compared to what would be expected if all the incident energy were transferred to the creation of secondaries.

The energy dependence of the average multiplicity predicted by most of the theoretical models is the $\ln s$

dependence in the high energy region and a power function dependence (s^α) in the low energy region. π -p interactions for the whole energy range up to $\sim 2,000$ GeV available at ISR can be expressed as (14)

$$\langle n_s \rangle = A + B \ln s + C s^{\frac{1}{2}} \quad \text{with } A = -1.94 \pm 0.43, \\ B = 1.65 \pm .07 \\ C = 2.91 \pm 1.01;$$

and the χ^2 per degree of freedom equal to 2.1.

For the multiplicity distribution, the Chew-Pignotti model (15,16) predicted a Poisson-type multiplicity distribution P by assuming that the particles are produced in uncorrelated centers of production (e.g., clusters)

$$P(n) = c \left\{ \frac{\langle n \rangle^n e^{-\langle n \rangle}}{n!} \right\} \quad \text{where } c \text{ is a constant.}$$

However, it has been found experimentally that for hadron-hadron interactions, the dispersion (D) for the multiplicity distribution is dependent roughly on average multiplicity $\langle n \rangle$ linearly (17) for all incident particles in the energy range presently available by

$$D = (.54 \pm .02) \langle n_s \rangle - (.40 \pm .07) \quad \text{for } \pi\text{-p} \\ = (.58 \pm .01) \langle n_s \rangle - (.56 \pm .01) \quad \text{for } p\text{-p}$$

instead of $D = \langle n_s \rangle^{\frac{1}{2}}$, which is the dispersion for Poisson distribution. Experimentally, the multiplicity distribution was found to be narrower than the Poisson distribution when the energy was lower than 30 GeV and broader when the energy was higher than 100 GeV.

Empirical formulas have been proposed by several authors (17,45). Moreover, Koba, Nielsen and Olesen (18) proposed a scaling multiplicity distribution (KNO scaling) and show that asymptotically $\langle n \rangle \sigma_n(s)$ is only a function of $n/\langle n \rangle$. When the energy is high, the asymptotic behavior of topological cross sections may be summarized as

$$P_n(s) = \frac{\sigma_n(s)}{\sigma_{inel}(s)} \xrightarrow{s \rightarrow \infty} \frac{1}{\langle n \rangle} \Psi\left(\frac{n}{\langle n \rangle}\right)$$

where $\Psi\left(\frac{n}{\langle n \rangle}\right)$, the normalized asymptotic form for the multiplicity distribution, is independent of energy itself except through the variable $Z = \frac{n}{\langle n \rangle}$, and

$$\int_0^\infty \Psi(z) dz = \int_0^\infty P_n(s) dn = 1$$

$$\int_0^\infty z \Psi(z) dz = \frac{1}{\langle n \rangle} \int_0^\infty n P_n(s) dn = 1$$

For p-p interactions in the energy range 50 ~ 303 GeV, the

fit of multiplicity distribution done by Slattery (19, 20) for the function $\Psi(z)$ is

$$\Psi(z = \frac{n}{\langle n \rangle}) = 3.97z + 33.7z^3 - 6.64z^5 + .332z^7) \exp(-3.04z)$$

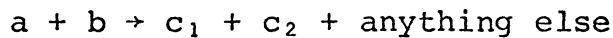
All data points with a satisfactory χ^2 indicate that the scaling idea is experimentally useful in this energy range.

(II) Two-Particle Rapidity Correlation.

One of the main reasons for studying the rapidity correlation of secondary particles in inclusive reactions of high energy hadron interactions is to see how particles which exist in the same region of the phase space are correlated with each other. This will help to evaluate various mechanisms proposed by different models.

1: Definition

For the two-particle inclusive process,



The normalized single-particle and two-particle inclusive densities are defined by (1) and (2) respectively.

$$\rho^1(y) = \frac{1}{\sigma_{\text{inel}}} \frac{d\sigma}{dy} \quad (1)$$

$$\rho^2(y_1, y_2) = \frac{1}{\sigma_{\text{inel}}} \frac{d^2\sigma}{dy_1 dy_2} \quad (2)$$

where σ_{inel} = total inelastic cross section;

and y_1, y_2 are the rapidities corresponding to particles c_1 and c_2 .

If particles c_1 and c_2 are uncorrelated, $\rho^2(y_1, y_2)$ would be simply the product of $\rho^1(y_1) \cdot \rho^1(y_2)$. The two-particle rapidity correlation function is then defined as the difference between the two-particle inclusive density and the product of the two independent single-particle densities:

$$C(y_1, y_2) = \rho^2(y_1, y_2) - \rho^1(y_1) \cdot \rho^1(y_2)$$

By integrating over y_1 and y_2 , we get the second moment of multiplicity distribution:

$$\int C(y_1, y_2) dy_1 dy_2 = \langle n(n-1) \rangle - \langle n \rangle^2 = f_2 \quad (3)$$

where n = multiplicity.

The normalized two-particle rapidity correlation function $R(y_1, y_2)$, defined below, is also often used by experimentalists because it is less sensitive to experimental error, and still has the same qualitative behavior as $C(y_1, y_2)$.

$$\begin{aligned}
 R(y_1, y_2) &\equiv \frac{\rho^2(y_1, y_2) - \rho^1(y_1)\rho^1(y_2)}{\rho^1(y_1)\rho^1(y_2)} \\
 &= \frac{\sigma_{\text{inel}} \left(\frac{d^2\sigma}{dy_1 dy_2} \right)}{\frac{d\sigma}{dy_1} \cdot \frac{d\sigma}{dy_2}} - 1 \\
 &= \frac{N_T N_2(y_1, y_2)}{N_1(y_1)N_1(y_2)} - 1
 \end{aligned}$$

where N_T = total number of events;

$N_1(y)$ = total number of particles at rapidity y ;

$N_2(y_1, y_2)$ = total number of particle pairs with rapidity y_1 and y_2 in the same event.

2: Short-Range Correlation (SRC) Hypothesis

The hypothesis states that when the rapidities of any two particles, which are secondaries of high energy hadronic interactions, are separated by a distance larger than a certain correlation length L , then the particles are uncorrelated. For instance, let y_i and y_j be the rapidities of particles i and j respectively: if $|y_i - y_j| \gg L$, then, by the SRC hypothesis, particles i and j are expected to have been emitted independently in the inclusive reaction.

The SRC hypothesis also implies the limiting fragmentation property of the single-particle inclusive spectrum. The extent of the limiting property in a single-particle inclusive spectrum depends on the energy considered at the low energy limit (where when energy is too low, the fragmentation region cannot be separated) and on the corresponding width of the rapidity distribution. For convenience, we differentiate this property into three energy ranges.

(i) When energy is low, the width (Y) of the rapidity distribution is less than one correlation length ($Y < L$), all the secondaries are correlated, and the shape of the rapidity distribution function is energy-dependent.

(ii) When the energy is higher, such that $Y > L$, the particles at one end of the spectrum are separated from the particles at the other end by more than one correlation length. By the SRC hypothesis, these are uncorrelated, and emitted independently from the interaction. Thus the inclusive spectra formed the projectile and target fragmentation regions, and both of them limiting.

(iii) When the energy is high enough, such that $Y \gg L$, the spectrum expands and develops the central plateau. Thus the spectrum can be divided into three regions: (A) the target fragmentation region with particle

rapidity (y) less than L ($y < L$); (B) central plateau region ($L < y < Y - L$); and (C) projectile fragmentation region ($y > Y - L$). Particles belonging to different regions are independent of each other.

3: General Discussion: Data and Models

(A) Data

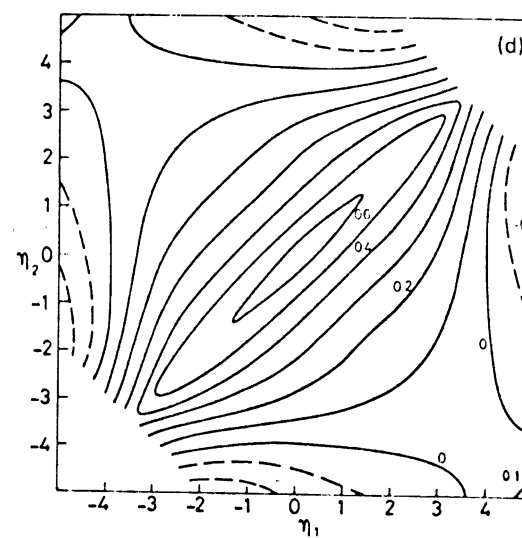
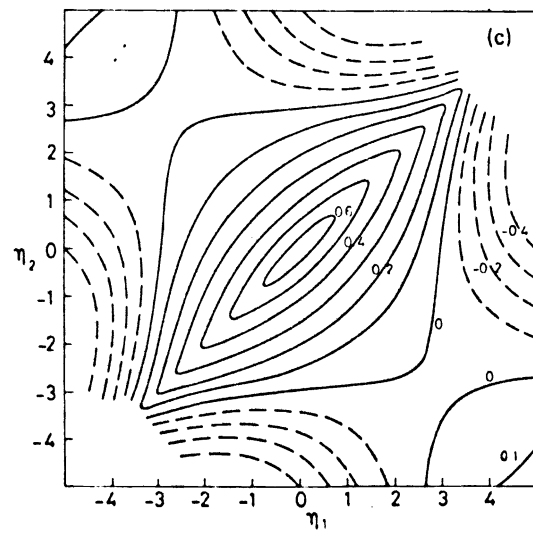
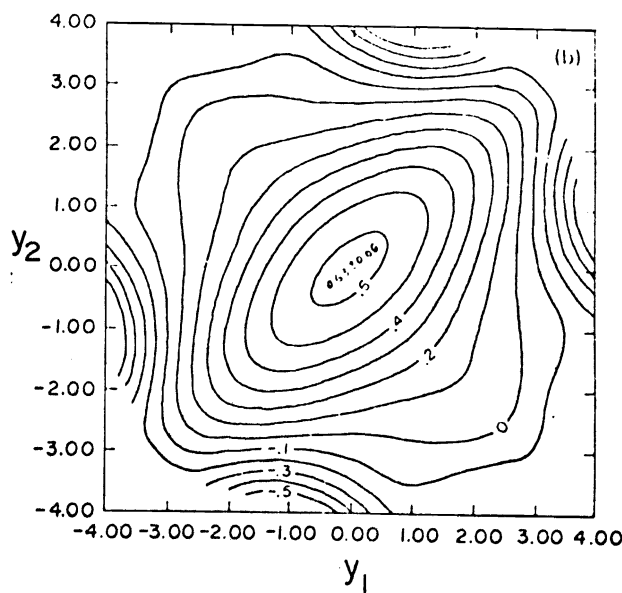
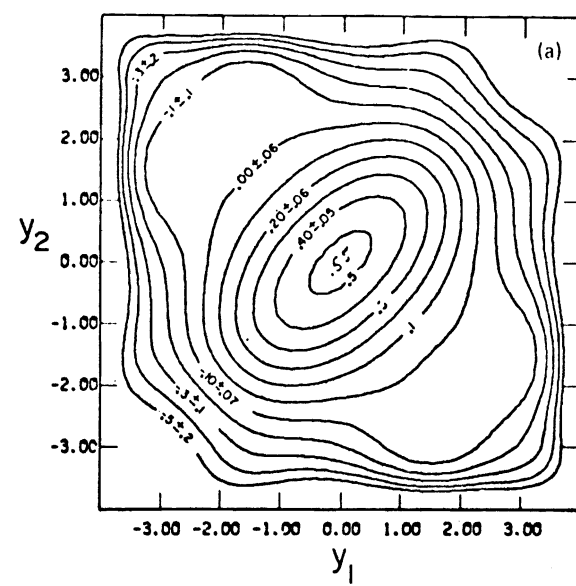
Earlier experiments in two-particle correlation were done at both FNAL and the ISR at CERN.

At FNAL, the main sources are from a 30-inch hydrogen bubble chamber (HBC) with an energy range between 100 GeV \sim 500 GeV. The HBC shows the pattern of each event and each individual track, which makes the direct measurement of the rapidity of each track possible. It also shows the charge of each track. This disadvantages of the HBC are the poor statistics and the inability to identify the nature of the particles. At ISR, where the energy range of the p-p head-on collision reaches $s \sim 63$ GeV in the CM system, several different detectors have been used by various groups (21~26) to collect data.

Some existing data from FNAL and ISR concerning the correlation function $R(y_1, y_2)$ with different energies on p-p collisions are shown in Figure 4. Strong positive short correlation is seen at the central region with

FIGURE 4.

Two dimensional plot of $R(y_1, y_2)$: (a) at 102 GeV;
(b) at 400 GeV (FNAL data) and (c) at $11 + 11$ and (d)
at $31 + 31$ GeV (ISR data).



little energy dependence. An empirical formula for the correlation function $R(y_1, y_2)$ in the central region of the rapidity range is given by C. Quigg (27) with equation (4):

$$R(y_1, y_2) \approx .7 \exp [-|y_1 - y_2|/2] \quad (4)$$

It decreases exponentially with the correlation length $L \approx 2$, independent of the energy. Theoretical calculations done by A. Barband (28), based on Mueller's Regge-pole-dominated method of approach to inclusive reactions (29~31), also suggested that the correlation length L approximately equals two rapidity units. The correlation due to prominent low-energy resonance (32,33) also suggests that $L \approx 2$. The evidence for strong short-range correlation implies that the presence of a particle at a given rapidity favors the production of other particles in the same region of rapidity. Along the $y_1 = -y_2$ line, R drops quickly, but rises to positive value at the large $|y_1| + |y_2|$ region, due to the long range correlation of the diffractive components of the inelastic cross section. The only sign of energy dependence of the function $R(y_1, y_2)$ shown in Figure 4 is that as the energy increases the shape of the pattern expands along the diagonal line; and when the pseudo-rapidity η approaches the fragmentation

region, then $R(y_1, y_2)$ is energy dependent.

The correlation function $R(y_1, y_2)$ also shows the scaling properties for small q^2 for different energies where

$$q = \exp \left(\frac{Y}{2} - y^* \right)$$

where y^* = rapidity in CM system, and Y is the overall rapidity interval.

Although the contour expands with the increase of energy, the scaling of correlation requires that inside the fragmentation core the function $R(y_1, y_2) | y_1 = y_2$ depends only on $(\frac{Y}{2} - y^*)$, and not S , which is similar to those of single-particle spectra.

Investigation of the correlation for like (R^{++} or R^{--}) and unlike (R^{+-}) charged secondaries from the HBC at FNAL (34~36) gives large values of R^{+-} as compared to R^{++} or R^{--} . This fact indicates the dominance of the production of neutral pairs of particles over the production of charged pairs.

(B) Models

There are various models devised to explain correlation properties. Most of the existing data are favorable to the predictions of cluster models, which have success-

fully predicted and interpreted the observed behavior of correlation in the central region of the rapidity plot. As described by this class of model, secondary particles are produced in hadronic interactions in a two step process. As the interactions take place, clusters are formed as an intermediate state and decay afterward into secondary particles. Figure 5 illustrates the production of clusters; each decays into K particles. The simple realization of the decay of clusters is given by an independent-emission model in which it is an isotropic decay of clusters in their rest frames. The rapidity distribution of decayed particles of each cluster is approximately described by a Gaussian form (37) distribution with the dispersion (δ) (38), where $\delta \lesssim 0.9$, corresponding to the production of a single isotropic cluster.

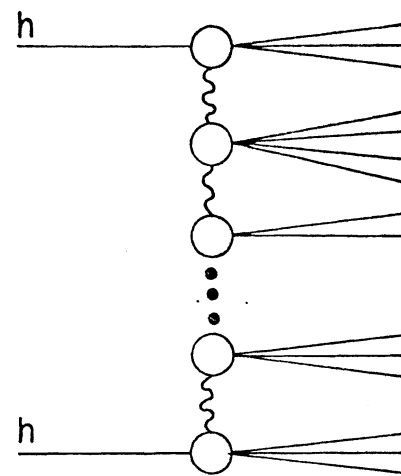
$$P(y, \bar{y}) = \frac{1}{\sqrt{2\pi} \delta} \exp [-(y - \bar{y})^2 / 2\delta^2]$$

where P is the rapidity distribution of decayed particles and \bar{y} is the average rapidity. Particles from different clusters are uncorrelated due to the absence of correlation among clusters. This leads naturally to the short-range correlation behavior of final states.

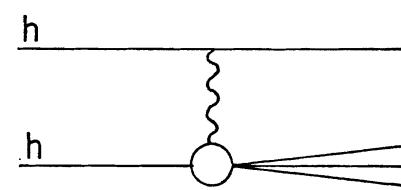
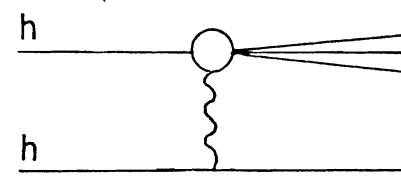
When the energy of the interactions increases, only the number of the clusters increases, while the properties

FIGURE 5.

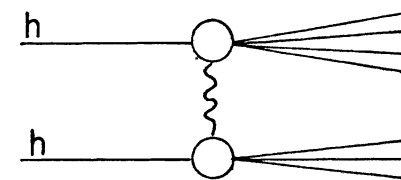
Cluster production in hadronic interactions; each cluster decays into K particles (a) multiperipheral cluster production; (b) diffractive fragmentation production.



(a)



(b)



of the clusters stay well defined. Thus, the decay parameters are energy independent; they depend only on the formation and decay mechanism of each cluster. Data in Figure 4 shows little energy dependence at the center for about 2 units; furthermore, the $R(0,0)$ is energy independent.

The other type of model is the class of two-component models (39~43) which divides events into two groups: (i) diffractive events, usually with low multiplicity, and one particle on one side of the rapidity distribution and several particles on the other side; and (ii), non-diffractive events with all the secondaries distributed all over the pionization region around the center of mass rapidity, with no interference between the two components. These models well predict the increase of secondary moment f_2 (which is related to the correlation function by equation (3)) with energy. In other words, the multiplicity distribution broadens with the increase in energy.

CHAPTER II:
REFERENCES.

1. S. Hayakawa. Cosmic Ray Physics; Monographs and Texts in Physics and Astronomy, vol XXII, Wiley-Interscience (1969).
2. P. Capiluppi et al. Nucl. Phys. B79, 189 (1974).
3. W. Busza. AIP Conference Proceedings #26 (1975).
4. J. Gierula and W. Wolter. Acta Physica Polonia B2, 95 (1971).
5. C. Castagnoli et al. Nuovo Cimento 10, 1539 (1953).
6. W. Thomé et al. Preprint, submitted to Nucl. Phys. (June 1977).
7. G. B. Yodh et al. Phys. Rev. Lett. 28 #15, 1005 (1972).
8. G. Cocconi. Phys. Rev. 111, 1969 (1958).
9. R. K. Adair. Phys. Rev. 172, 1370 (1968).
10. M. L. Good and W. D. Walker. Phys. Rev. 120, 1857 (1960).
11. J. Benecke et al. Phys. Rev. 188 #5, 2159 (1969).
12. T. T. Chou and C. N. Yang. Phys. Rev. Lett. 25, 115 1072 (1970).
13. R. P. Feynman. Phys. Rev. Lett. 23 #24, 1415 (1969).

14. E. Albini. Nuovo Cimento 32A, 101 (1976).
15. G. F. Chew and A. Pignotti. Phys. Rev. Lett. 20, 1078 (1968).
16. G. F. Chew and A. Pignotti. Phys. Rev. 176, 2112 (1968).
17. E. De Wolf et al. Nucl. Phys. B87, 325 (1975).
18. Z. Koba, H. B. Nielsen and P. Olesen. Nucl. Phys. B40, 317 (1972).
19. P. Slattery. Phys. Rev. Lett. 29 #24, 1624 (1972).
20. P. Slattery. Phys. Rev. D7 #7, 2073 (1973).
21. S. R. Amendolia et al. PSB Collaboration. Phys. Lett. 48B #4, 359 (1974).
22. H. Dibon et al. Phys. Lett. 44B, 313 (1973).
23. E. Eggert et al. Nucl. Phys. B86, 201 (1975).
24. M. G. Albrow et al. Phys. Lett. 51B, 421 (1974).
25. J. V. Allaby et al. 17th Int. Conf. on High Energy Phys., London (1974).
26. G. Ranft and J. Ranft. Phys. Lett. 45B #1, 43 (1973).
27. C. Quigg. AIP Conference Proceedings #12 (1973).
28. A. Barband. Phys. Rev. D3, 2227 (1971).
29. A. H. Mueller. Phys. Rev. D2 2963 (1970).
30. A. H. Mueller. Phys. Rev. D4, 150 (1971).
31. J. Koplik and A. H. Mueller. Phys. Rev. D12 #11, 3638 (1975).

32. W. R. Frazer et al. Rev. of Mod. Phys. 44 #2 (1972).
33. W. R. Frazer et al. 13th International Cosmic Ray Conference, Denver, Colorado, 17-30 August (1973).
34. T. Ferbel. Recent Results from HBC at FNAL COO-3065-91 (1974).
35. N. N. Biswas et al. Phys. Rev. Lett. 35 #16, 1059 (1975).
36. J. Whitmore. AIP Conference Proceedings #12 (1973); preprint NAL-Pub-73/70-EXP (1973).
37. E. L. Berger and A. Krzywicki. Phys. Lett. 36B, 380 (1971).
38. E. L. Berger. Phys. Lett. 43B #2, 132 (1973).
39. K. G. Wilson. Cornell preprint CLNS-31 (1970).
40. A. Bialas et al. Nucl. Phys. B48, 237 (1972).
41. K. Fialkowski. Phys. Lett. 41B, 379 (1972).
42. K. Fialkowski. Phys. Lett. 43B, 61 (1973).
43. P. Pirilä. Phys. Lett. 43B, 502 (1973).
44. H. Cheng et al. Phys. Lett. 44B, 97 (1973).
45. O. Czyzewski and K. Rybicki. Nucl. Phys. B47, 633 (1972).

CHAPTER III:
THEORY OF HADRON-NUCLEUS INTERACTION

In high energy physics, some theoretical effort has been made in understanding the multiparticle production of hadron-nucleus (h-A) interactions. However, the account of production dynamics is still very inadequate for explaining many features of the process, such as the lack of intranuclear cascading, the space time evolution of the interaction, or how secondaries are emitted and how they are correlated with each other. Models using the basic information of the hadron-hadron (h-h) interactions and some special assumptions have been developed to interpret the production process. Although different mechanisms have been assumed, and thus have resulted in differences in the predictions of some measurable physical quantities in different models, all the models have those features in common that are needed to agree with the data. For the sake of discussion, two major types of model are presented separately, one of which considers the h-A interaction as a sequence of independent collisions of hadrons and nucleons, and the other of which considers the h-A interaction as a hadron and nucleus interacting coherently.

(I) Models With Independent Collisions with Constituents.

Within this class of model, descriptions were devised more to account for the various qualitative features of h-A interactions in terms of the independent h-h interactions of the projectile hadron with the nucleons. The nuclear cascading is the result of the composition of those h-h interactions that occur inside the target nucleus. Several categories of models can be differentiated by their proposed interaction mechanisms.

1: Several Phases Models

Historically, in h-A interactions, secondary particles were first assumed to materialize right after each h-h collision inside the nucleus and to be able to interact with the downstream hadrons. This process develops a nuclear cascade which is not consistent with the low multiplicity in hadron-nucleus interactions.

In new versions (1~4) of this type of model, an intermediate excited state, which will materialize into secondary particles after a certain characteristic time τ longer than the nucleus radius, was introduced. Interactions are involved with several phases of the excited hadronic matter with the downstream hadrons. Various assumptions are made by models of this sort about the nature of

the excited state, but they all have certain features in common: (i) low multiplicity production; (ii) the same cross section for both excited and unexcited hadronic matter; and (iii) long range correlation among secondary particles.

(A) Energy Flux Cascade (EFC) Model

Proposed by K. Gottfried (2), the EFC model follows the main idea of Landau's hadrodynamiic model (5,6)--that the essential variable is the energy-momentum flux of hadronic matter (not a conventional hadron), and that this is what determines the early evolution of the system.

Consider τ' to be the characteristic time for h-h collisions in the CM system. From the Lorentz transformation, the interaction time will be $\tau = \tau' \gamma$ in the Lab system.

The basic assumptions made in this model are that:
(i) When a projectile with sufficiently high energy collides with the first nucleon in the nucleus, it forms excited hadronic matter within an expanding cylinder which can be considered as energy flux with a rapidity distribution the same as that in the h-h collision. (ii) As the energy becomes high enough, τ would be long compared to the nucleus interaction mean free path λ . (iii) This flux

can be divided into "slices," each of which, after some characteristic time, has the spatial thickness appropriate to a hadron, and can be considered as a "Gottfried hadron" moving with the mean rapidity of that slice. This is a universality hypothesis: when any hadronic state occupies the same volume as a hadron with the same rapidity, its behavior in a collision is close to that of an ordinary hadron. Thus, this Goffried hadron, which behaves as a single hadron, will interact with \bar{v} downstream hadrons in the same cross section as an h-h collision, where \bar{v} is the average number of collisions and is estimated as

$$\bar{v} = \frac{A\sigma_{hp}^{\text{inel}}}{\sigma_{hA}^{\text{inel}}}$$

In general, \bar{v} is roughly the average nuclear thickness in units of mean free path of the projectile with the nucleons.

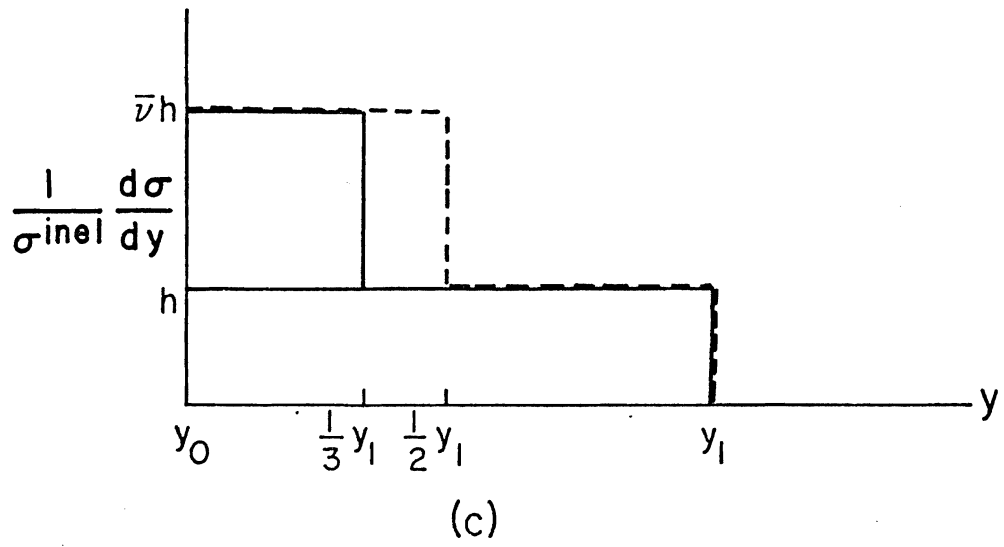
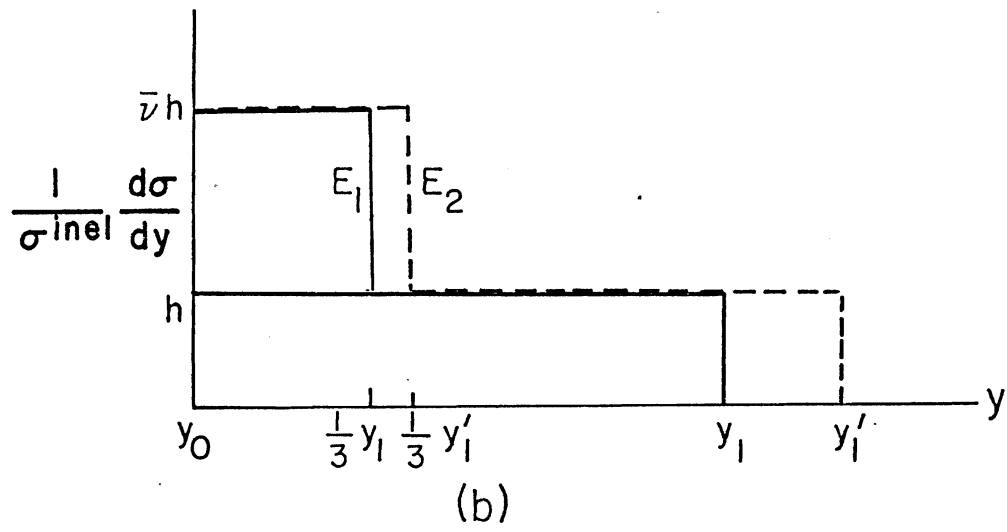
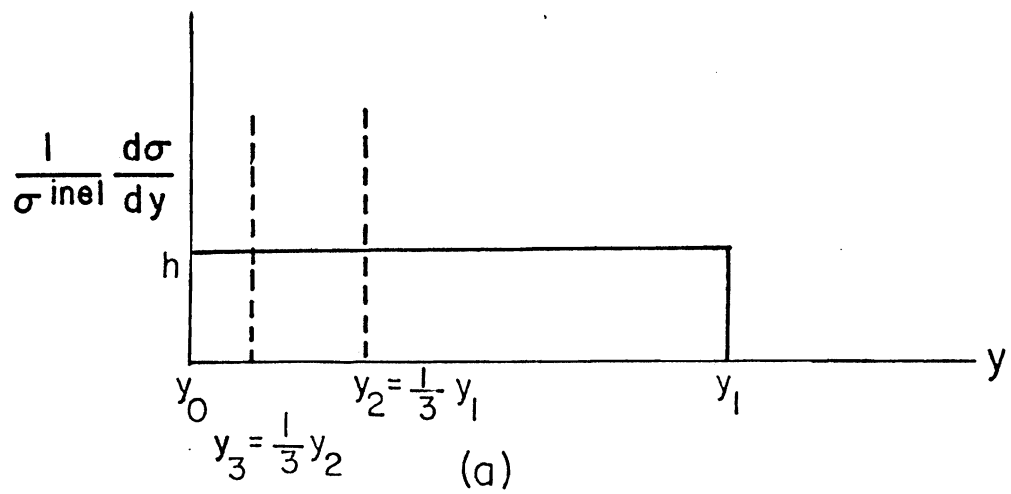
Figure 6(a) shows the slicing of the rapidity distribution into Gottfried hadrons. For h-h collisions, the rapidity distribution is between y_0 and y_1 , where y_1 is the incoming rapidity. As the flux expands, the first slice would be the energy flux moving with a rapidity distribution between y_1 and y_2 ; the second, between y_2 and y_3 , and so on.

FIGURE 6.

(a) The slices of energy flux (for example, 3) in EFC model for an ideal h-h rapidity distribution. The slice with energy corresponding to a hadron can interact with the downstream nucleons and form the energy flux with rapidity distribution similar to that of h-h interactions.

(b) Rapidity distributions predicted by Gottfried's EFC model with different incident energies E_1 (solid line) and E_2 (dash line), where $E_2 > E_1$.

(c) A comparison of Gottfried's EFC model (solid line) and the modified EFC model (dash line).



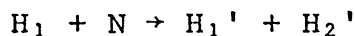
From the calculations done by Gottfried (1), the number of slices divided (K) grows like $\ln(\ln s)$; thus, $K = 3$ when $E \approx 10^6$ GeV, which is much higher than what can be obtained at ISR-CERN or FNAL. Therefore, it is proper to restrict this discussion to only that case in which two slices of energy flux H_1 and H_2 , with energy E_1 and E_2 , are divided, with the cut of slices at $\frac{1}{3}$ of the flux rapidity range.

$$y_2 \approx \frac{1}{3}(y_1)$$

$$E_1 \approx E_{\text{inc}} (1 - \text{const. } s^{-\frac{2}{3}}) \approx E_{\text{inc}}$$

$$E_2 \approx \text{const. } s^{\frac{1}{3}} \approx E^{\frac{1}{3}}$$

In the h-A interaction with energy in the range $10^2 \sim 10^6$ GeV, we can consider the nucleus as \bar{v} nucleons lined up with space equal to one interaction mean free length λ . After the first collision, the energy flux is formed and expanding while traversing along its path. Before it reaches the second collision, two Gottfried hadrons H_1 and H_2 are formed. H_1 (hard hadron) carries most of the energy and all the quantum numbers of the incident particle, and would act as the projectile in the following interactions:





while each H_2 (soft hadron) decays into $\frac{1}{3} \langle n_s \rangle_{h-p}$ secondaries (since the energy of H_2 is not sufficient for $H_2 + N \rightarrow H_2' + H_3'$, i.e., $K = 3$).

The overall interaction has two parts. First, one H_1 -nucleon interaction in the last collision produces $\langle n_s \rangle_{h-p}$ secondary particles. Second, there are $(\bar{v} - 1)$ H_2 hadrons, each of which decays into $\frac{1}{3} \langle n_s \rangle_{h-p}$ secondary particles. This double process gives the multiplicity of the interaction as follows:

$$\langle n_s \rangle = \langle n_s \rangle_{hp} + (\bar{v} - 1) \frac{1}{3} \langle n_s \rangle_{hp}$$

This also gives the variable R , defined as the ratio of $h-A$ multiplicity to $h-h$ multiplicity.

$$\begin{aligned} R &= \frac{\langle n_s \rangle_{hA}}{\langle n_s \rangle_{hp}} &= 1 + \frac{1}{3}(\bar{v} - 1) \\ & &= \frac{2}{3} + \frac{1}{3}\bar{v} \end{aligned}$$

R is independent of the incident energy and is dependent on the projectile only through the variable \bar{v} .

This model was modified by G. Calucci et al. due to a detailed dynamic analysis of the interaction process (7). In this analysis, the rapidity spectrum of the secondaries (energy flux) produced in $h-h$ collisions is divided into

two parts, the hard hadron and the soft hadron, with the cut y_c at

$$y_c = \eta Y,$$

where Y is the incoming rapidity, and η , which was put equal to $\frac{1}{3}$ in Gottfried's EFC model, is a parameter to fit the experimental data. It was found that a better agreement of multiplicity distribution can be obtained by adjusting the cut at $\eta = \frac{1}{2}$, which gives the ratio R related as

$$\begin{aligned} R &= 1 + (\bar{v} - 1)\eta \\ &= \frac{1}{2} + \frac{1}{2}\bar{v} \end{aligned}$$

Figure 6 (b,c) shows the rapidity distribution predicted by the EFC model: (b) predicted by Gottfried with different energies, (c) a comparison with that predicted by the modified EFC model.

(B) Two-Phase Model (TPM)

A simple description of the TPM, presented by P. M. Fishbane and J. S. Trefil (3) is as follows.

In hadronic interactions, hadronic matter appears in two phases: excited state and unexcited state. The excited state is formed from the h-h interaction with the

rapidity of excited hadronic matter, uniformly distributed in the range $0 < y < Y$, where Y is the incoming rapidity. The excited hadronic matter can be divided into slices (see Figure 7(a)). Each slice of the rapidity length βY can interact with downstream hadrons in a manner similar to h-h interactions, and produce excited hadronic matter with cross section $\beta \sigma_{\text{total}}^{\text{inel}}$. After the characteristic time τ , which is longer than the nuclear radius, the excited state decays into secondary particles.

This model predicts a wedge-shaped rapidity distribution (shown in Figure 7(b)), and the ratio related to \bar{v} , as

$$R = \frac{1}{2} + \frac{1}{2}\bar{v}$$

(C) A Third Model by J. Babecki et al.

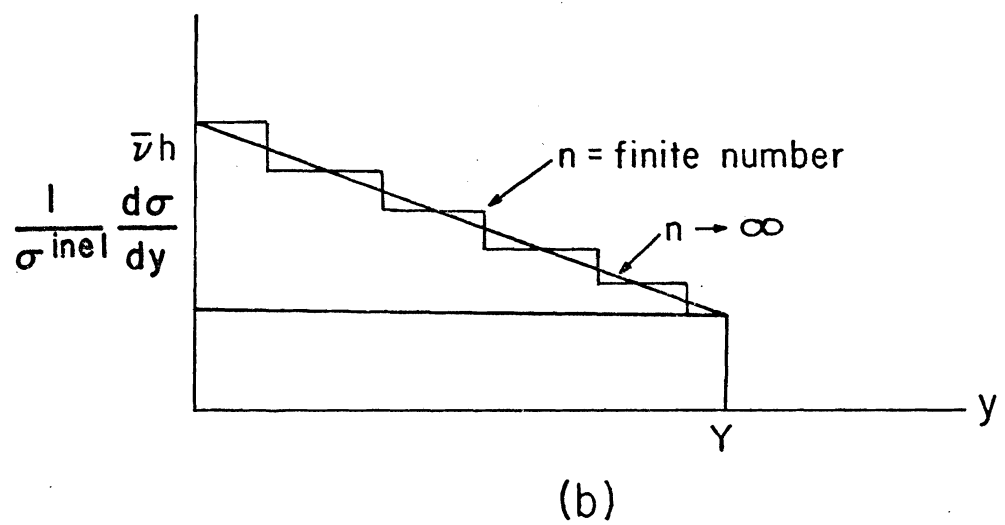
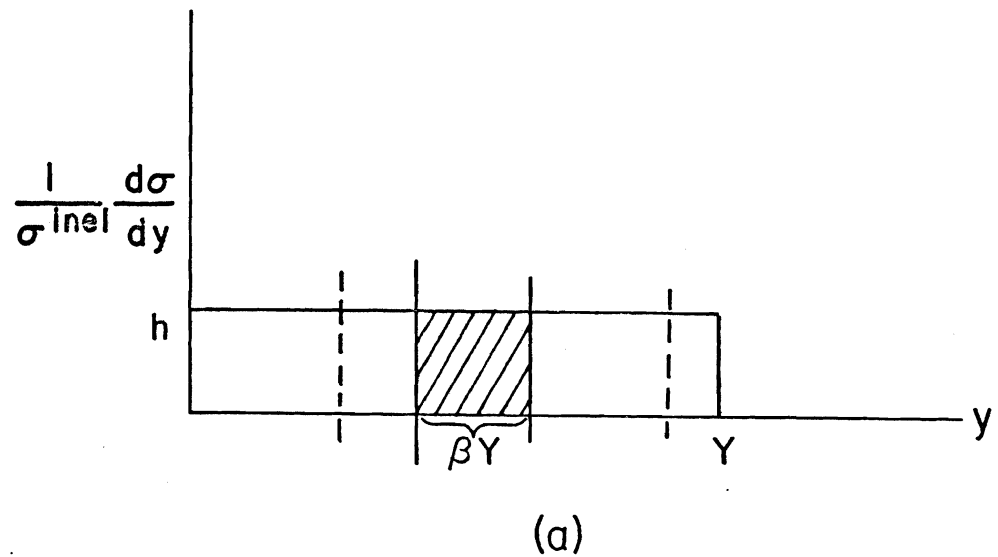
The other method of approach for the rapidity distribution in h-A interactions is discussed by J. Babecki et al. (8) in terms of the excitation of the target nucleus, which is based on observations of rapidity distributions at different energies.

All the secondary particles are assumed to be generated through an intermediate state, and to be divisible into two components which depend only on the incidental

FIGURE 7.

(a) The hadronic matter slices for an ideal rapidity distribution of h-h interactions. The shaded area is a slice of excited hadronic matter acting as a hadron with rapidity length βY and interaction cross section $\beta \sigma_t^{\text{inel}}$.

(b) Rapidity distribution for h-A interactions predicted by TPM: n is the number of slices dividing the excited hadronic matter of the first h-h interaction in the target nucleus.



energy E and the rapidity y : (i) a nuclear excitation-independent component A , and (ii) a nuclear excitation-dependent component B . Thus, the rapidity distribution can be expressed as

$$\Delta n_s (E, y) = A (E, y) + B (E, y) N_h \quad (5)$$

where A and B are the coefficients independent of the target and N_h is the number of heavy particles emitted from the excited target nucleus. N_h is often regarded as a measure of target excitation. It depends on the target mass in the form of $A^{\frac{2}{3}}$ (9) and closely relates to \bar{v} , which is proportional to $A^{\frac{1}{3}}$. However, the relation between N_h and \bar{v} is not universal. It depends on the nature of the projectile (10).

It is found that the rapidity range of both A and B components expands as energy increases, while the rapidity range covered by the B component is always wider than A by 2 high-value rapidity units at all energies. This gives the dependence of rapidity on energy and target size, as shown in Figure 8.

2: Multiperipheral Production Model (MPM)

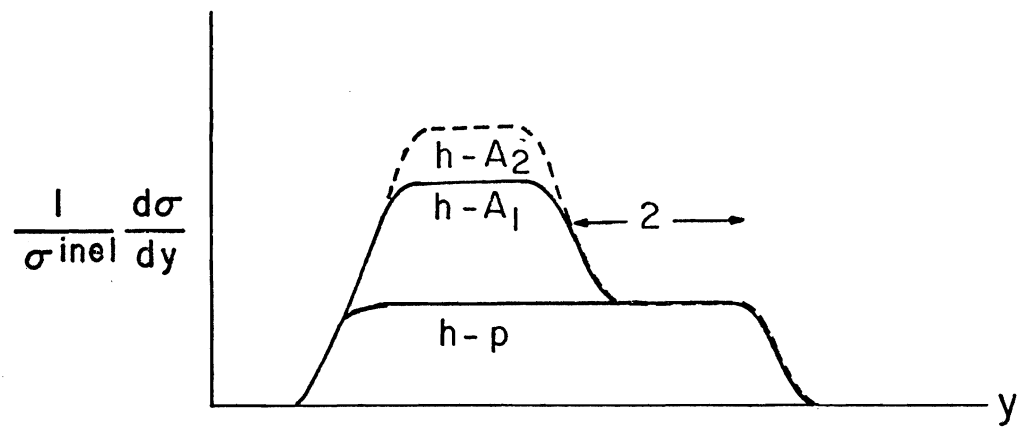
This model has been extensively developed from its early stage, when it was based on the idea that one-pion exchange dominates high energy processes (11), up to

FIGURE 8.

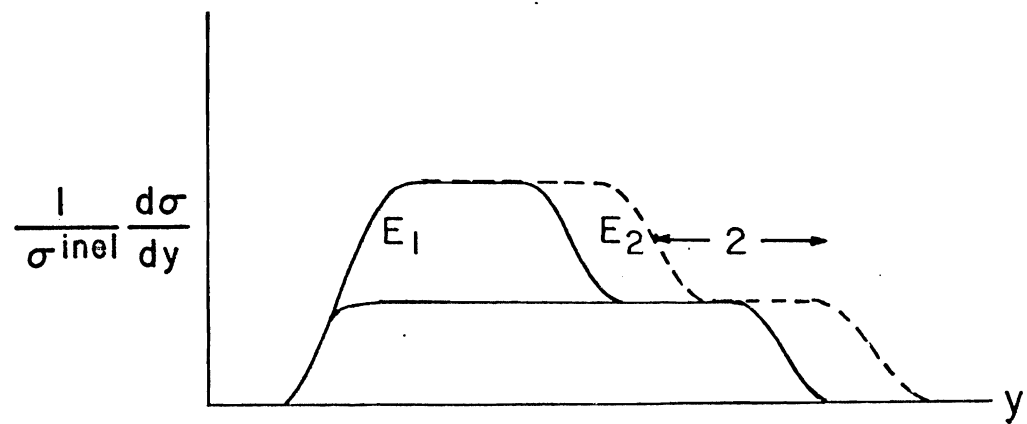
Predictions of rapidity distribution by Babcock et
al.

(a) For different sizes of target (proton, A_1 , and A_2 , where $A_2 > A_1$), target fragmentation rises as the increase of target size; the two-unit difference from projectile rapidity remains unchanged.

(b) For different incident energies, where $E_2 > E_1$.



(a)



(b)

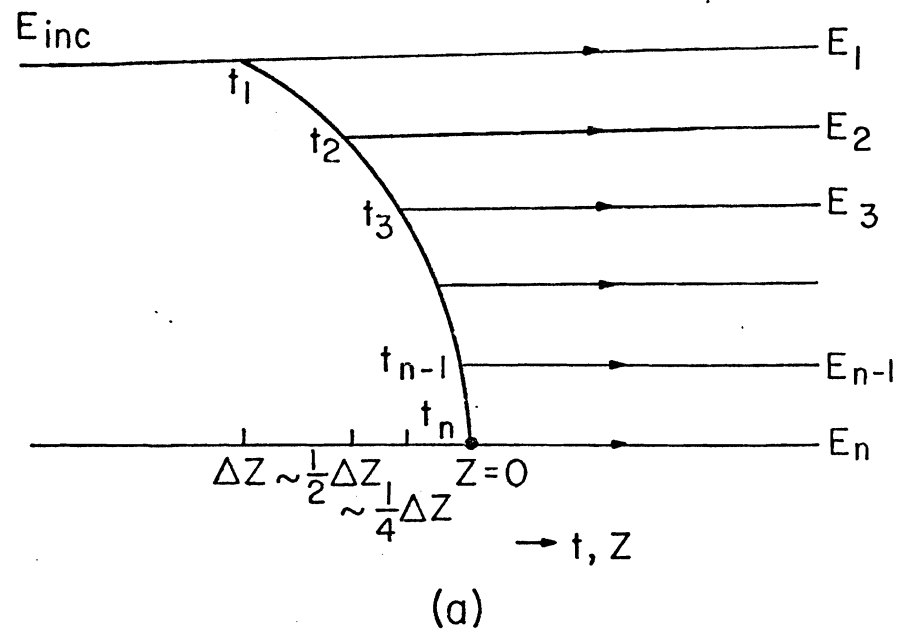
more recent models based on the regge exchange (12) arising from soft field theory. The MPM is described here only briefly, in terms of those versions that fit the data best (13~15).

In the MPM, high-energy hadron-nucleus interaction is usually considered as composed of successive hadron-hadron interactions, that is, as an expansion in the number of interactions between projectile and the individual constituents of the target.

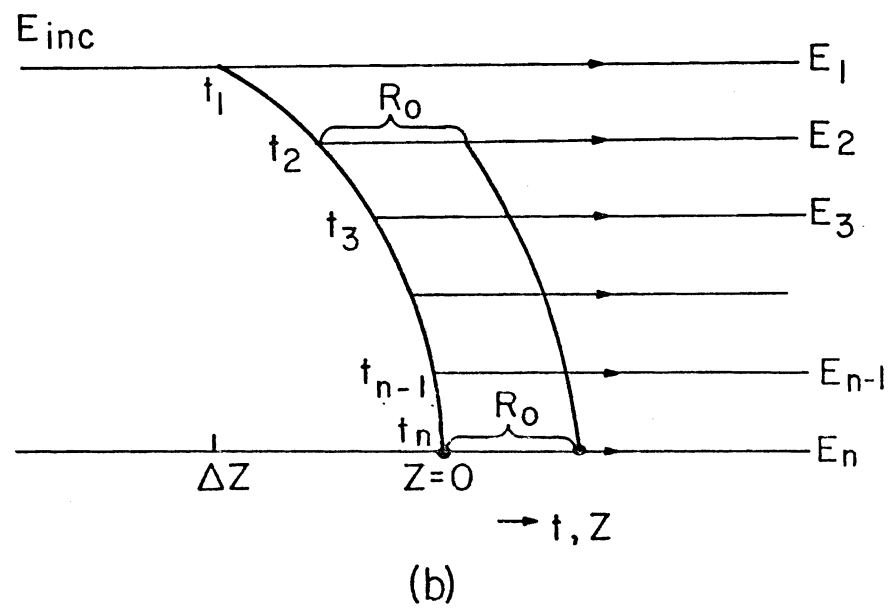
Figure 9(a) shows the longitudinal production process from old fashioned (time ordered) perturbation theory. An incident particle with rapidity y will emit a slower particle (parton) with energy and rapidity $E_2 = \frac{1}{c}E_1$, where c is a constant and $y_2 = y_1 - \Delta$, at a time t_1 before it reaches the target. After a time period $t_2 = \frac{1}{c}t_1$, the second particle emits a third particle with

$$E_3 = \frac{1}{c}E_2, \quad y_3 = y_2 - \Delta, \text{ etc.}$$

From the soft field theory hypothesis, only particles with low energy can interact with the target hadrons to form the nuclear cascade inside the nucleus. To have the cascade within the nucleus requires that the time required for the formation of slow particles $\gamma\tau_0$, where τ_0 is the



(a)



(b)

FIGURE 9.

The time-space picture for hadronic interactions in MPM.

- (a) In h-h interactions, secondary particles are emitted with energies $E_{i+1} = \frac{1}{c} E_i$, where c is a constant.
- (b) In h-A interactions, a second chain can be emitted well before the interaction with target nucleons and form the nuclear cascade. R_0 is the interaction length.

characteristic interaction time, be less than the nuclear diameter R :

$$\tau = \gamma \tau_0 \leq 2R \quad (6)$$

This, then, implies

$$y \approx \ln \frac{2E}{m} = \ln 2\gamma \leq \ln \frac{4R}{\tau_0}$$

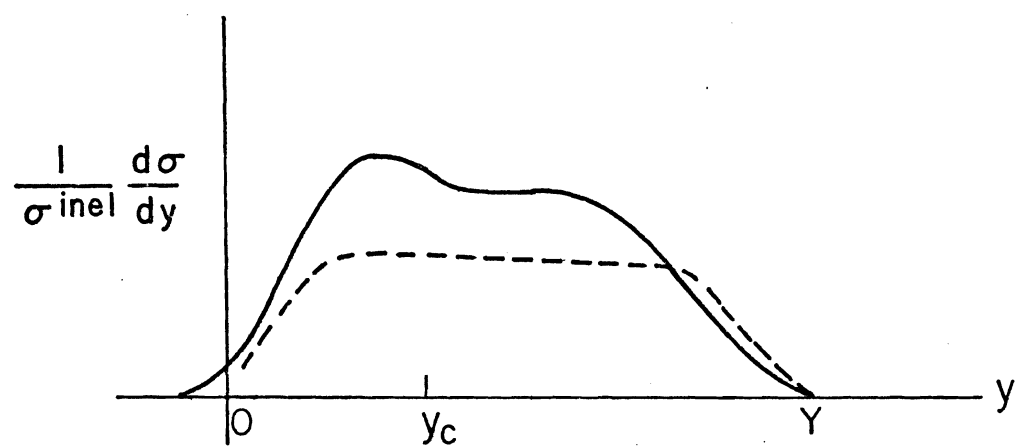
Particles with rapidity less than $y_c = \ln \frac{4R}{\tau_0}$ will interact with target nucleons and contribute to the cascade in high energy hadron-nucleus interactions. However, a second chain can be emitted well before the collision. Thus, multiparticle interactions can take place in the way shown in Figure 9(b).

A typical plot for the rapidity distribution predicted in this model (15,16) is shown in Figure 10. The inclusive cross section increases with A but shows no plateau for large A . In the target fragmentation region where $y < y_c$ (y_c depends on A), a larger increase is possible due to the cascade composed by the rescattering among target nucleons. In the central region, the relative cross section grows roughly as \bar{v} ($\bar{v} \sim A^{\frac{1}{3}}$) at the asymptotic energy limit,

$$\frac{1}{\sigma_{hA}^{\text{inel}}} \frac{d\sigma_{hA}}{dy} \longrightarrow \frac{1}{\bar{v} \sigma_{hp}^{\text{inel}}} \frac{d\sigma_{hp}}{dy} \quad \text{when } s \rightarrow \infty;$$

FIGURE 10.

Predictions of MPM about rapidity distributions for h-A interactions (solid curve) compared with h-h interactions (dash curve). A larger increase at the target fragmentation region is due to rescattering. Depletion is shown in the projectile fragmentation region.



but this limit is reached slowly with increasing s , and at present accelerator energies, the central plateau is not well developed; hence R_y is much less than \bar{v} (16) where

$$R_y = \frac{\frac{1}{\sigma_{inel}^{hA}} \frac{d\sigma_{hA}}{dy}}{\frac{1}{\sigma_{inel}^{hp}} \frac{d\sigma_{hp}}{dy}}$$

In particular, the dependence of $\frac{1}{\sigma_{inel}^{hA}} \frac{d\sigma_{hA}}{dy}$ on \bar{v} becomes rapidly very weak as one moves from central region to projectile fragmentation region where a slight decrease of the differential cross section with \bar{v} is expected. Within the rightmost one or two units (the projectile rapidity region), a slight decrease with A ($\propto A^{-\frac{1}{3}}$) is seen due to the constraints of energy-momentum conservation.

The scaled dispersion of the multiplicity distribution ($D/\langle n_s \rangle$, where D is the dispersion) is predicted (16) to be a constant with respect to $\langle n_s \rangle$ within $\sim 10\%$ error for present accelerator energies.

3: Parton Models

Models in this category, which always include a conventional parton model idea, consider that the final multiparticle state is directly produced from the colliding particles. In the parton model, a relativistic hadron is

viewed as a system of point-like particles--partons. Only wee partons, with relativistic momentum less than $K \approx m$, could interact strongly with each other and the target.

Two more recent versions of the parton-model approach to high energy h-A interactions are discussed below.

(A) N. N. Nikolaev et al.

In the model for h-A interactions described by N. N. Nikolaev et al. (17), after the first inelastic h-h collision takes place in the nucleus, the hadrons dissociate into partons via some multiperipheral mechanism. The parton constituents of the projectile hadron transform into secondary particles with the formation time in the order of $\tau_0 \sim \frac{1}{m}$ (i.e., $\tau \approx E/m^2$ in the lab system), and will be able to interact with downstream hadrons when $\tau < 2R$, where R is the nuclear radius. This model is actually very similar to the MPM in its descriptions of the space-time evolution of h-A interactions, except that it emphasizes collisions of slow partons, with rapidity $y < y_c$.

Predictions made by this model can be summarized as follows.

(i) As in the predictions of the MPM, the variable R_y can be parametrized as $R_y = A^\alpha$, where α is a parameter strongly dependent on the momentum of emitted particles,

particularly in the central rapidity region $R_y \approx A^{\frac{1}{3}}$. Moreover, the depletion of the high rapidity region for large A is also predicted due to energy-momentum conservation.

(ii) The prediction of the multiplicity (discussed in terms of the variable R , where

$$R = \frac{\langle n_s \rangle_{hA}}{\langle n_s \rangle_{hp}} \quad)$$

as a function of incident energy and atomic size is shown in Figure 11. R increases with energy when the energy is not higher than ~ 300 GeV; but, as the energy becomes very high, all curves tend to $R = 1$.

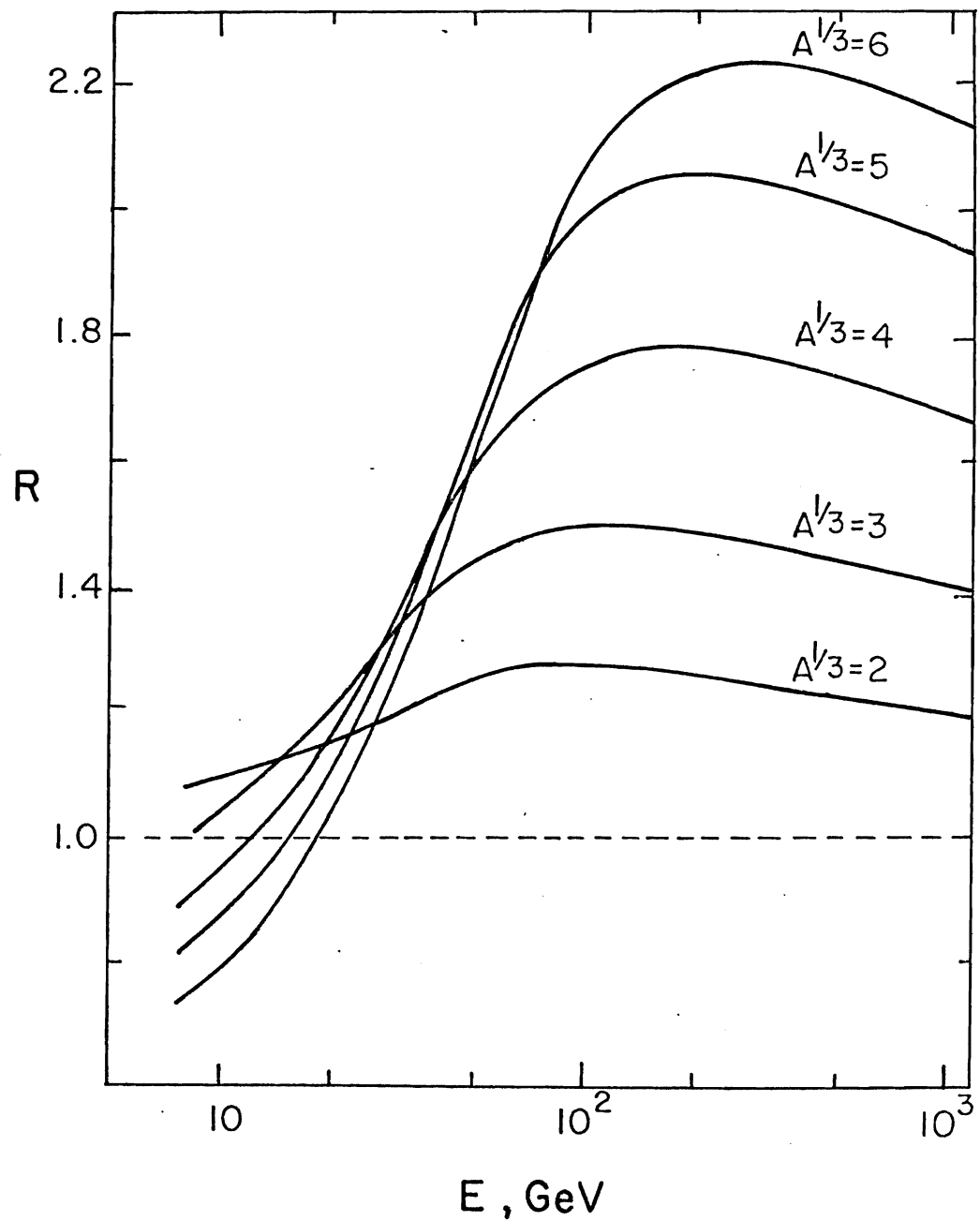
(B) S. J. Brodsky et al.

S. J. Brodsky et al. (18) recently proposed a model that also considers the inelastic h - A interactions as the result of the wee partons of the projectile, which are uncorrelated in rapidity, interacting with the wee partons of the independent nucleons in the target, in a manner analogous to the Drell-Yan pair production process (19,20).

In h - h inelastic interactions, as described in this model, the rapidity \hat{y} , at which the parton-parton collision occurs, is uniformly distributed throughout the central rapidity region, in contrast with the usual model,

FIGURE 11.

The multiplicity ratio R predicted by the parton model of N. N. Nikolaev.



in which it is assumed to be at $y \approx 0$ in whatever frame the system is in. After the collision, the partons in the beam materialize as hadrons with rapidity y in the range where $\hat{y} \lesssim y \lesssim y_B$, and those in the target materialize as hadrons for $y_A \lesssim y \lesssim \hat{y}$, with y_A and y_B being the rapidities for target hadron and beam hadron respectively. In the case of h-A interactions, when the beam particle passes through the target nucleus there are \bar{v} collisions with the hadrons, and the rapidities of the \bar{v} collisions are uncorrelated.

Thus, on the average, one expects $\frac{\bar{v}}{2} n_c$ target hadrons and $\frac{\bar{v}}{\bar{v} + 1} n_c$ projectile hadrons to be emitted as the secondary particles (Figure 12), where n_c is the number of secondaries in the central region of the h-h interaction. Therefore, in the central region, the multiplicity ratio R_{central} can be expressed as

$$R_{\text{central}} = \frac{\bar{v}}{2} + \frac{\bar{v}}{\bar{v} + 1}$$

which is also the asymptotic form of R . When the fragmentation regions are included, the formula for R is adjusted to fit the data of Busza et al. (21) at 200 GeV as follows:

$$R = \frac{\bar{v}}{2} + \frac{\bar{v}}{\bar{v} + 1} - 0.2 \left(\frac{\bar{v} - 1}{\bar{v} + 1} \right)$$

FIGURE 12.

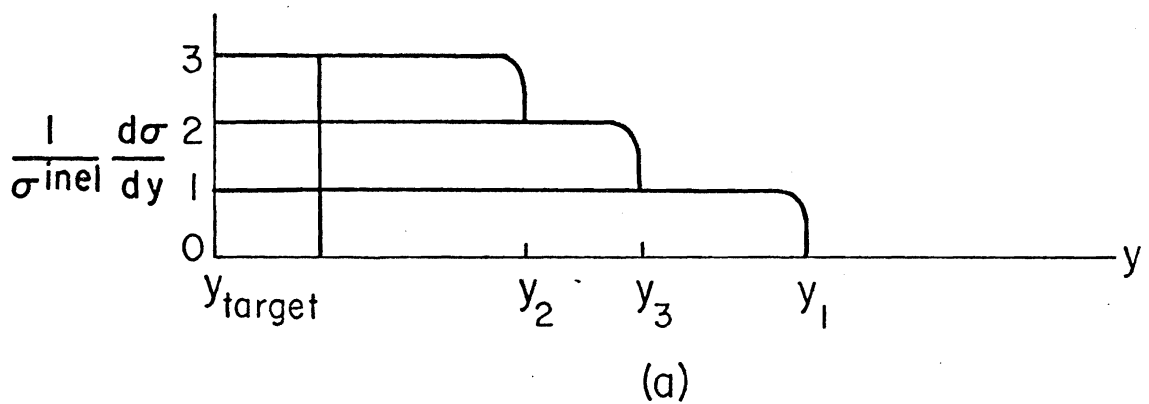
An illustration for h-A interactions (with 3 collisions in the target nucleus) of the model proposed by Brodsky et al. Rapidities of collisions y_i are uniformly distributed in the central region of a typical h-h rapidity range.

(a) $\langle \text{Target-produced multiplicity} \rangle = \frac{\bar{v}}{2} n_c$.

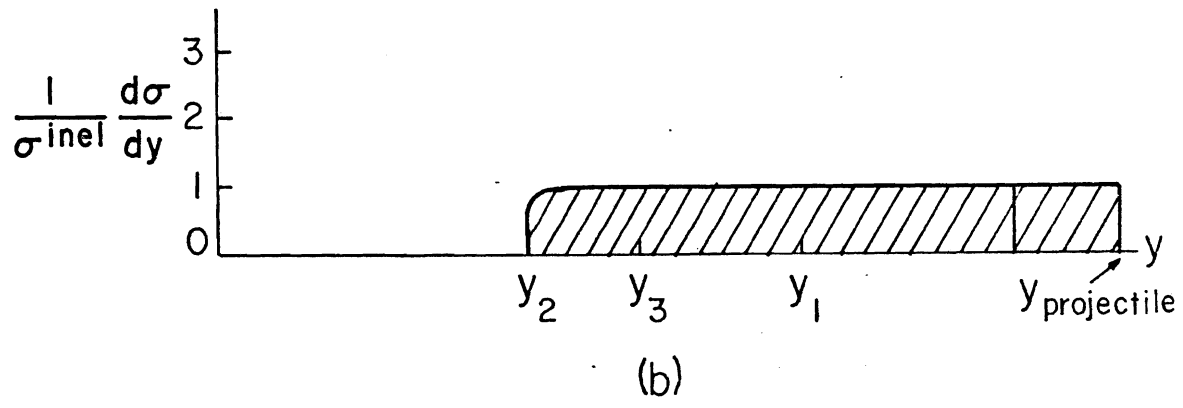
(b) $\langle \text{Projectile-produced particle multiplicity} \rangle$
 $= \frac{\bar{v}}{\bar{v}+1} n_c$.

(c) Total multiplicity = $(\frac{\bar{v}}{2} + \frac{\bar{v}}{\bar{v}+1}) n_c$

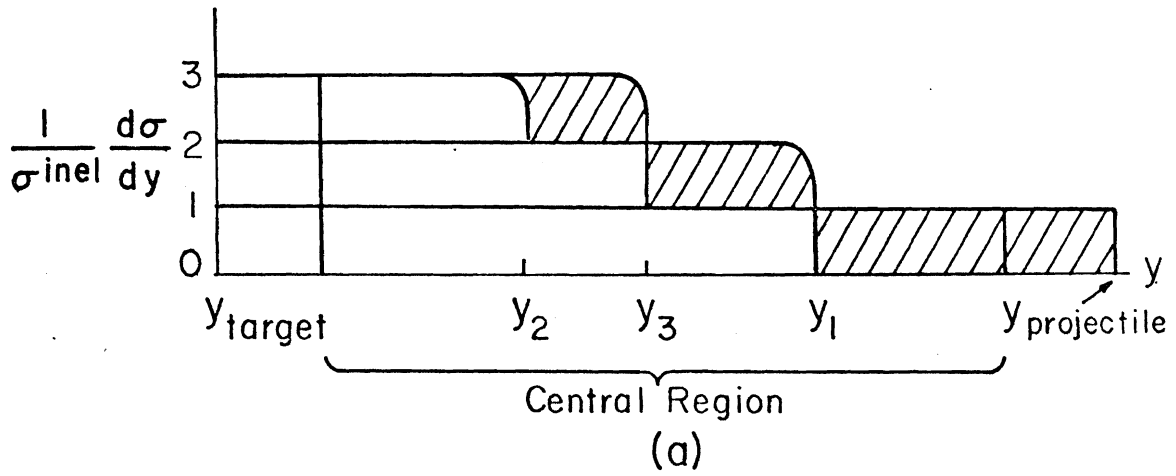
in the central region.



(a)



(b)



(a)

(II) Models Using Coherent Interactions with Nucleus.

The general feature of this class of model is the use of a completely different interaction mechanism. The h-A interaction is considered as a coherent interaction of the projectile with the target nucleus. In the interaction process, nucleons in the target nucleus are considered to act as a whole according to an undefined mechanism. Two of the models in this class that have been proposed in the current literature are (1) the coherent tube model and (2) a coherent interaction model proposed by G. Białykowski et al.

1: Coherent Tube Model (CTM)

The CTM (22~24) assumes that the nucleons in a tube of the incident particle path act as a single body with cross section σ (where σ is the inelastic h-h cross section) colliding simultaneously with the projectile with the CM energy s

$$S = A^{\frac{1}{3}}s = 2A^{\frac{1}{3}}m_p E \quad \text{where } A^{\frac{1}{3}} \text{ is taken as the number of nucleons in the tube;}$$

m_p = mass of nucleons, and E = incident energy.

In the CM system, the particle-tube collision is assumed to act as a particle-nucleon collision at the same center of mass energy S . Thus the high-energy hadron interacts with the nucleus (as shown in Figure 13) such that the incident particle interacts simultaneously with the array of $A^{\frac{1}{3}}$ nucleons of the target nucleus which lies on its path.

The rapidity distribution is dependent on target size, as predicted by CTM. The rapidity distribution of $h-A$ interactions rises slowly and expands in the direction of the target fragmentation, when compared to $h-h$ interactions at the same energy. When the energy increases, it rises and expands in the direction of the projectile fragmentation (as shown in Figure 14)

$$\frac{1}{\sigma_{hA}^{\text{inel}}} \frac{d\sigma_{hA}}{dy} (s, y) = \frac{1}{\sigma_{hp}^{\text{inel}}} \frac{d\sigma_{hp}}{dy} (A^{\frac{1}{3}}s, \frac{1}{6} \ln A + Y)$$

Also, the average multiplicity is predicted as

$$\langle n(E) \rangle_{hA} = \langle n(A^{\frac{1}{3}}E) \rangle_{hp}$$

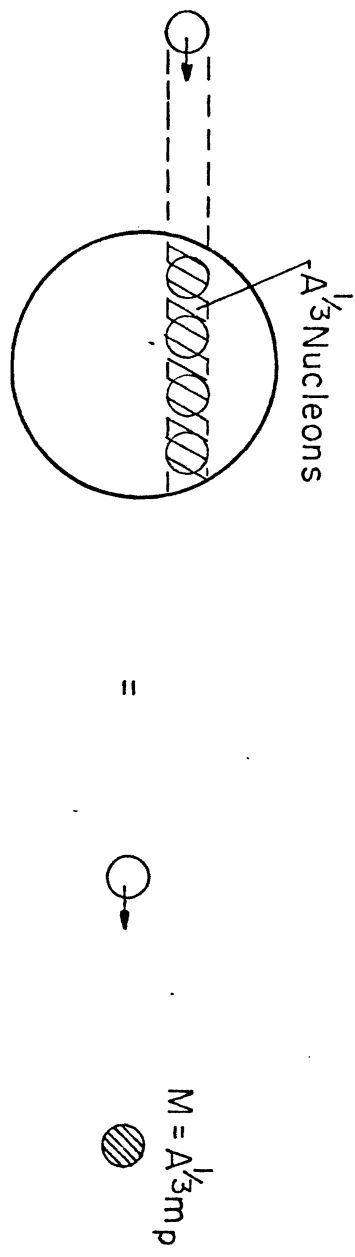
which implies that the scaled multiplicity distribution $\psi(z)$ in KNO scaling is universal to the nucleon and nucleus target

$$\psi_p(z) \approx \psi_A(z)$$

FIGURE 13.

In CTM, the incident hadron interacts with an array of nucleons lying on its path coherently as a hadron-hadron interaction at energy $A^{\frac{1}{3}}E$.

Hadron + Nucleus

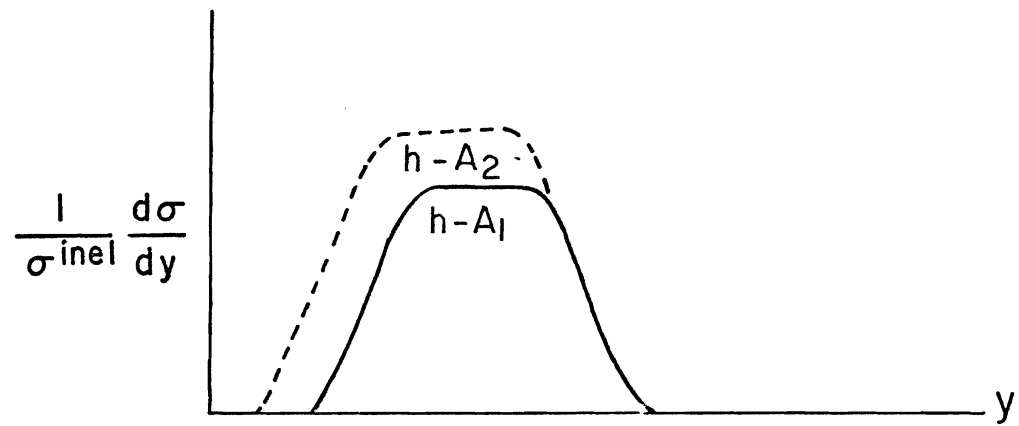


= Hadron + "Effective Hadron"

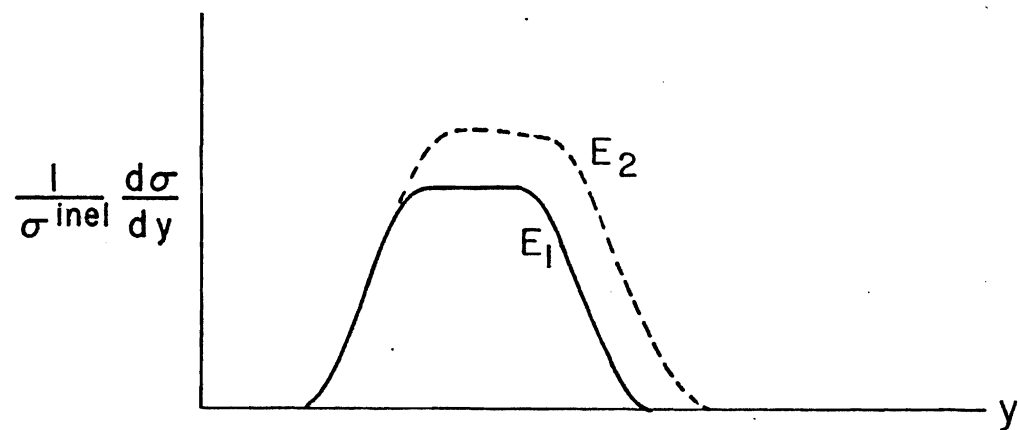
FIGURE 14.

Predictions of CTM about rapidity distributions

- (a) For different sizes of target, where $A_2 > A_1$, the rapidity distribution rises and expands toward the direction of target fragmentation.
- (b) For different energies, where $E_2 > E_1$, the rapidity distribution expands toward the direction of projectile fragmentation.



(a)



(b)

2: A Coherent Interaction Model by G. Bialkowski
et al.

In addition to the model discussed above, a model with a similar interaction mechanism has been proposed by G. Bialkowski et al. (25). This model considers that the particles in the nucleus at the instant of their creation are not only immature, but that their maturation rate is enhanced by the presence of other hadronic matter.

Some predictions made by this model, resulting from quantitative calculations, with the assumption of a uniform nuclear density, can be summarized as follows:

(i) the multiplicity ratio R is related to \bar{v} as

$$R \approx 1 + .52 (\bar{v} - 1);$$

(ii) the total inelastic cross section of h - A interactions is linearly dependent on $A^{\frac{2}{3}}$, and the coefficients are different for different types of projectiles; and

(iii) the behavior of the rapidity distribution with varying target nuclear size predicted in this model is very similar to that predicted by the CTM, with the central and target fragmentation regions rising and the maximum moving to lower rapidities when the target size is increased.

(III) Some Comments on Models.

In general, all the models mentioned in this chapter predict general features of h-A interactions fairly well. Each of them has some success in the predictions that it stresses; none of them, however, succeeds by itself in describing the interaction mechanism and predicting all interaction features in detailed discussion.

Several phase models are all similar in spirit, in that they divide the hadronic matter in the interaction into two components. The active component interacts with nucleons to form a cascade, while the passive component does not interact, but decays into secondaries. This leads one to predict a small multiplicity for h-A interactions. Also, models in this category are rather ad hoc, and are usually adjusted to fit the data. Thus, predictions are naturally not far from experimental results.

For the MPM, A. Capella and A. Krzywicki (16) have worked out the consequences of the picture described in previous discussions and find good agreement about rapidity distribution with data from W. Busza et al. (21) in the central region, but find disagreement in the projectile fragmentation region, where depletion is expected.

However, both the recent data on neutron-nucleus interactions (26) and the data from p-Em interactions at 67 and 200 GeV (10), parametrized according to equation (5) of the model of J. Babecki et al., do show depletion in the last two units. Other than this, the prediction of $\frac{D}{\langle n_s \rangle}$ in the MPM fits the data (16) within 10%.

The parton model described by S. J. Brodsky et al. provides only qualitative predictions about rapidity distribution. The predictions about the variable R as a function of \bar{v} are adjusted to fit the data. Furthermore, the parton model of N. N. Nikolaev discusses the interaction mechanism in more detail and gives predictions very close to those of the MPM. The differential inclusive cross section ratio R_y predicted in this model is reasonably in agreement with experimental data from p-Em interactions at 200 GeV (17). However, the prediction for R as a function of incident energy and target size does not seem to fit the data as well. One would need data over a wider range to decide on the problem of agreement.

With respect to the CTM, the multiplicity scaled function $\psi(z)$, which is independent of energy, has good agreement with both h-p and h-A data, except for large z values where $z \gtrsim 2.0$ (27). However, the predicted curves of the rapidity distribution do not seem to fit the data

very well. For example, the percentage of increase of the inclusive cross section in the central rapidity region for p-A interactions (22) is about 20% for $A = 1$ to $A = 70$, while the estimates based on the data of W. Busza et al. (21) give at least an 80% increase.

The coherent interaction model of G. Białykowski et al. fits the rapidity data very well with one parameter (25). Moreover, the linear relation of cross section σ_{hA}^{inel} with $A^{\frac{2}{3}}$ also agrees well with the data. The prediction of the multiplicity ratio R is very close to the predictions by EFC or TPM.

Except for the CTM, the models discussed seem to fit the data on rapidity distribution with some or no parameters. Some other features, such as R as a function of \bar{v} or s , scaled multiplicity distribution, or total inelastic cross section, are also discussed in some models. However, most of these features are only discussed qualitatively, with little said in detail about possible interaction mechanisms. Also, in the extant models, there is very little discussion of two-particle correlations-- a subject which is considered an important aspect of h-A interactions. To make distinctions between models, it is important to have more detailed theoretical calculations as well as more, and better, data from future experiments;

only this will allow us to eliminate as many models as possible, and help us get down to a very successful and predictive one.

CHAPTER III:

REFERENCES

1. K. Gottfried. Ref. TH 1735-CERN, CERN Preprint.
2. K. Gottfried. Phys. Rev. Lett. 32 #17, 957 (1974).
3. P. M. Fishbane and I. S. Trefil. Phys. Lett. 51B
#2 (1974).
Phys. Rev. Lett. 31 #11, 734 (1973).
Nucl. Phys. B58, 261 (1973).
Phys. Rev. D4, #1, 168 (1974).
4. A. Dar and J. Vary. Phys. Rev. D6, #9, 2412 (1972).
5. E. L. Feinberg. Phys. Report 5C #5 (1972).
6. A. S. Goldhaber. Phys. Rev. D7, 765 (1973).
7. G. Calucci, R. Jengo and A. Pignotti. Phys. Rev.
D10, 1468 (1974).
8. J. Babecki et al. Phys. Lett. 52B #2, 247 (1974).
9. Alma-Ata-Moscow-Tashkent Collaboration, Preprint N77,
Moscow (1977).
10. B. Furmanska et al., Preprint, Kraków (August 1977).
11. D. Amati, Nuovo Cimento 26, 896 (1962).
12. W. R. Frazer. Rev. of Mod. Phys. 44 #2, 284 (1972).
13. J. Koplik and A. H. Mueller. Phys. Rev. D12 #11,
3638 (1975).

14. L. Bertocchi. AIP Conference Proceedings #26 (1975).
15. J. H. Weis. Acta Physica Polonia B7, 851 (1976).
16. A. Capella and A. Krzywicki. Preprint LPTPE-77/16
17. N. N. Nikolaev. Review paper given in International Seminar on Particle-Nucleon Interaction, Miramere-Trieste, 10-15 June (1976).
18. S. J. Brodsky, J. F. Gunion and J. H. Kühn. Phys. Rev. Lett. 39 #18, 1120 (1977).
19. S. D. Drell and T. M. Yan. Phys. Rev. Lett. 25, 316 (1970).
20. P. V. Landshoff and J. Polkinghorn. Nucl. Phys. B32, 541 (1971).
21. W. Busza et al. Paper submitted to XVIII Int. Conf. on High Energy Physics, and preprint of lectures given at the VII Int. Colloquium in Multiparticle Research, Tutzing, June 21-25 (1976).
22. Y. Afek et al. Preprint Technion-PH-76-48 (1976).
23. G. Berlad, A. Dar, and G. Eilam. Phys. Rev. D13 #1, 161 (1976).
24. A. Dar and Tran Thanh Van. Preprint Technion PH-76-61.
24. G. Bialkowski, C. B. Chiu and D. M. Tow. Phys. Lett. 68B #5, 451 (1977).
25. D. Chaney et al. Phys. Rev. Lett. 40 #2, 71 (1978).

CHAPTER IV:
EXPERIMENTAL PROCEDURES

(I) Research With Nuclear Emulsions

1: Introduction

Using nuclear emulsion as a detector is a well developed photographic technique. The nuclear emulsion serves as an instrument of research for high energy physics in such areas as elementary particle studies, cosmic ray shower spectrum studies, and, recently, for studies of nuclear interactions from accelerator particles.

One of the most important features of the photographic method is that it records the tracks of charged particles and provides a permanent record which can be examined and reviewed at will under the microscope. Historically, nuclear emulsion has also been used as a detector for discovering new particles such as π^\pm , K^\pm , Σ^\pm , $\bar{\Lambda}$, etc. By examining the tracks with the microscope, the characteristics of the corresponding particle--charge, mass, velocity, etc.--can be obtained. Different particles can thus be differentiated. Recently, nuclear emulsion has often been used to detect very short-lived new particles, for example, in charmed particle searches (1), since only

nuclear emulsions will provide direct evidence of existence and permit a detailed analysis of the physical properties associated with these particles.

This method has its limitations. Both the background due to unrelated tracks and the distortion of the nuclear emulsion with a gelatine base make measurements hard to deal with. Also, the detection of events is very time-consuming. However, the double measurement technique (see Appendix I) is used to improve accuracy, and the newly developed electronic techniques are used for locating events. With the incorporation of scintillation counter, spark chamber (or drift chamber, or proportional chamber, or even the bubble chamber, as in an approaching experiment by University of Washington investigators), and various electronic devices, one can locate an event within 1 mm³.

2: Chemical Composition and the Mechanism of Track Formation

The basic components of nuclear emulsion are (i) silver halide, chiefly silver bromide (AgBr), sometimes with a small mixture of silver iodide (AgI); (ii) gelatin and a plasticizer, such as glycerine; and (iii) water. The silver halide is the photosensitive compound, and is

sensitive to either photons or fast-moving charged particles. It is embedded uniformly in the gelatin in the form of microcrystals or grains, of a shape that differs with manufacture and of a size varying with type of emulsion. Gelatin and plasticizer are the organic complex, with elements H, C, N, O, S, and water. These are light-transparent materials that provide a network to fix the AgBr (or AgI) crystals in position.

When the silver halide crystal absorbs energy from photons or fast-moving charged particles incident on it, the microcrystals may be conditioned by this experience so that, under the action of a chemical reducing agent, conversion of the halide metallic silver will proceed more rapidly than in an unirradiated crystal. This reaction produces a latent image which can be developed into a black spot (and is the so-called grain in the charged particle track). The track left in nuclear emulsion by a charged particle is a series of "grains" developed from the latent images. Since the energy that remains in the silver halide crystal traversed by the particle is responsible for latent image production, it is expected (2) that the grain density of the track would be nearly proportional to the energy loss of the charged particle.

3: Ionization Loss of Charged Particles, and Restricted Ionization Loss in Emulsion

For charged particles heavier than an electron, such as pions, kaons, or protons, ionization energy loss is the most important mechanism of energy loss. Ionization energy loss of a charged particle is caused by the interaction of electromagnetic radiation with matter. As the charged particle moves through the matter, it loses energy as a consequence of collision with atomic electrons. However, it is important to remember that the density effect (3) δ of the dense medium, and the shell correction (3) U for heavy elements at higher energy, decrease the interaction between the particle and the medium, thus decreasing the energy loss.

The full computation of the ionization energy loss per unit length $\frac{1}{\rho} \frac{dE}{dx}$, known as the Bethe-Bloch formula (3,4), for a particle with a charge z and mass m moving with a velocity v , can be expressed by

$$- \frac{1}{\rho} \frac{dE}{dx} = \frac{2\pi n z^2 e^4}{\rho m v^2} \left[\ln \frac{2m v^2 W}{V^2 (1-\beta^2)} - 2\beta^2 - \delta - U \right]$$

where n = number of electrons per unit volume
in stopping substance;
 $\beta = v/c$;

V = mean excitation potential of the atoms
of the substance; and

W = maximum energy transfer from the in-
cident particle to the atomic elec-
trons.

The highest energy exchange to an atomic electron which can be detected in nuclear emulsion W_0 is $W_0 \sim 5$ KeV (3). Thus, for grain count in emulsion, the relevant quantity is the restricted ionization loss, which is the ionization loss with energy transfer less than W_0

$$I = - \frac{1}{\rho} \frac{dE}{dx} \Big|_{W = W_0}$$

and the grain density along the track is proportional to I

$$g \propto I$$

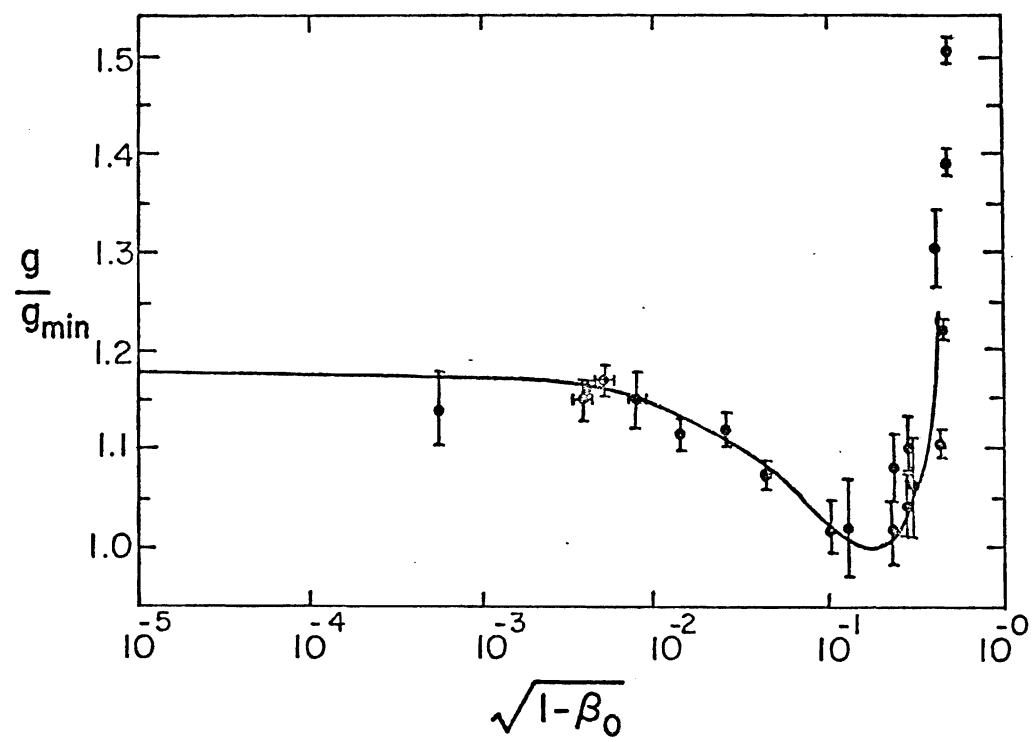
Shown in Figure 15 is the ratio of the grain density to that at the minimum of ionization derived from K5 emulsion measurements (5).

4: Special Features

Nuclear emulsion is very different from the ordinary emulsion employed by conventional photography. The main differences are that in nuclear emulsion the ratio

FIGURE 15.

The ratio of the grain density to that at the minimum of ionization loss, derived from K5 emulsion measurements.



of AgBr is ~ 8 times higher than in conventional emulsion; also, nuclear emulsion is not very sensitive to changes in the degree of development. In addition, the emulsion layer used in experiments is always thick--about several hundred μ .

Many types and series of nuclear emulsion (2) are produced by commercial organizations. Nuclear emulsions differ in either grain size or sensitivity of the particle energy range for different research purposes. Ilford G5 and K5 emulsions are similar in type except for grain size. Both of them are used for recording relativistic particles. (For more detail, see section III (1).)

(II) Apparatus Set-Up.

The apparatus used to detect high energy hadron-nucleus collisions is made of nuclear emulsion plates with the pure element confined inside. Each emulsion plate has granules of a particular heavy element as targets for high energy particles. After being bombarded by the beam particles, the emulsion records all the tracks of charged particles, including the charged particles emitted from the hadron-nucleus interactions.

Some advantages of using the nuclear emulsion as a detector for nuclear interactions in this experiment

--which are not obtained with hydrogen bubble chamber or counter experiments--are as follows.

(i) It allows direct observation of events in 4π solid angle, so that one can study the nuclear interaction in detail.

(ii) It makes extreme accuracy of distance and angle measurement possible, such that very fine spatial resolution and good precision can be obtained.

(iii) It can detect very short term behavior (up to microns), so that very short-lived particles can be observed and their life spans measured.

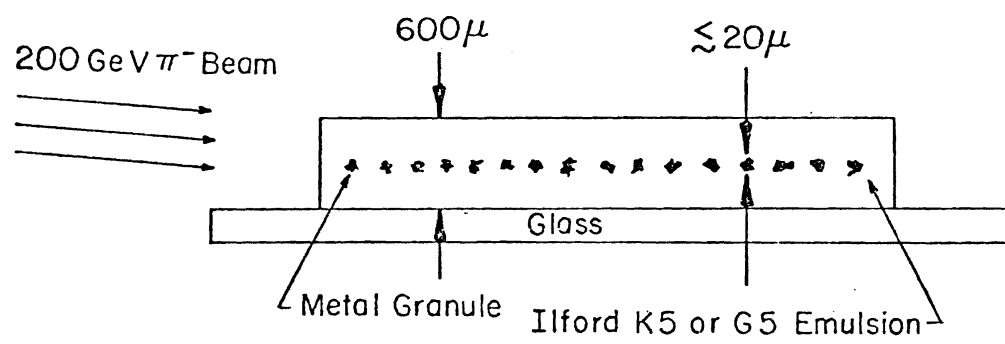
The emulsion plate, as shown in Figure 16, is composed of an element-emulsion sandwich on top of a glass plate. The element-emulsion sandwich is constructed of two layers of 300μ thick nuclear emulsion and a target layer, which is pure element powder of $\leq 20\mu$, embedded between the two emulsion layers. The target layer is in the shape of granular clumps, scattered separately throughout the emulsion gelatin.

1: Size and Material Used

All plates are made up on $5" \times 4\frac{1}{2}"$ Ilford treated glass plate. Dimensions of the element-emulsion sandwich are $4" \times 4" \times 600\mu$. The average diameter for each

FIGURE 16.

Nuclear emulsion plates with embedded metal granules.



element clump embedded is $\lesssim 20\mu$. The emulsions used are Ilford K5-gel and G5-gel. The main difference (2) between them is the size of the grains in the track caused by the charged particle when it passes through. Ilford G5-gel is an electron-sensitive emulsion, and the grains are therefore coarse, with diameter around $.3\mu$. K5-gel emulsion is similar in type to the G series except for the diameter of the grains, which is approximately $.15\mu$. Because of the coarse grain of G5, the hadron-nucleus interaction events in the G5 plates are more prominent and easier to find, although the background in the plate is darker. However, K5 plates provide more precise measurements because of the small grain size in the minimum ionization tracks.

For the target elements, Cr, W, Ag and AgBr powder are used for investigating the differences in interactions with the variation of nuclear target size (or the atomic mass A). The amount of the seived element powder used per plate is $\sim .4g$. This turned out, after many trials, to be the optimum amount for giving the maximum possible number of events while avoiding a clump density that would hinder scanning efficiency and measurement precision.

Besides the element powder plate, some gelatin-emulsion sandwich plates are also prepared with three layers: emulsion 200 μ , gelatin 50 μ , emulsion 400 μ (from top to bottom).

2: Technique

The preparation of the element loaded emulsion plates can be divided into two steps: (i) mounting the lower layer of emulsion onto glass plate as the base, and (ii) loading the element and adding the top layer of emulsion.

(i) A large, cold, flat metal surface is needed to cool the plate down and coagulate the liquid emulsion. The clean glass plate was put on top of the metal surface, with $\frac{1}{2}$ " square cross section brass dikes on it for the 4" x 4" emulsion pool. Meanwhile, Ilford G5- and K5-gel was put in an ultrasonic cleaner at $\sim 40^{\circ}\text{C}$. After the emulsion was melted, a small pitcher was used to pour the liquid emulsion onto the pool and make it flow over the surface of the plate (diluted with 10~15 cc of water if too thick). The induced bubbles that occurred were removed by suction right after pouring, since bubbles will cause curvature of the emulsion after coagulation.

After one layer was mounted on each glass plate, all the plates were left in a drying box. The door to the

box was left open, and a fan ~15' away was allowed to blow air directly to the plates. The dark-room radiator was on to bring the temperature to 80°F. Drying time was around 15~20 hours.

(ii) After the lower layer of emulsion was dried, various seived metal powders were put on the surface of the emulsion by the slurry method, a special technique developed by the Cosmic Ray Laboratory at the University of Washington:

(a) The surface of the base emulsion was wetted with tap water by puring the water over the surface.

(b) About one minute later, a slurry of a given element was poured over the wet surface.

Since most metals, especially tungsten, are much more dense than water, the following method was use to give a uniform dispersion. The metal powder was put, along with about 100 cc of water, in a 250 cc beaker. The beaker was subjected to a swirling motion until the powder was mixed with the water. This was kept up until a moment before pouring over the emulsion layer.

After coating the emulsion with metal powder, the damp emulsion was allowed to dry for a few minutes, and then the top layer of the emulsion was mounted using the

same technique described in part (i).

3: Exposure to the 200 GeV π^- Beam

The emulsion plates were packed in stacks and exposed to 200 GeV negative pion beams at National Accelerator Laboratory in June, 1975. Each plate was impinged on by the beam particles in the manner shown in Figure 16. Various exposures at differing track densities were tried on different stacks to find the optimum track density in terms of the balance of the background and the number of events expected. 32k, 48k, 60k, and 73k per square centimeter were tried. $73k/cm^2$ gave the best results.

4: Grid Printing and Developing the Plates

Grids were printed at the bottom of emulsion layers to help in locating each event on the plates. For all types of emulsion used, printing took 7 seconds at 85 volts. Afterward, emulsion plates were developed as follows:

1. Soak in cold water at $5^\circ C$ for 2 hours.
2. Soak in Amidol at $5^\circ C$ for 2 hours.
3. Warm develop at $22^\circ C$ for 1 hour.
4. Stop bath at $5^\circ C$ for 2 hours.
5. Fix at $5^\circ C$ for 70 hours.

6. Wash at 5°C for 72 hours.
7. Alcohol + 5% glycerine at 5°C for 2 hours.

(III) Scanning and Measurement.

1: Events

Of the available emulsion plates, 5 chromium and 2 tungsten plates have been scanned. A typical event is shown in Figure 17 with the 200 GeV π^- coming in as a minimum ionized track in the emulsion, interacting with the nucleus inside the element granule, where secondaries are emitted. Only tracks of the charged particles are shown in the emulsion. The secondaries can be classified into two groups by degrees of ionization (I):

Shower particles $I \leq 1.4 I_0$, where I_0 = minimum ionization;

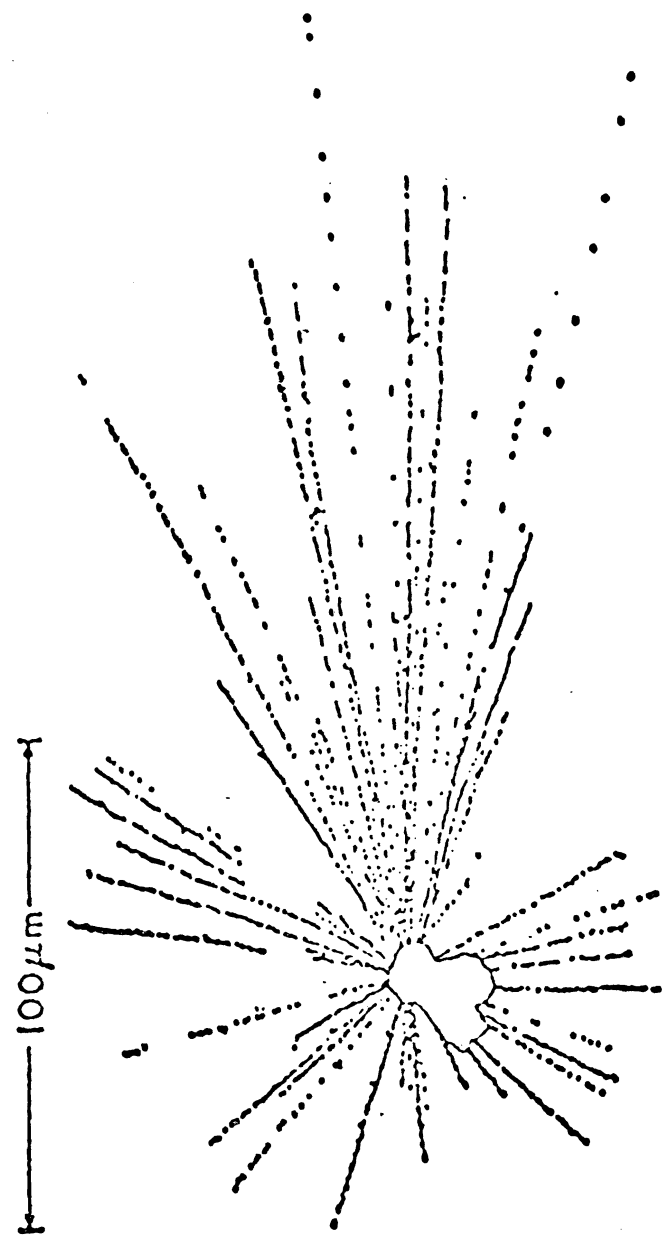
Heavy track particles $I > 1.4 I_0$; and

(Gray-track particles $6.8 I_0 > I > 1.4 I_0$).

(i) Shower particles are the particles that leave the minimum-ionized tracks and are pretty much collimated in a forward cone. They correspond to the fast particles, with velocity $\beta \geq 0.7$. Most of the energy is carried by the shower particles, including pions, kaons, and fast protons. More than 80% are pions (6).

FIGURE 17.

A picture of a typical pion-nucleus interaction in nuclear emulsion plates.



(ii) Heavy-track particles are often divided into grey- and black-track particles. (a) For black track particles, energy and angular distribution are very similar to what is expected for thermal excitation processes in the interaction. They are low energy mesons, protons, or nucleus fragments emitted from the excited target. (b) Grey track particles are believed to be associated with the recoil particles (7).

The number of heavy tracks (N_h) (or the number of grey tracks (8) (N_g)) is closely related to the average number of collisions \bar{v} that have happened inside as a result of the projectile traversing the nucleus (9). The number of tracks (either heavy or grey) often serves as a measurable indicator of the degree of target excitation.

2: Scanning

All the scanning was carried out with the Leitz binocular microscope at 55 power with immersion oil. While searching the events, a certain area of plate was area-scanned. In order to prevent missing any events, the microscope was focused all through the granular layer vertically. Also, rescannings were performed all over the scanned area for possibly missed events, and to

calculate scanning efficiency. These are the criteria used to identify an event:

(i) There exists an incoming ionized track which is parallel to the beam track;

(ii) The interaction vertex, which can be centered on from the heavy tracks, is in the granule--events with the vertex on the edge of the granule are discarded for lack of confidence;

(iii) There are shower particles among the outgoing particles; heavy tracks are only the evaporation of the target;

(iv) Coherent events are also discarded. Such events (10~12) are produced by projectile break-up or an electromagnetic process rather than a hadronic interaction. Most 3-pronged white events ($N_h = 0$) found in our experiment turned out to be coherent. Because of the small momentum transfer in the coherent interaction, the coherent event is characterized by very strong collimations of secondary particles without any destruction, or recoil target, being visible. Also, the three emergent tracks are nearly coplanar, with the middle track showing no detectable deflection from the primary. All the events found were double-checked by the Koristka microscope for the above-mentioned requirements.

3: Measurement

The measurement work was done with the Koristka microscope with which the X , Y , and Z value of a specific point can be read to a micron. Grain counting is used to distinguish the shower tracks from the heavy tracks, although they can be distinguished by eye right away in most cases. The method of grain counting is as follows. The primary is taken to be the minimum ionized track with grain density $g_0 \approx 15$ grains/ 80μ , varying slightly in different plates. Since the grain density (g) is proportional to the ionization of the corresponding particle, we can also differentiate the shower tracks by counting the grain density of the track, since $g_{\text{shower}} \leq 1.4 g_0$.

Before measuring each event, it is necessary to follow the primary track all the way through to make sure that it is not a secondary event. The spatial measurement (see Appendix I) is then carried out by regular measurement or double measurement, depending on the curvature of the emulsion.

(i) In regular cases, the emulsion shrank almost uniformly while drying and the primary could be aligned with the horizontal axis of the scope. Positions of the vertex, primary, and each of the shower tracks are

measured.

(ii) Double measurement is used when the emulsion about the event is very curved such that the primary can not be aligned well with the scope coordinates. Double measurement is used to improve measurement accuracy by choosing a minimum ionized track, which is parallel to and as close as possible to the primary, to be a reference coordinate.

In addition to the spatial measurement, the number of shower particles (N_s) and the number of heavy tracks (N_h) of each event are also counted.

4: Shrinkage Factor

Emulsion shrank after it was developed, so that the field of view of a microscope does not correspond to a true plane in the object. In general, two points in focus in different parts of the field are not at the same depth in the emulsion, but differ by a shrinkage factor (SF). The shrinkage factor can be derived by measuring the emulsion thickness by a micrometer caliper before and after developing at several spots, since the emulsion is often curved and the shrinkage factor varies slightly from spot to spot. It is found that the average shrinkage factor, which is a dimensionless ratio, is

$\langle SF \rangle = 2.51 \pm .05, \sigma = .13$ for G5 emulsion;
 $= 2.21 \pm .06, \sigma = .15$ for K5 emulsion;
 where σ is the standard deviation.

In the calculations for data analysis, this factor is taken into account for the correction of the vertical measurements.

(IV) Methodology

1: Event Selection

After all the events that could be found were measured, it was necessary to select those that qualified as 200 GeV π^- events for analysis, and discard the abnormal events--those not definitely induced by the π^- beam particles. The events that qualify as π^- -nucleus events are differentiated from the abnormal ones by their dip angles.

In each plate, the distribution of the dip angle θ for primaries is assumed to be normally distributed about its mean value $\bar{\theta}$, with the standard deviation D

$$dP = \frac{1}{D\sqrt{2\pi}} e^{-(\theta-\bar{\theta})^2/2D^2} d\theta$$

The dip angles of the π -nucleus events are expected to fall around the mean dip angle $\bar{\theta}$. Thus, cut-offs were made at $\bar{\theta} \pm 2D$, and events with dip angle outside the

range $\bar{\theta} - 2D \leq \theta \leq \bar{\theta} + 2D$ were excluded and discarded for lack of confidence that they were induced by the 200 GeV π^- beam particles. The same process of discarding was repeated on the remaining events until there were no more abnormal events appearing. By doing this, we obtained at least 95% confidence (13) that the events remaining were 200 GeV π -nucleus interactions.

Of the events measured, three out of the 56 π -W events, and six out of the 63 π -W events, were excluded. Thus, only 53 π -W events and 57 π -Cr events in this experiment were analyzed.

2: Efficiency

Most measurements of high energy nuclear interactions are made statistically. In nuclear emulsion experiments, in order to get a random sample, one attempts to detect all the events of interest in a specific region of nuclear emulsion. Unfortunately, missing events, especially those light events with only a few heavy tracks, is inevitable. To improve the statistics, and minimize the systematic error, rescanning was performed on all the areas scanned in different emulsion plates, except for some small areas by the edges, which cannot be overlapped exactly in the two scannings. Rescanning was done as carefully as the

first scanning in order to prevent any scanning bias.

The scanning efficiency (14) for the two scannings can be estimated from the number of events found and missed (see Appendix II). In this experiment, a total of 105 events were found in the areas overlapping in the two scannings. 26 were missed in the first scanning and 5 in the rescanning.

If the assumption is made that all the events have a similar intrinsic probability of being detected, from Appendix II it is found that 75% is the scanning efficiency for the first scanning and 94% for the rescanning. The true number of events occurring in these regions was also estimated as ~ 106 , which is very close to what was found.

However, the assumption made above is not quite adequate. In scanning, it is noted that events with lower N_h value are easier to miss. Thus, for a better estimation of scanning efficiencies, events were divided into two groups with (a) $N_h \leq 3$ and (b) $N_h > 3$. It would be more reasonable to assume that the probability of being detected for all events with $N_h \leq 3$ is equal, and that all the events missed belonged to the group of $N_h \leq 3$. In this case, among the 36 events with $N_h \leq 3$ found in

two scannings, 12 were missed in the first scanning and 5 were missed in the rescanning. With the same calculations as before, scanning efficiency of the first scanning for events of $N_h \leq 3$ is 61%, and the rescanning efficiency 79%. The true number of events is estimated at 39. (See summary in Table I.) For events with $N_h \geq 3$, the scanning efficiency is 100% in rescanning. Thus, in the data analysis, the efficiency for events of $N_h \leq 3$ can be used to correct some sensitive variables.

TABLE I.

Summary of the scanning efficiencies for first and second scannings.

TABLE I

(a) For all N_h

	Total number of events found in two scannings	Events Missed	Scanning efficiency	Estimated true total number of events
First scanning		26	75%	
	105			106
Second scanning		5	94%	

(b) $N_h \leq 3$ only

First scanning		12	61%	
	36			39
Second scanning		5	79%	

CHAPTER IV;

REFERENCES.

1. Deep-Inelastic Interactions of Tagged 150 GeV Muon in Nuclear Emulsion Targets, Cornell-FNAL-Kraków-MSU-Seattle Collaboration E.382, Private Communication.
2. Powell, Fowler and Perkins. The Study of Elementary Particles by the Photographic Method. Pergamon Press (1959).
3. L. Marton, Editor in Chief. Method of Experimental Physics, Nuclear Physics, 5A, Academic Press (1961).
4. B. Rossi. High Energy Particles. Prentice-Hall, Inc. (1952).
5. Walter H. Barkas. Nuclear Emulsion Research, Academic Press (1963).
6. J. Whitmore. NAL-Pub-73/70-Exp (1973).
7. I. Otterlund. Cosmic Ray Physics Report LUIP-CR-76-07 (1976).
8. Alma-Ata-Moscow-Tashkent Collaboration, preprint N77, Moscow (1977).
9. B. Furmanska et al. Preprint, Kraków (August 1977).

10. S. Konishi et al. Phys. Rev. D13 #7, 1826 (1976).
11. Alma-Ata-Budapest-Kraków-Dubna-Sofia-Tashkent-Ulan Bator Collaboration, Proc. 11th Int. Conf. on Cosmic Rays, Budapest (1969).
12. J. E. Butt and D. T. King. AIP Conf. Proc. #12, Particle and Field Subseries #4.
13. L. Marton, Editor in Chief. Method of Experimental Physics, Nuclear Physics, 5B, Academic Press, New York (1961).
14. C. J. Waddington. Supp. Nuovo Cimento 19, 37 (1961).

CHAPTER V:

RESULTS

In this experiment, the results of the data, analyzed from the 57 events of 200 GeV π -Cr interactions, and 53 of π -W, can be analyzed as follows.

(I) Multiplicity Distributions.

1: Shower Particle Multiplicity Distributions

The distribution of shower particles for all tungsten and chromium events is plotted separately in histograms in Figure 18. Numbers of events are given with bin width 5. This is similar to that found in the experiment with the proton beam (1). The shower particles of tungsten events spread out over a wider range than those of chromium, with the average multiplicity $\langle n_s \rangle$ and the dispersion (D) of the distributions being

$$\langle n_s \rangle = 14.58 \pm 1.01, D = 7.35 \text{ for } 53 \pi\text{-W events;}$$

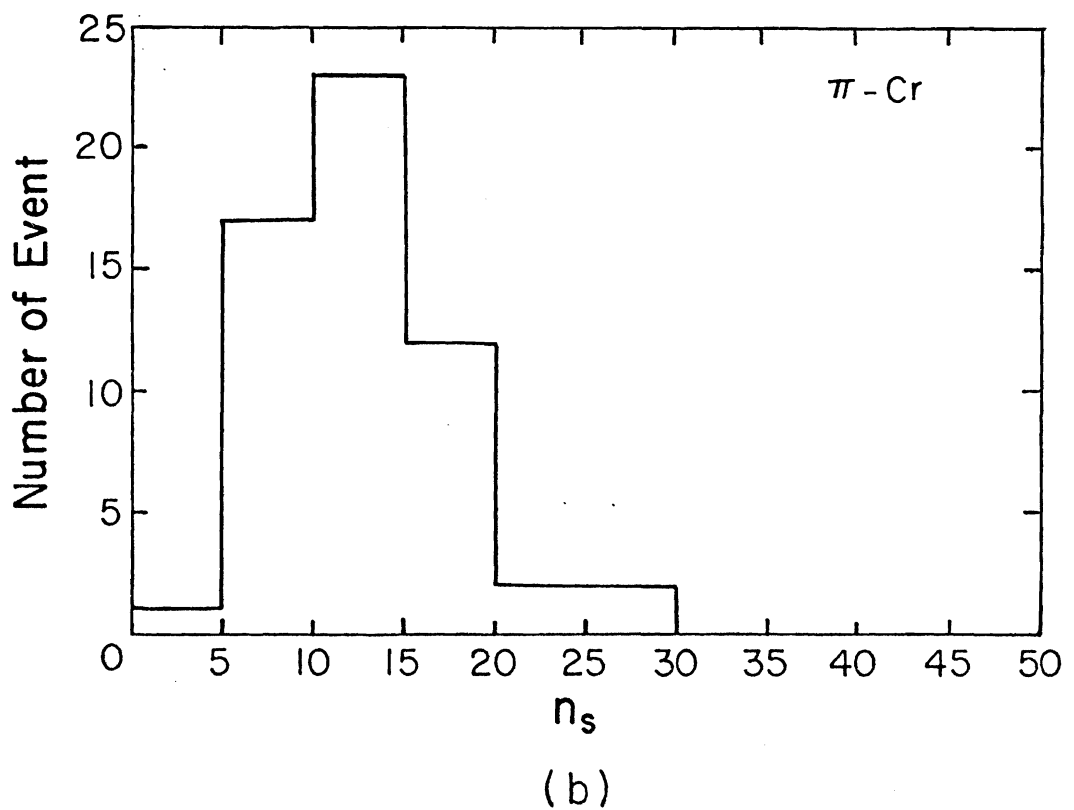
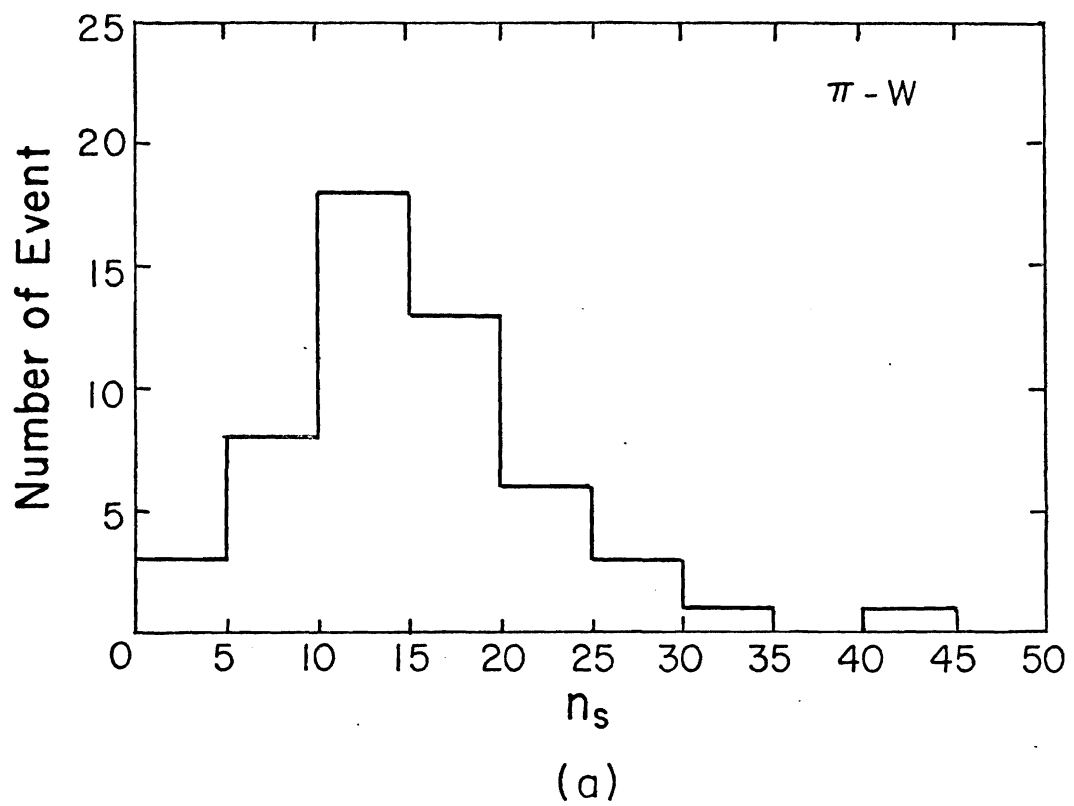
and

$$\langle n_s \rangle = 12.53 \pm .64, D = 4.83 \text{ for } 57 \pi\text{-Cr events.}$$

The dispersions are larger than $(\langle n_s \rangle)^{\frac{1}{2}}$. Thus, for both sets of events, shower particles are distributed more

FIGURE 18.

Histograms of multiplicity distributions for (a)
 π -W and (b) π -Cr interactions at 200 GeV.



broadly than a typical Poisson distribution.

2: The Scaled Multiplicity Distribution

The KNO scaling function ψ ($z = \frac{n}{\langle n \rangle}$, the scaled multiplicity distribution on the scaled variable $z = \frac{n}{\langle n \rangle}$, is a universal function independent of incident energies E for the hadronic interactions. In some previous experiments using protons as projectiles on either nucleon or nucleus targets (2,3,4), data has shown that the scaled multiplicity distributions are satisfactorily described by the Slattery function (see Chapter 2, section I5). Similar behavior, shown in Figure 19, is observed for pion as projectile. Figure 19 shows the scaled multiplicity distribution of the tungsten and chromium events from this experiment, including the data from π -p interactions at 205 GeV from bubble chamber (5) and the data from pion-emulsion (π -Em) interactions at 16 GeV (6). Also included are the data from π -Ne collisions at 10.5 GeV and 200 GeV (7). All the data points have been normalized to make the area beneath the curve equal to 1. The solid curve shown is the least square fit of a function, similar to that of Slattery, to π -p data, while the dash curve is for both tungsten and chromium data. The coefficients and χ^2 of both the

FIGURE 19.

Scaled multiplicity distributions, where $Z = \frac{n_s}{\langle n_s \rangle}$,
and $\psi(Z) = \langle n_s \rangle P_n$. The solid line is the least square
fit of Slattery type function for π -p data, and the
dash line is for the W and Cr data from this experiment.

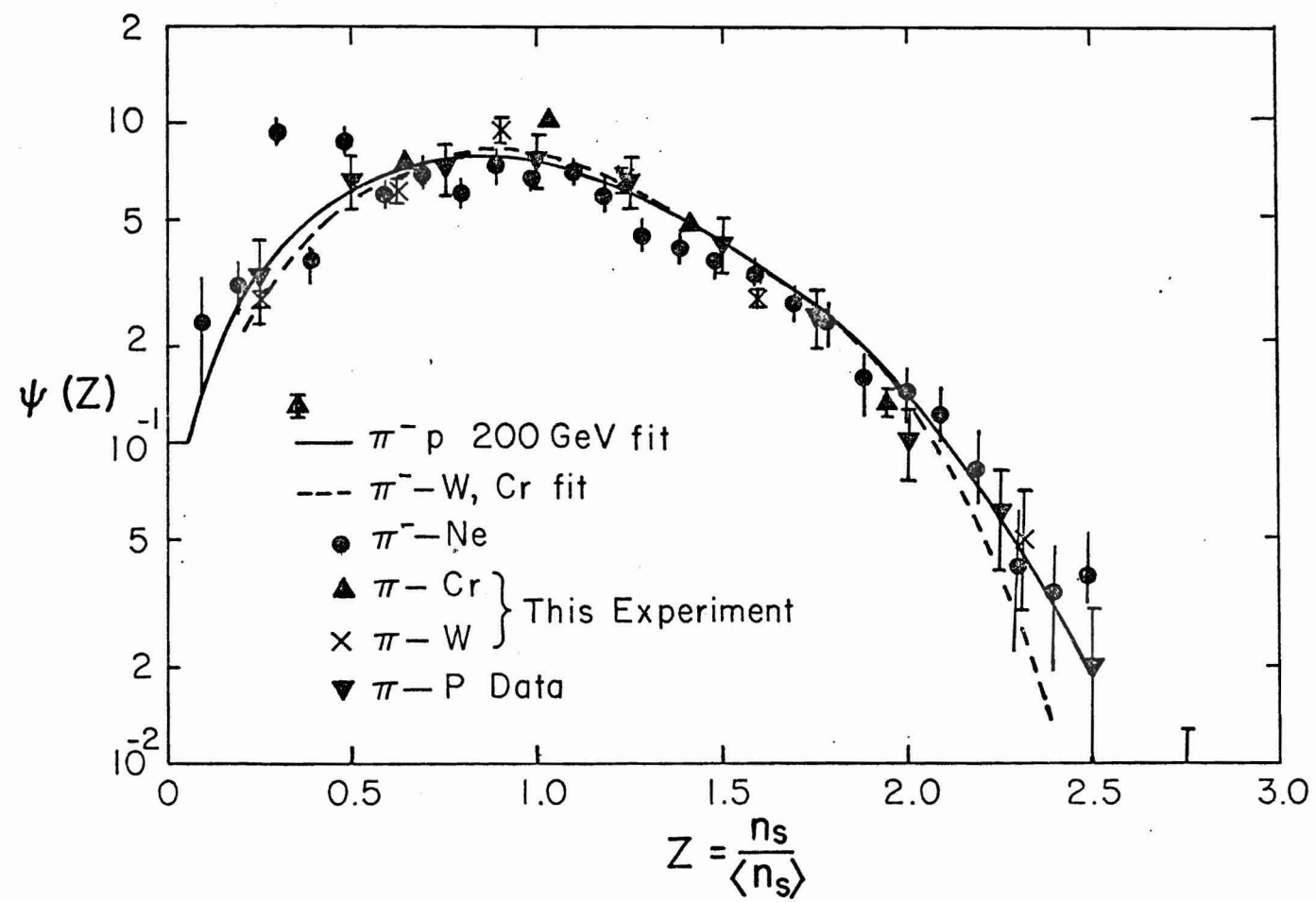
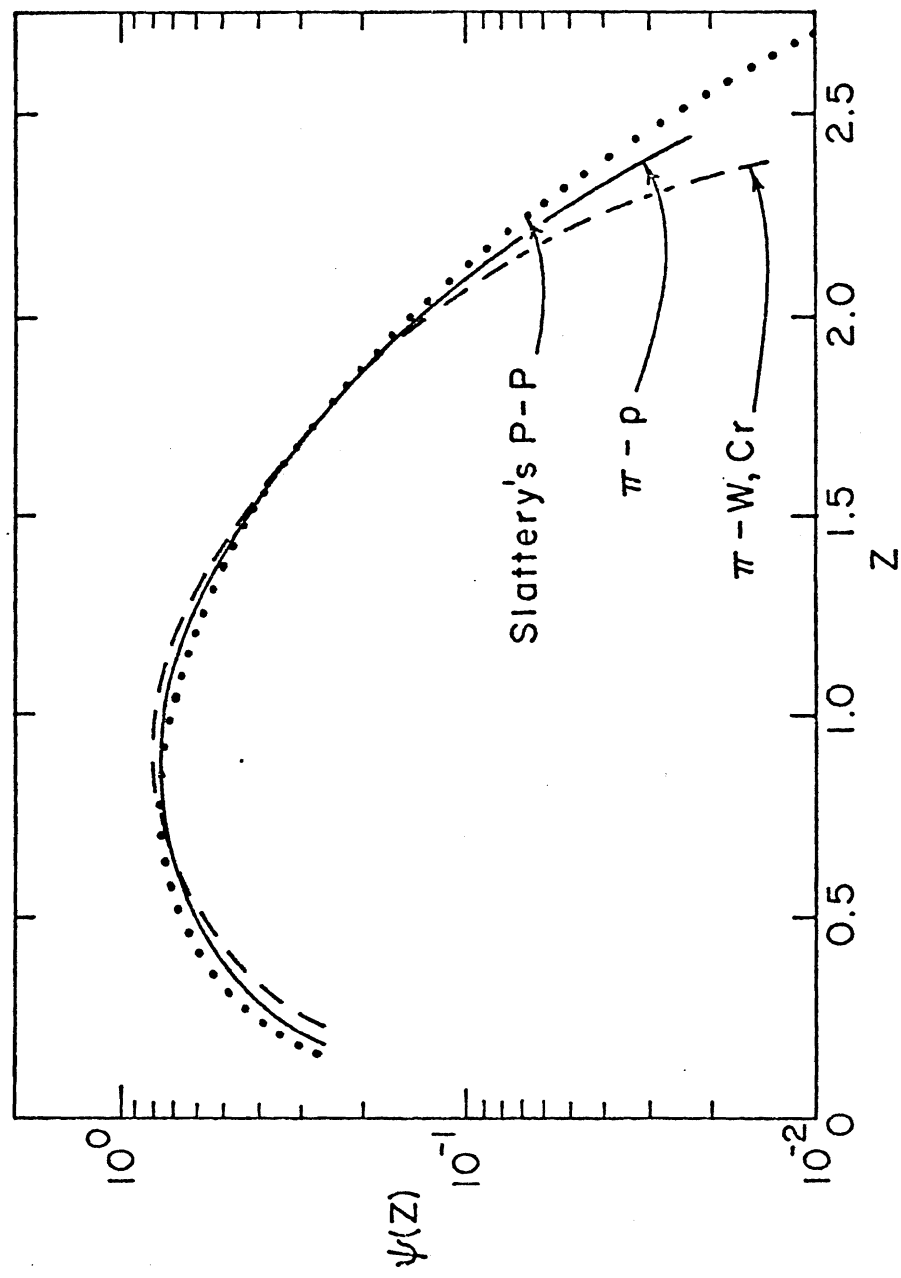


FIGURE 20.

A comparison of least square fit of Slattery type function for π -p (solid line) and π -nucleus from this experiment (dash line) with Slattery's function (dot line) for p-p interactions.



equations are summarized in Table II. The two curves are very close together except for those of larger Z values. The curve for tungsten and chromium tends to bend in after $Z \gtrsim 2.0$. It should be noted that this is a least square fit which lacked data points for $Z \gtrsim 2.0$ and $Z \lesssim 0.5$. This fact seems to agree with the predictions of the CTM and MPM; from the observations, the scaled multiplicity distribution seems to be universal to the incident energies that can be obtained, and for different sizes of target, within 10~15% error in the data range of this experiment, and the error is smaller than the data fluctuation.

It should also be noted that the difference of function $\psi(Z)$ for different types of projectile is very small. Figure 20 shows the area-normalized Slattery curve for p-p interactions in comparison with curves for π -p (5) and π -W,-Cr interactions (observed in this experiment). They are almost equal within the limit of experimental error.

For the scaling hypothesis to be valid, the moments of the multiplicity distribution should be independent of energy, and the ratio of the second moment D to the average $\langle n_s \rangle$ of multiplicity distribution, $D/\langle n_s \rangle$, is expected to be constant with $\langle n_s \rangle$. The previous

TABLE II.

Coefficients of the least square fit of the function
for scaled multiplicity distribution (after Slattery)

$$\psi(z) = (Az + Bz^3 + Cz^5 + Dz^7) \exp(-EZ)$$

for π -nucleus and π -p interactions at 200 GeV.

TABLE II

	A	B	C	D	E	χ^2/DF
Slattery function	3.79	33.7	-6.64	.332	3.04	
π -p	1.915	12.36	-3.105	.194	2.705	.026/11
π -W, Cr	.052	23.21	-5.837	.332	3.025	.21/9

statement is found to be true for interactions using protons as the projectile. Also, p-p data has been compiled by A. Wróblewsky (8) for the energy range $4\sim 303$ GeV, who also determined the relationship of the second moment $D = (\langle n_s^2 \rangle - \langle n_s \rangle^2)^{1/2}$ and the average multiplicity $\langle n_s \rangle$

$$D = (.576 \pm .008) (\langle n_s \rangle - 1)$$

This also agrees with recent data about p-p collisions from ISR (9) at energies up to $\sqrt{s} = 62.8$ GeV. As for the second statement, it has also been observed from the data from p-nucleus (1) and p-emulsion (3,10) interactions at different energies that the ratio $D/\langle n_s \rangle$ is almost equal to $1/2$, which is very close to that which is found for p-p, and a linear relation is also observed with the slope close to that of p-p data, within present experimental error.

In the experiments using pions as projectiles, different measurements (5,7,11~13) for different nucleon and nucleus targets have been compiled by W. Busza (2) and A. Wróblewsky (8) for the energy range $50\sim 205$ GeV. These values, along with the efficiency corrected data (see Table III) from this experiment, are shown in Figure 21. Since the value of D is very sensitive to the possible

TABLE III.

Some measurements corrected by scanning efficiency.

TABLE III

Interaction	$\langle n_s \rangle_{\text{experiment}}$	$\langle n_s \rangle_{\text{corrected}}$	$D_{\text{exp.}}$	$D_{\text{corr.}}$	Number of event
					Exp. Corr.
π -W	14.58 ± 1.01	14.05 ± 1.00	7.35	7.50	53 56
π -Cr	$12.53 \pm .64$	$12.00 \pm .68$	4.83	5.24	57 60

FIGURE 21.

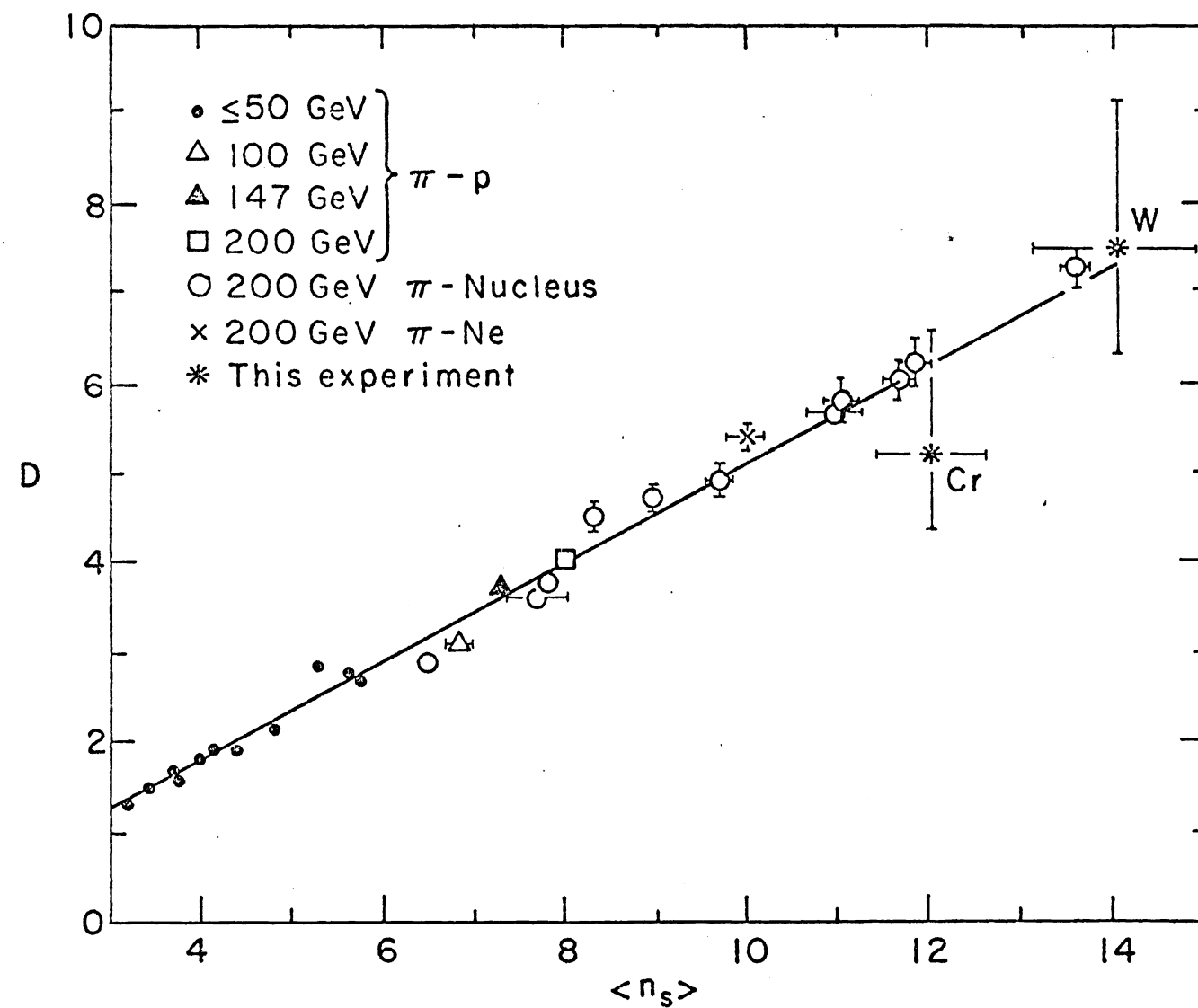
Data and linear least square fit of data for D vs.

$\langle n_s \rangle$ where

$$D = \sqrt{(\langle n_s^2 \rangle - \langle n_s \rangle^2)}$$

π -W and π -Cr data from this experiment are indicated.

Others are π -p and π -nucleus data at different energies compiled by W. Busza and Wróblewski (8).



scanning bias of events with lower multiplicity, missing events with low multiplicity tend to reduce the value of D. Thus it is believed that the experimental results represent lower limits for this quantity. To correct the data by scanning efficiency for events with $N_h \leq 3$, an overall efficiency of 80% is used in the calculation for both chromium and tungsten events with $N_h \leq 3$.

The solid line is the linear least square fit for all the data points (see Figure 21)

$$D = (.552 \pm .015) \langle n_s \rangle - (.408 \pm .127)$$

$$\text{with } \frac{\chi^2}{\text{DF}} = \frac{.376}{27}$$

which gives a similar slope to that of the data for interactions with protons as projectiles.

3: R vs. \bar{v}

The dependence of the ratio R, where

$$R = \frac{\langle n_s \rangle_{\pi A}}{\langle n_s \rangle_{\pi p}}$$

on \bar{v} , is important for differentiating predictions made by different models. The value of the average multiplicity of π -p interactions at 200 GeV is taken from the

bubble chamber experiment (5) as $\langle n_s \rangle_{\pi p} = 8.02 \pm .12$, and \bar{v} is taken as the average number of collisions estimated in certain models as

$$\bar{v} = \frac{A\sigma_{\pi p}^{\text{inel}}}{\sigma_{\pi A}^{\text{inel}}}$$

It is found that for 200 GeV, π -p collisions, within acceptable accuracy (5,12~14), $\sigma_t \approx 24.2$ mb, and $\sigma_t^{\text{inel}} = 21.2$ mb. The inelastic cross section of hadron-nucleus collisions (σ_{hA}) has been studied by S. P. Denisov et al. (14) at Serpukhov in the 6~60 GeV/c momentum range. It was found that, very much as in hadron-hadron interactions, the inelastic cross sections for pion, kaon and proton as incident particles are also independent of energy for $P > 20$ GeV/c. Other than this, the inelastic cross section for π^+ and π^- are equal within the measurement error. The dependence of σ_{hA} on the mass number of the target A for pion projectiles could be well described by the power function

$$\sigma_{\pi A} = 28.5 A^{-7.5}$$

Thus, \bar{v} is related to A as

$$\bar{v} = .744 A^{-2.5}$$

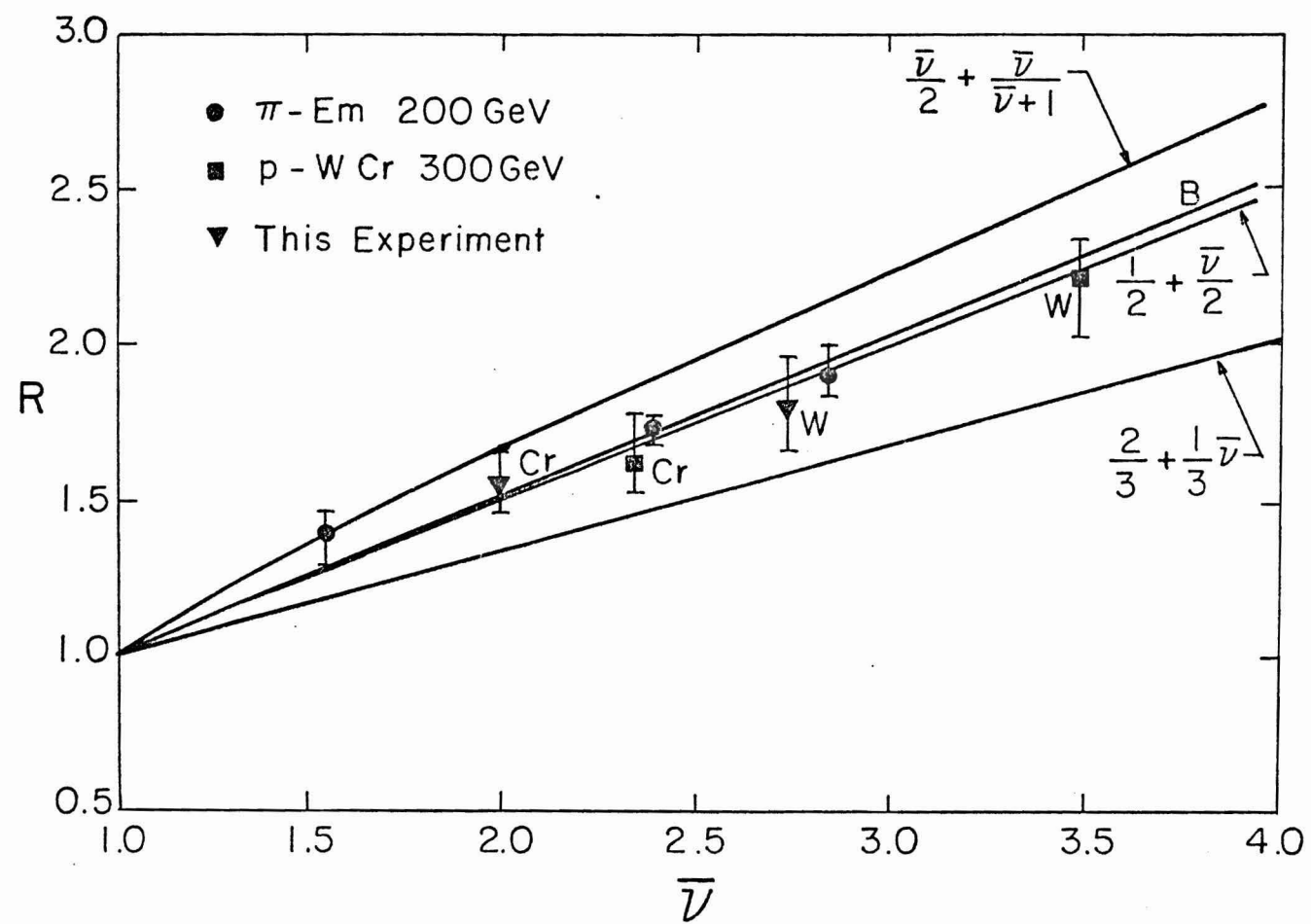
It is also found that R is a quantity not very sensitive to scanning bias. From Table III one can see that, for average multiplicities, the deviations of the corrected values from observed values are only 4% for both π -Cr and π -W events.

Figure 22 shows the data from this experiment and the data from proton-element and proton-emulsion (1) interactions at 300 GeV and 200 GeV respectively. Predictions of R vs. \bar{v} relations from different models (EFC, TPM, and the asymptotic form of R in the model proposed by S. J. Brodsky et al. with a new parton model approach) are also plotted. In addition, a best fit curve (B) for π -element and p-element interactions from counter experiments of W. Busza (2,15) are also shown in Figure 22 for comparison. It is clear that most of the data points seem to agree with the prediction of $R = \frac{1}{2} + \frac{1}{2} \bar{v}$ of either the modified EFC model or the TPM. Other than this, the data also agree with the MPM, since A. Capella and A. Krzywicki (16) found R consistent with W. Busza's data in MPM, while W. Busza's data also seems to support this observation within the limit of experimental error.

As to the energy dependence of R , it has been noticed that R is very weakly dependent on, or almost independent of, the incident energy E over the range 50~1,000 GeV.

FIGURE 22.

R vs. \bar{v} ; data are shown as indicated. The lines labeled with functions of \bar{v} are predictions from various models, while the line B is the best fit of data from the counter experiment (2).



Also, the relation between R and E depends on the type of projectile, as revealed by the data from p -Em and π -Em experiments (17). Both the data from reference (17) and this experiment seem not to agree well with either the prediction of the parton model of N. N. Nikolaev (which does not discuss the dependence on type of projectile), nor that of the EFC model (which predicts that R is a constant with E but dependent only on \bar{v}). However, it is premature to come to this conclusion at this stage; one needs data covering a wider energy range and different types of projectiles and targets before one can form any conclusions about this dependence.

4: Heavy Track Particles

The number of heavy tracks (N_h) emerging from the hadron-nucleus collision is believed to be a convenient measure of the degree of excitation or the effective size of the target nucleus in the interaction. The heavy track particles are mainly the recoil protons (which give grey tracks, the number of which is approximately linearly dependent on the number of black tracks) and target fragments (black tracks) evaporated from the excited nucleus via a thermal process. It has been found that the heavy tracks are isotropically emitted in the CM system and are independent of the incident energy. They

depend only on the target, and, probably, the type of projectile.

The histogram shown in Figure 23 is the N_h -distribution for π -W and π -Cr events (see caption), plotted separately, with bin width equal to 5. Similar to the findings for p-Em interactions at 200 GeV (18), both the π -W and π -Cr data decrease monotonically as N_h increases. However, there are differences when compared with the results from p-Cr and p-W interactions at 300 GeV (1), which show peaks at larger N_h values.

The average N_h values from this experiment are:

$$\langle N_h \rangle = 11.15 \pm 1.57, \text{ for } \pi\text{-W; and}$$

$$\langle N_h \rangle = 8.49 \pm .91, \text{ for } \pi\text{-Cr.}$$

These show little differences from interactions using protons as projectiles at 300 GeV (summarized in Table IV).

In Figure 24, data from both π -W and π -Cr interactions from this experiment are presented in terms of $\langle N_s \rangle$ vs. $\langle N_h \rangle$, with the line of least square fit for π -W events also plotted. Also presented are the data of π -Em interactions and their least square fit at 200 GeV from W. Wolter, Kraków Cosmic Ray Group (19). For comparison, the least square fit of p-Em data at 200 GeV (20) is also

FIGURE 23.

Histograms of N_h -distributions for (a) π -W and (b)
 π -Cr interactions at 200 GeV.

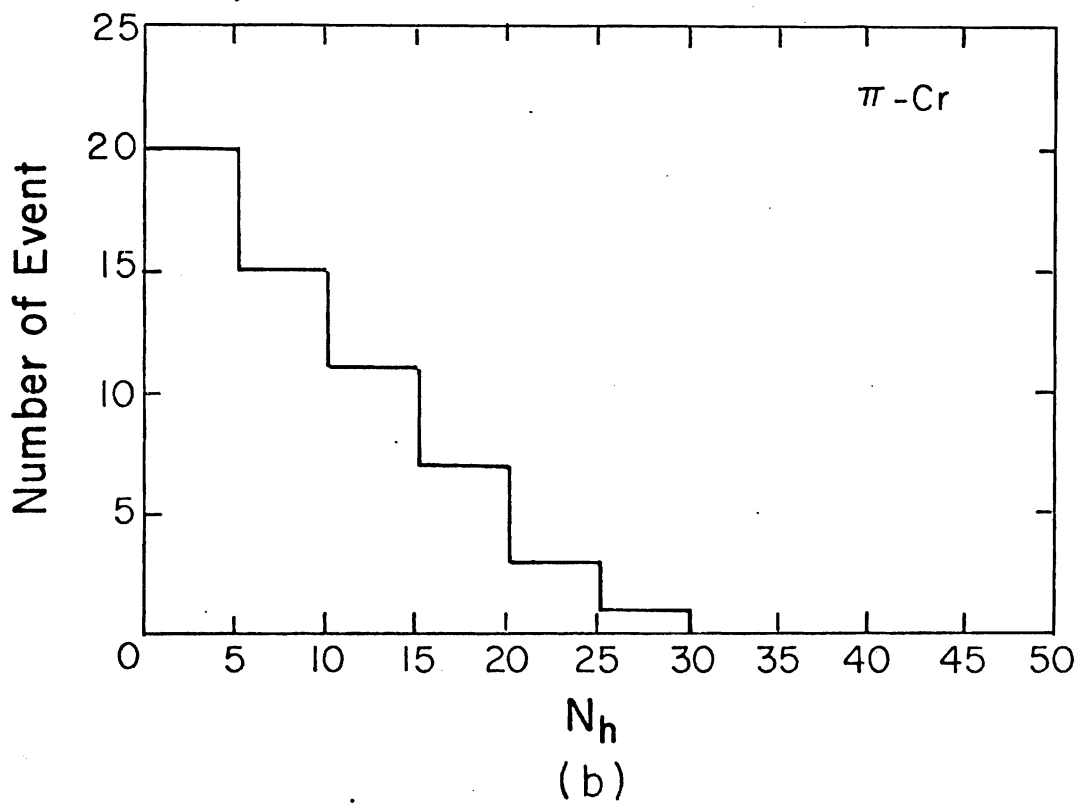
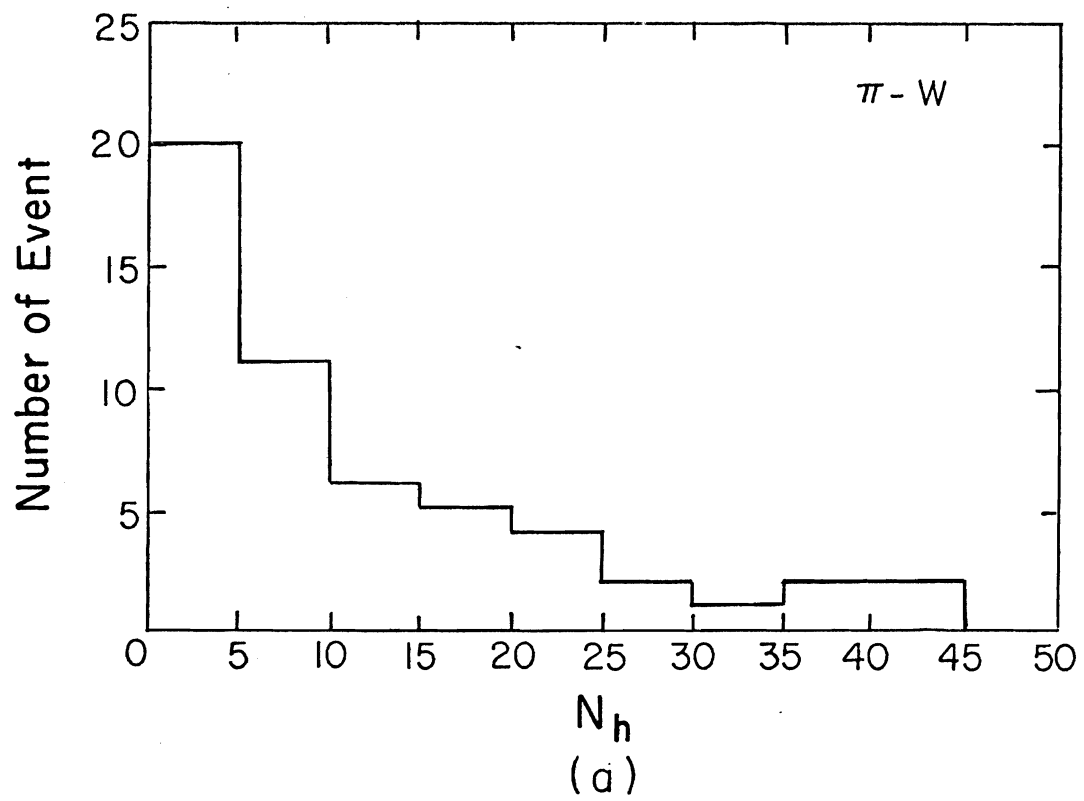


TABLE IV.

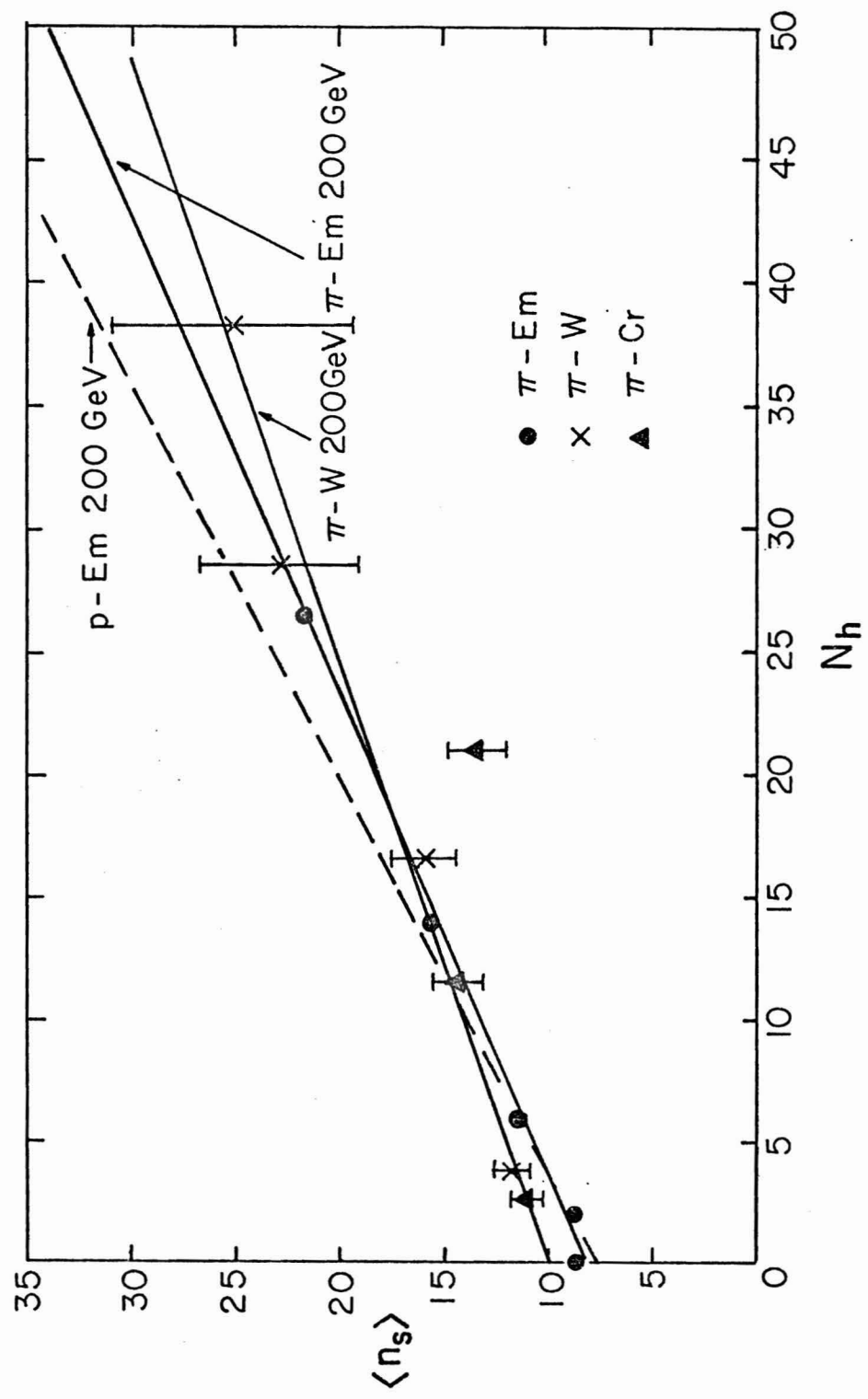
Comparison of $\langle N_h \rangle$ for hadron-nucleus interactions.

TABLE IV

Projectile	Target (A)	Number of events	$\langle N_h \rangle$	Incident energy	\bar{v}
P	W(184)	184	12.9 \pm 1.2	300 GeV	3.49
P	Cr(52)	52	7.2 \pm .07	300 GeV	2.36
π	W(184)	53	11.15 \pm 1.57	200 GeV	2.74
π	Cr(52)	57	8.49 \pm .91	200 GeV	2.00

FIGURE 24.

$\langle n_s \rangle$ vs. N_h data of π -W, π -Cr and π -Em (20) at 200 GeV are as indicated. The linear least square fits for π -Em, π -W and P-Em (19) interaction data are included for comparison.



plotted. It can be seen from the slopes that (i) at any specific energy, for nuclear emulsion as both target and detector and with different types of particles (say proton and pion) as projectile, the slope obtained from interactions using protons as projectiles is steeper than that from using pions; and (ii) for the same type of projectile, the nuclear emulsion, which provides a mixture of nuclei targets, gives a steeper slope than that obtained from a pure element target. This effect has also been observed (1) in comparing data from interactions of p-element with that from p-Em (Figure 25).

For the mixture of target nuclei presented in nuclear emulsion, the mean value of shower particles $\langle N_s \rangle$ increases linearly with N_h from 6.2 GeV to 300 GeV (18, 20), as shown in Figure 25, with the slope increasing with the energy. This linear dependence is also observed in both the experiment on p-element interactions (1), which is shown in Figure 25, and this experiment (in Figure 24) on π -element interactions.

Table V summarizes the coefficients of the straight lines

$$\langle n_s \rangle = a + b N_h$$

which fit the data of interactions using both π and p as

FIGURE 25.

A comparison of $\langle n_s \rangle$ vs. N_h for different projectiles and different targets at different energies, as indicated (19,1,3).

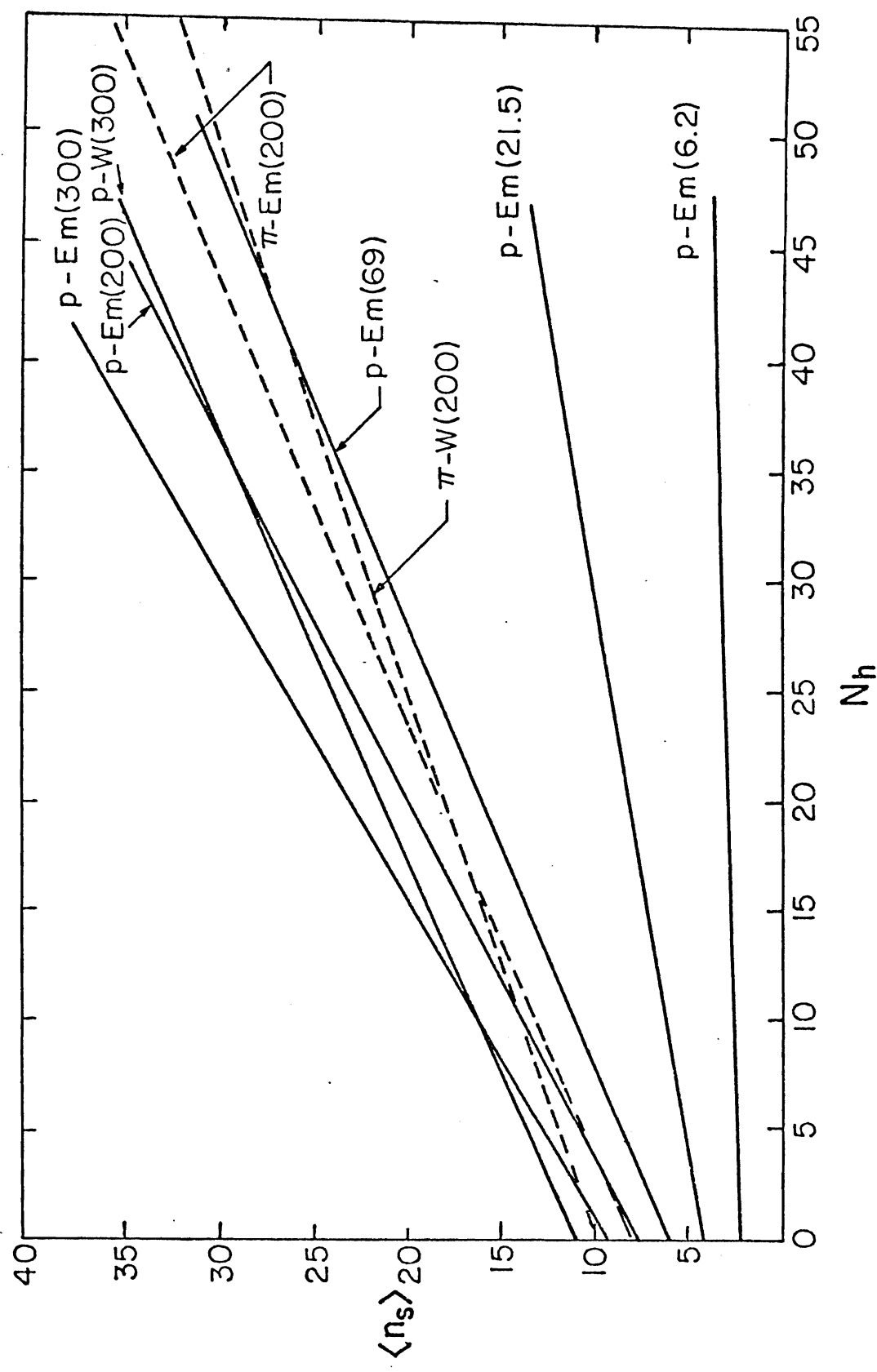


TABLE V.

Coefficients of linear least square fit of data
regarding

$$\langle n_s \rangle \text{ vs. } N_h: \langle n_s \rangle = a + bN_h$$

TABLE V

Interaction	E	a	b	χ^2/DF	From
π -Em		$8.24 \pm .28$	$.51 \pm .02$.02	W. Wolter, Kraków
π -W	200 GeV	9.98 ± 1.11	$.414 \pm .044$.04	This experiment
π -Cr		11.36 ± 1.92	$.13 \pm .14$.12	This experiment
P-Em		$9.2 \pm .5$	$.72 \pm .04$		Reference (1)
P-W	300 GeV	11.0 ± 2.4	$.57 \pm .15$.01	Reference (1)

projectiles, separately, at both 200 GeV and 300 GeV.

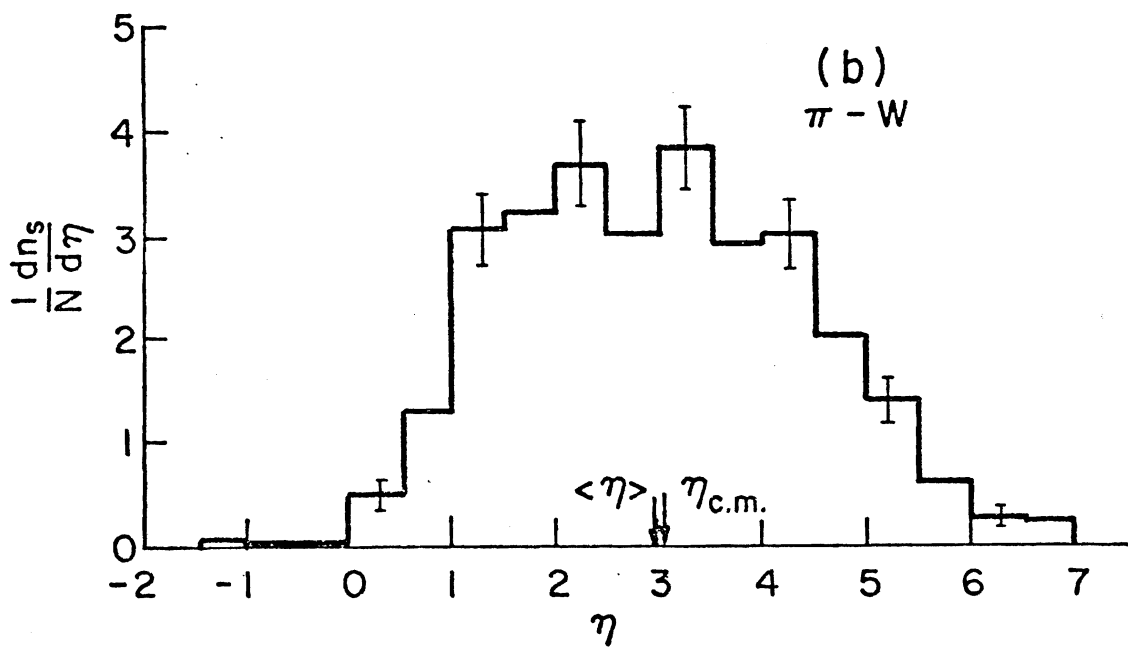
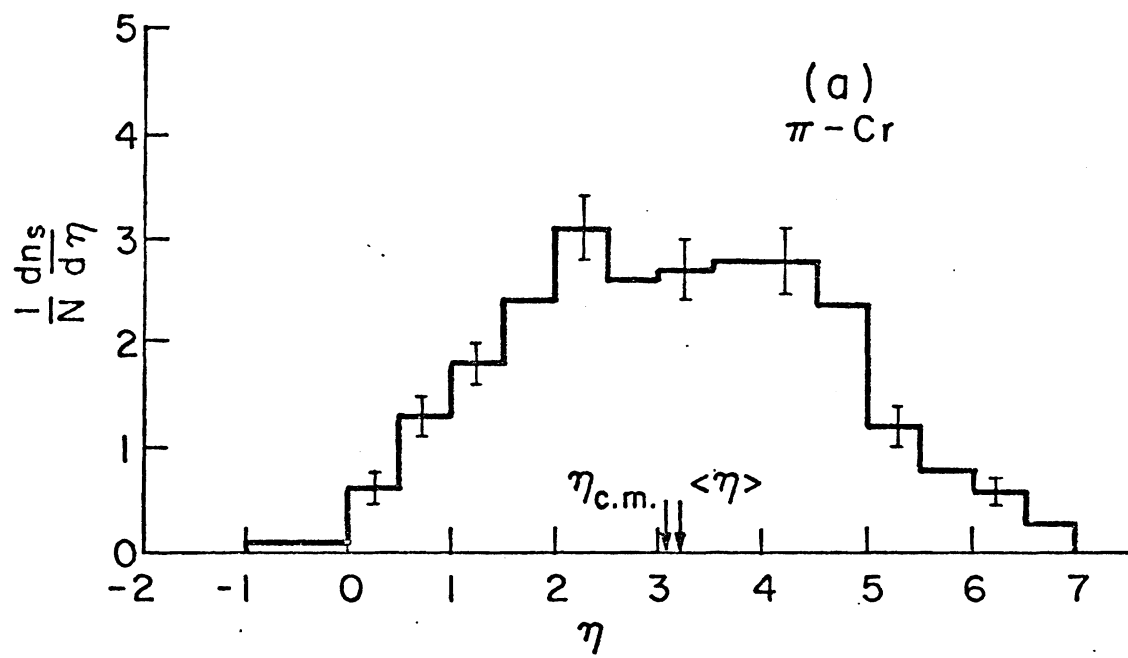
A very peculiar feature of π -Cr data seen in Figure 24 can also be observed in the p -Cr interaction at 300 GeV: (i) the data $\langle n_s \rangle$ from π -Cr interactions with smaller $\langle N_h \rangle$ falls onto the line that fits π -W data; and (ii) the data $\langle n_s \rangle$ with larger $\langle N_h \rangle$ falls far below the line. This deviation cannot be from scanning bias or any expected error, since it is impossible to miss events with large N_h values (around 20) in scanning. Intuitively, this deviation might be caused by some special saturated mechanism in the production process, which possibly due to the smallness of the chromium target ($A = 52$) becomes saturated at this energy range, while larger nuclei, like those of W ($A = 184$) might take more energy to produce the same effect.

(II) Angular Distribution.

Pseudo-rapidity distribution is used to express the angular distribution of high energy hadronic interactions. Figure 26 shows separate histograms of pseudo-rapidity (η) distribution for both π -W and π -Cr events, with bin width of 0.5. Each of the distributions has been normalized to correspond to a single interaction.

FIGURE 26.

Pseudo-rapidity distribution, normalized to that of one event, for (a) π -W and (b) π -Cr interactions at 200 GeV.



Error bars have been plotted for some bins to give an idea of the range over which distributions may fluctuate. A cut-off was made at $\eta = 7.0$, the high rapidity end, due to limitations of microscope sensitivity. Only for $\eta \lesssim 7.0$ can the Koristka microscope provide a high-accuracy measurement with error less than 2% on the average: beyond $\eta \gtrsim 7.0$, there are limitations on microscope sensitivity due to various kinds of scope noise, such as stage noise, grain noise, etc., which limit the measurement sensitivity of the microscope to 1 or 2 milliradians (mr). This corresponds to a pseudo-rapidity of $\eta = 6.91$ for $\theta = 2$ mr. Thus, measurements of pseudo-rapidity for particles with $\eta \gtrsim 7$ are not significant; these were therefore combined with the particles within the bin range of 6.5~7.0. In Figure 26, both the average pseudo-rapidities $\langle \eta \rangle$ and the CM rapidity η_{CM} for π -W and π -Cr interactions, also indicated with arrows, are found to be

$$\langle \eta \rangle = 2.954 \pm .053 \text{ for } \pi\text{-W};$$

$$\langle \eta \rangle = 3.131 \pm .057 \text{ for } \pi\text{-Cr};$$

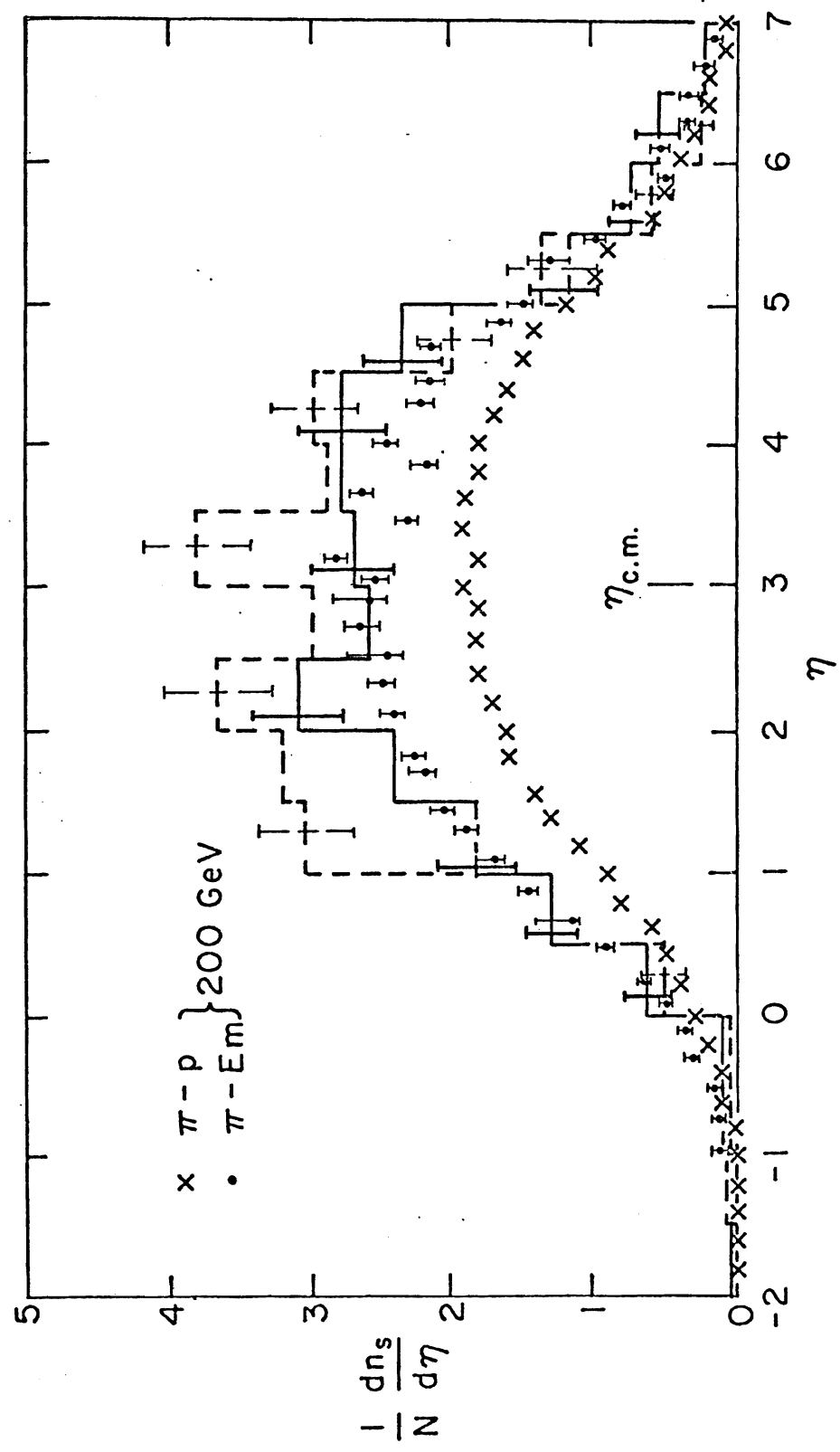
$$\eta_{CM} = \ln \frac{\sqrt{s}}{m_p} = 3.03, \text{ where } m_p = \text{mass of the nucleon.}$$

Figure 27 compares the η -distribution of hadronic interactions with the variation in target size (or target mass (A)). Shown in Figure 27 are the η -distributions from this experiment, along with those from π -Em interactions (21) and π -p interactions (22) with bubble chamber at 200 GeV. One can see that η -distributions seem to be independent of the size of the target in the projectile fragmentation region. Existence of the depletion predicted by MPM and N. N. Nikolaev is hard to judge in the last two units within the statistical accuracy allowed by this experiment. Increase in the target fragmentation region as A is increased is also seen. The critical value η_c is independent of A , and when $\eta \leq \eta_c$, the η -distribution of different target sizes starts to deviate from one another. This, predicted by EFC, is hard to see from the comparison graph.

In addition, the deviations from π -p of η -distribution do depend on A . These features contradict what is expected from the EFC models. Observations similar to those discussed above are also obtained from the experiment on π -Em interactions (23). In the target fragmentation region, the rapidity distribution rises with increasing A , but the expansion toward the direction of low

FIGURE 27.

Comparison of pseudo-rapidity distributions at 200 GeV with the variation of target sizes: π -p (22) and π -Em (21) data are as indicated; the solid histogram is for π -Cr interactions, and the dash histogram is for π -W interactions.



rapidity (predicted by CTM and also seen in the counter experiment (11,15) is not observed. Similar behavior is observed in the p-element experiment (1) and the π -Em experiment (21), which uses N_h as a means of distinguishing which atomic number was involved in a collision. The difference between the rapidity distribution of the backward particle ($\eta < 0$) in the counter experiment and the emulsion experiment is probably caused by the difference, with the counter experiment, in the backward-particle noise. Not having much background noise is known to be one of the advantages of using emulsion as a detector for hadronic interactions.

From the above observations on rapidity distribution, data would seem to agree more closely with the predictions of the MPM. Further, the growth of the height with A in the central region, which is $\sim 85\%$ for π -W and $\sim 45\%$ for π -Cr with respect to π -p data, is much faster than what is predicted by CTM. However, it is slower than what is predicted by either MPM or N. N. Nikolaev, in both of which $R_y \sim A^{\frac{1}{3}}$ in the central region. It is found in this experiment that the fit of $R_y \sim A^\alpha$ gives $\alpha \approx 0.2$ in the central region.

The η -distributions are also plotted for events grouped by different degrees of target excitation in terms of N_h for events with the same element target. Figures 28 and 29 are for π -W and π -Cr interactions respectively. As the target nucleus becomes more broken down, which is shown by the increase of N_h , η -distributions shift more to the small values. This implies that N_h is a relevant quantity for measuring the influence of the target nucleus on multiparticle production.

It should also be noticed that in both π -Cr and π -W interactions, bimodal structures, which are not seen at lower N_h , may exist in the η -distribution for $N_h \geq 11$. This has been pointed out by a Moscow group (23), whose data show the first maximum (right) located over $\eta = 3 \sim 4$ and the second maximum (left) developed with the increase of N_h and moved toward low rapidities. Since it is not seen in experiments using proton or other types of projectile, the bimodality is believed to be a property inherent in pion-nucleus interactions at high energies.

(III) Two-Particle Pseudo-Rapidity Correlations.

Two-particle pseudo-rapidity correlations have been extensively studied as a tool for understanding multi-

FIGURE 28

Pseudo-rapidity distributions for different ranges of N_h (a) $N_h = 0\sim 1$; (b) $N_h = 2\sim 10$; (c) $N_h \geq 11$ for π -W interactions at 200 GeV. Areas are normalized to the multiplicity for one event.

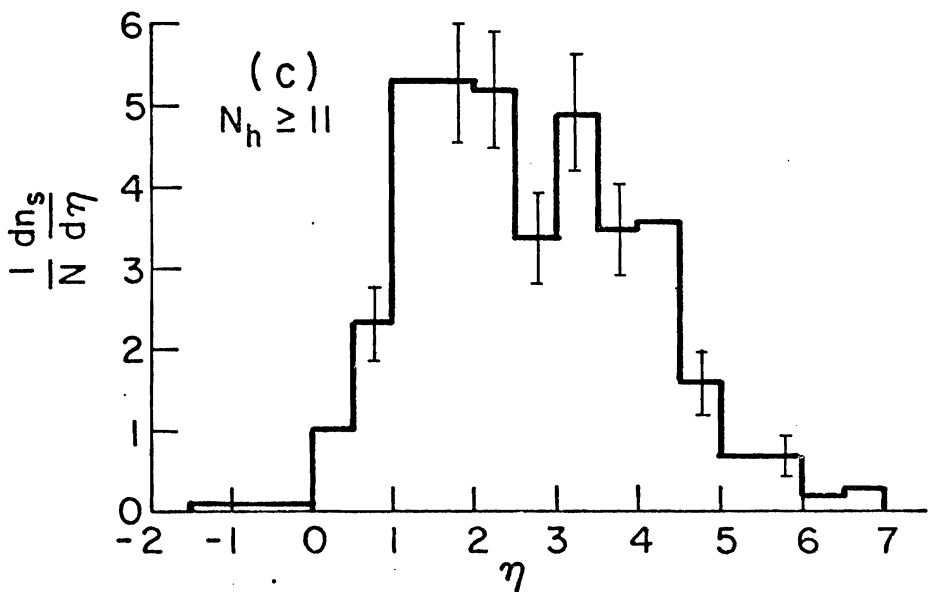
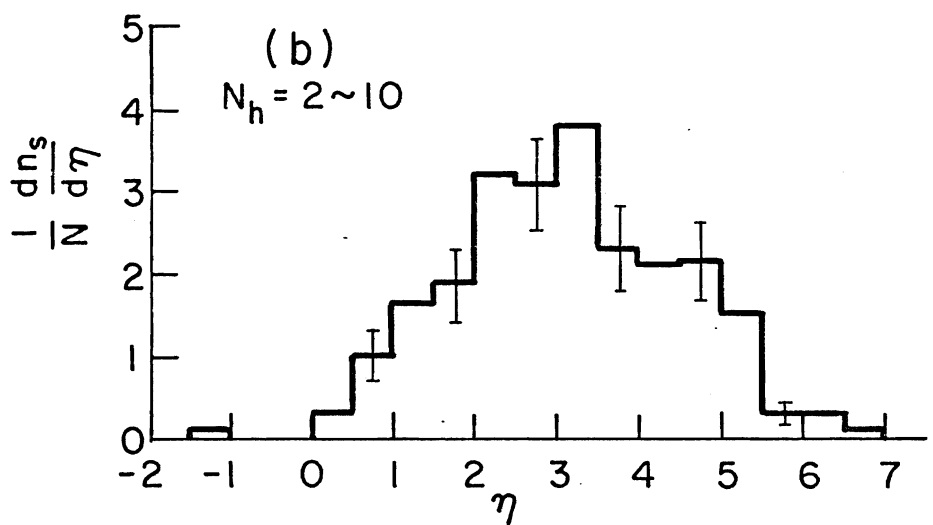
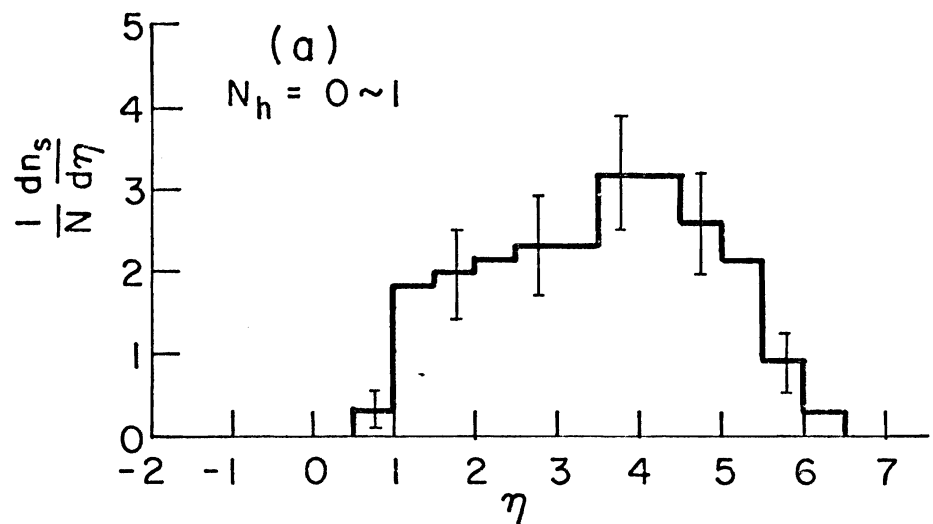
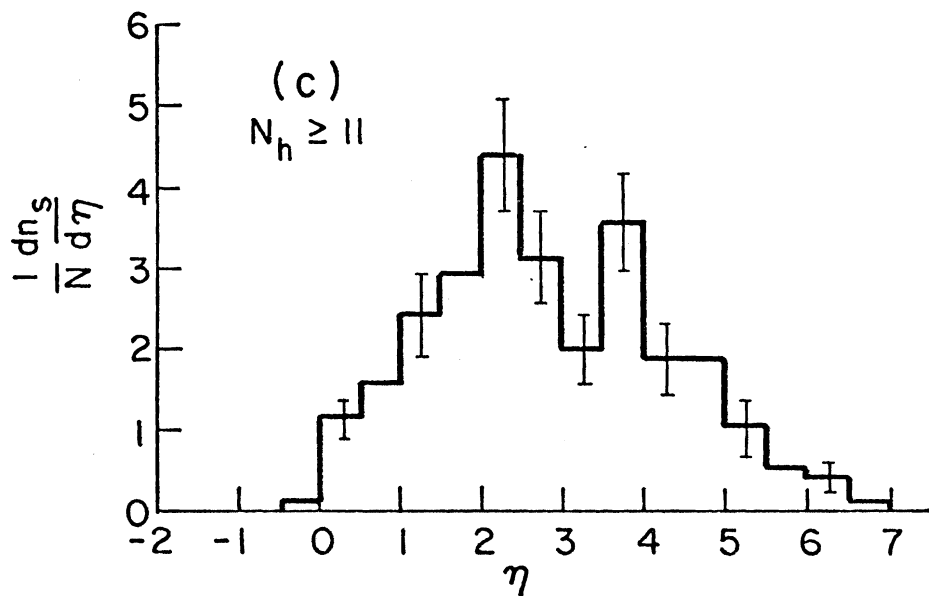
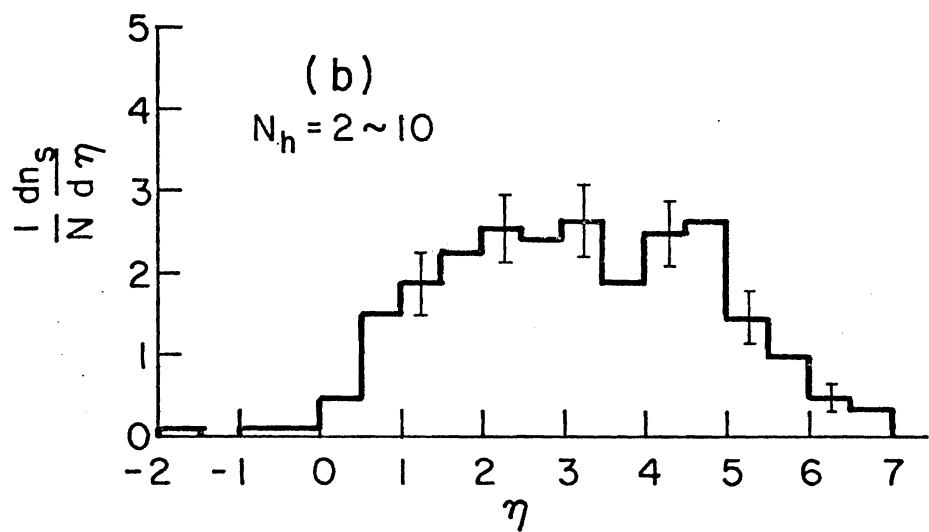
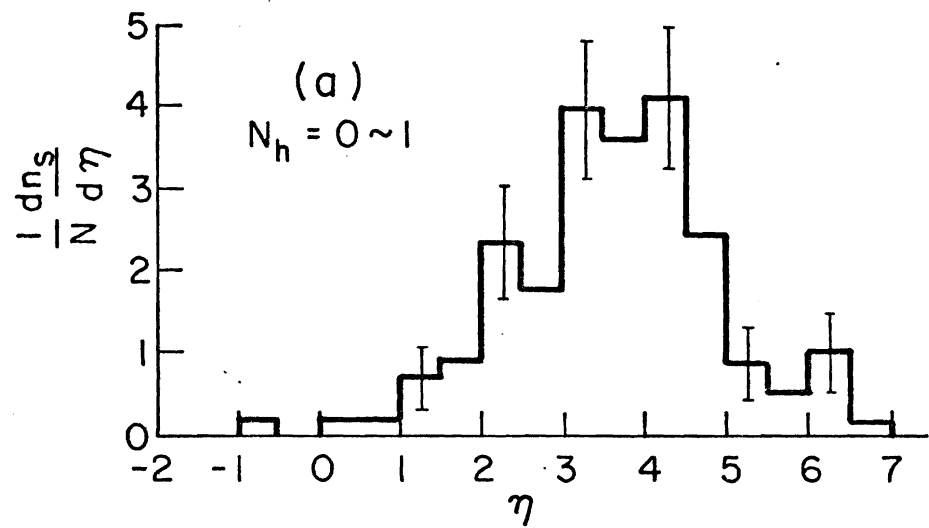


FIGURE 29.

Pseudo-rapidity distributions for different ranges of N_h (a) $N_h = 0 \sim 1$; (b) $N_h = 2 \sim 10$; (c) $N_h \geq 11$, for π -Cr interactions at 200 GeV. Areas are normalized to the multiplicity for one event.



particle production. Experiments in p-p interactions have been done at both FNAL and ISR (see Chapter II, section III). In addition, recent investigations have been made in this area using nuclear emulsion (i.e., with mixed nuclei) as the target (24,25). It was one of the main purposes of this experiment to provide data showing correlation behavior for hadronic interactions with pure element as the target. Figure 30 plots the values of function $R(\eta_1, \eta_2)$ at different fixed η_1 . These differ from those with proton targets. One can see that, (i) for η_1 fixed and close to zero ($\eta_1 = -.625$) when $\eta_2 < \eta_1$, function values of R (the normalized correlation function) are almost a constant, while when $\eta_2 > \eta_1$ they decrease; (ii) for η_1 fixed in the target region ($\eta_1 = -1.88$ for π -Cr and $\eta_1 = -3.13$ for π -W) monotonic decrease is seen.

Figures 31 and 32 show the general features of the two-particle correlation for π -W and π -Cr interactions respectively by the contour plot of the function $R(\eta_1, \eta_2)$ on the η_1, η_2 plane of the CM system. Only the area where we have statistical confidence in R is plotted. The graphs of the constant $R(\eta_1, \eta_2)$ are obtained by linear interpolation. Zero pseudo-rapidities in the lab system

FIGURE 30.

Correlation function $R(\eta_1, \eta_2)$ at several different fixed η_1 for π -W and π -Cr interactions at 200 GeV in the CM system.

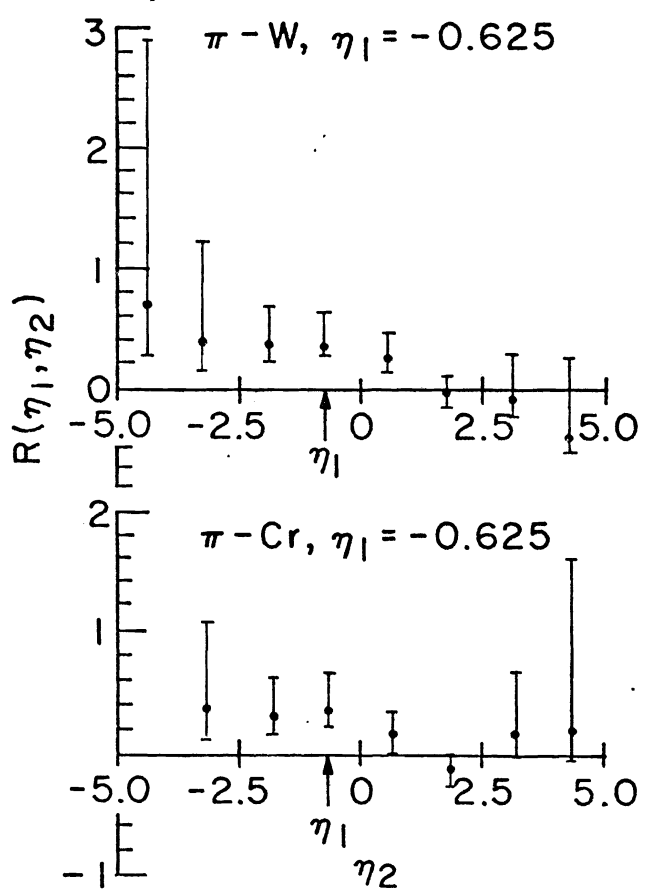
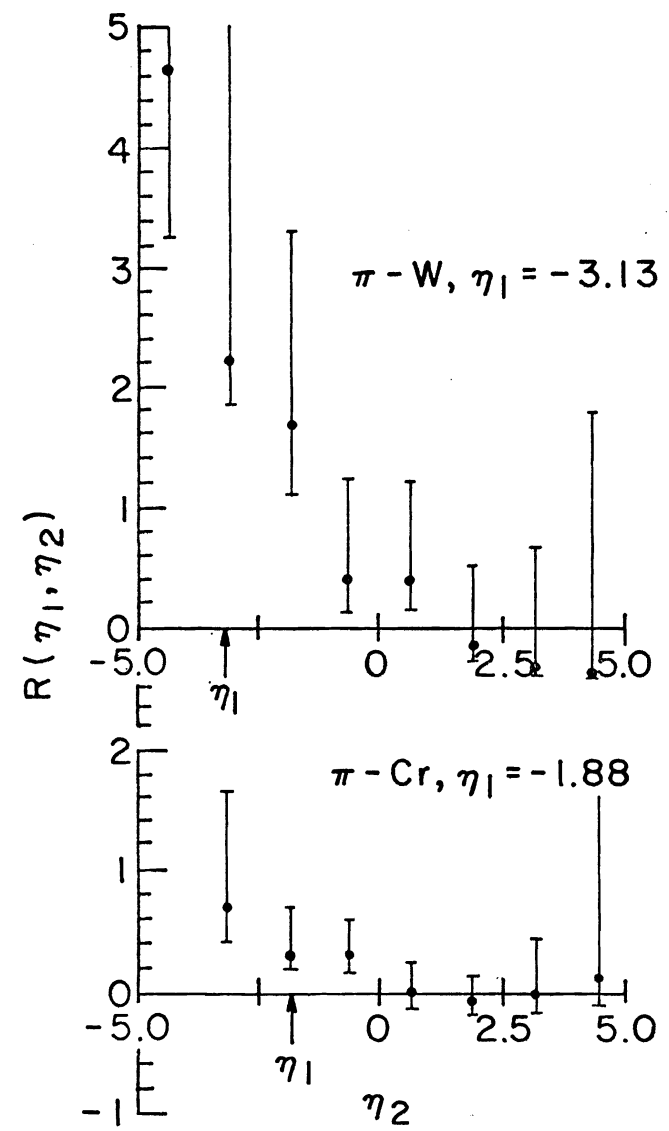


FIGURE 31.

Two-dimensional contour plot of the correlation function $R(\eta_1, \eta_2)$ for π -W interactions at 200 GeV in the CM system.

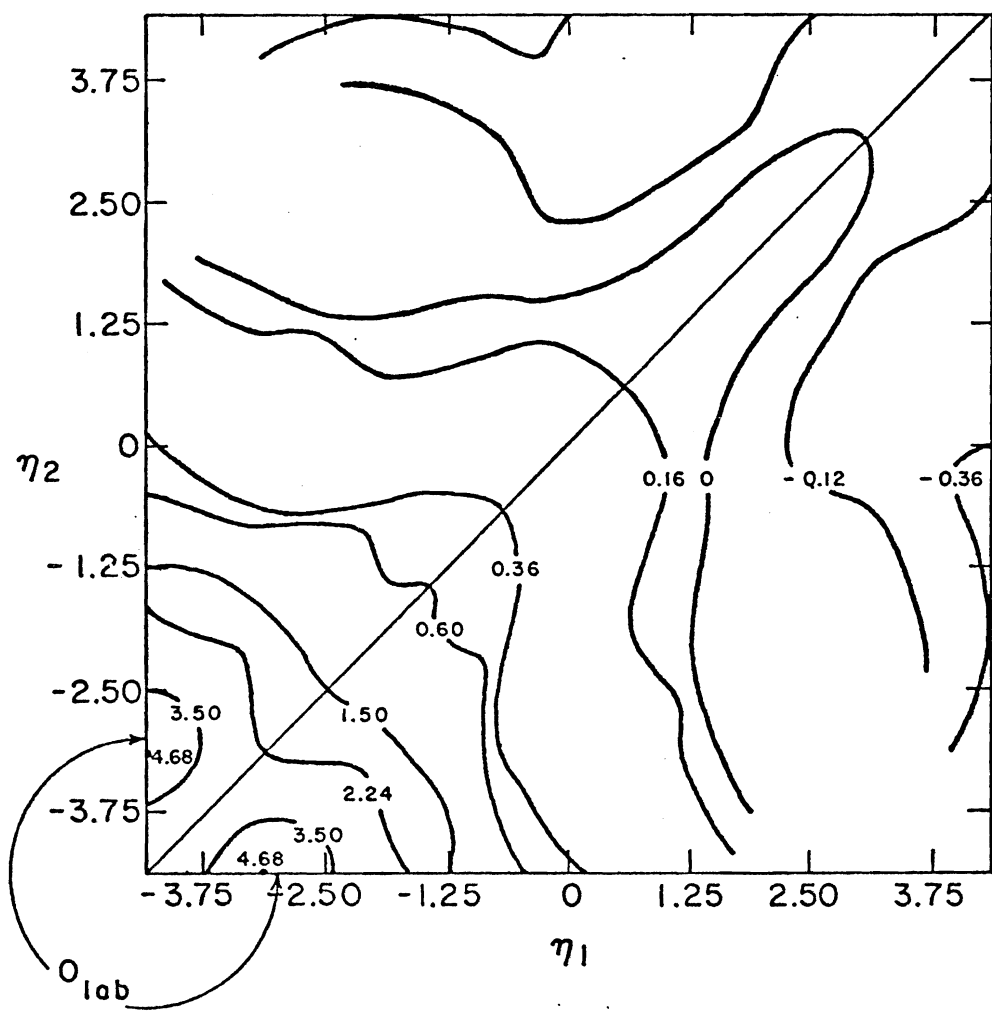
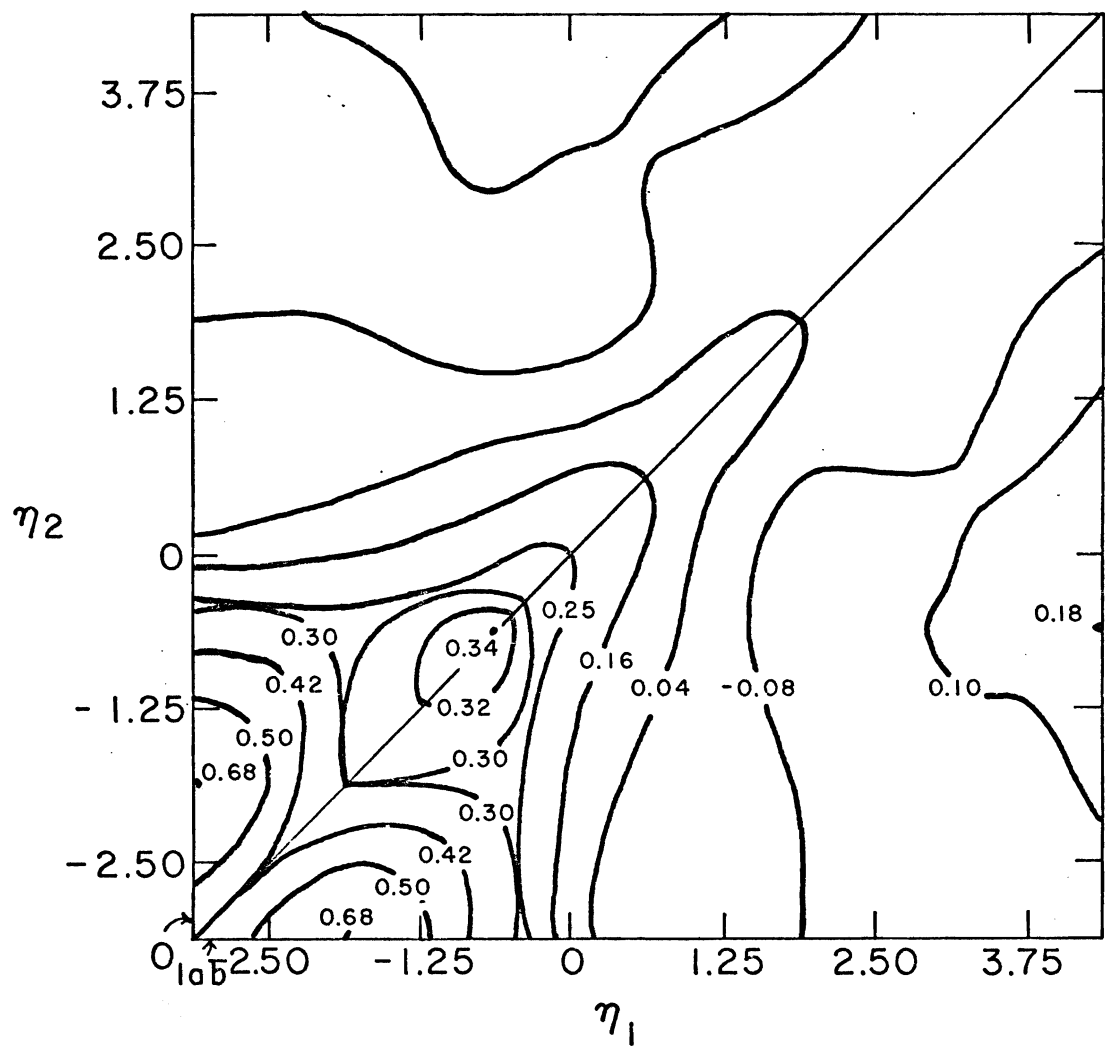


FIGURE 32.

Two-dimensional contour plot of the correlation function $R(\eta_1, \eta_2)$ for π -Cr interactions at 200 GeV in the CM system.



are indicated by arrows.

It is very obvious that the contour plot of R for π -nucleus interactions is very different from that derived from the use of protons as targets (see Figure 4). The plot is no longer symmetric to the line $\eta_1 = -\eta_2$, nor is the maximum at the center of the graph. (The remaining symmetry to the line $\eta_1 = \eta_2$ is due to the definition of the function R .) Instead, there are strong correlation centers at the low rapidity region, which resulted from the influence of the target nucleus. Also, in the CM system, there are very weak correlations (or none at all) between the forward cone and the backward cone particles--and particles in the very forward cone of the projectile region are uncorrelated. These facts imply that the mechanism involved in producing forward particles is different from that involved in producing backward particles, which are believed to be produced in a much more complicated multi-step process in which the production of a backward particle in the target fragmentation region tends to induce the production of another particle in the same region.

The fact that $R(\eta_1, \eta_2)$ are very different in $h-h$ and $h-A$ interactions implies the contradiction of data to the

CTM prediction, while the interaction mechanism described by N. N. Nikolaev might be a better candidate to account for this difference in R.

(IV) Conclusion.

There are three major areas of conclusions stemming from this experiment. The first concerns multiplicity distribution; the second the angular distribution; and the third, the two-particle pseudo-rapidity correlation.

The multiplicity distribution for π -nucleus interactions is scaled in the same manner as that described by Slattery's function for p-p interactions, with the dispersion increasing linearly with the average multiplicity $\langle n_s \rangle$, which itself increases linearly with the number of heavy tracks N_h , except for the unusual data point of π -Cr interaction at large N_h . Finally, the multiplicity ratio R depends on \bar{v} , the average number of collisions in the target nucleus, in a relationship $R = \frac{1}{2} + \frac{1}{2} \bar{v}$. This is consistent with most of the current models. To see if this feature agrees with the MPM or the parton model of N. N. Nikolaev, one would need to check if the asymptotic value of R approaches some certain value.

The pseudo-rapidity distributions of π -nucleus interactions are almost independent of target mass A in the forward cone, while in the target fragmentation region the η -distribution rises as A increases. This feature seems contradictory to the EFC model but close to the MPM. If one groups the shower particles by the degree of target excitation using different ranges of N_h , one can see that the η -distribution shifts in the direction of low rapidity as N_h increases, while at large N_h there is some possibility that the η -distribution develops a second maximum and shows a bimodal structure.

A strong but almost constant correlation is found for particles with rapidities in the target fragmentation regions. Particles in the forward cone are very weakly (or not at all) correlated with those in the backward cone. No correlation is found among particles in the projectile fragmentation region.

One of the main difficulties in explaining and organizing this data is the lack of understanding of the hadron-nucleus interaction mechanism. There is no theoretical model-independent way of extracting information about the space-time evolution of the interaction from the experimental data--only the general feature, that

secondary particles are not produced instantaneously at the moment of collision, seems to be well established. It takes a characteristic time τ of interaction in the lab frame of reference to develop the asymptotic final state for the multiparticle production.

In future work, one would expect that:

(i) theoretically: more detailed calculations of predictions of various possible multiparticle production mechanisms should be done for comparison with the existing data; moreover, it is important to develop the theory and carry out predictions on the subject of two-particle correlation to account for the behavior of $R(\eta_1, \eta_2)$ from h-A interactions;

(ii) experimentally: more hadron-nucleus experiments with a wider energy range or different type of projectile and target nucleus with better precision should be carried out for establishing how quantities like average multiplicity $\langle n_s \rangle$, or multiplicity ratio R , are dependent on incident energy, projectile, and target nucleus.

CHAPTER V:

REFERENCES

1. J. R. Florian et al. Phys. Rev. D13 #3, 558 (1976).
2. W. Busza. AIP Conference Proceedings No. 26 (1975).
3. I. Otterlund. Cosmic Ray Physics Report LUIP-CR-76-07 (1976).
4. P. L. Jain et al. Phys. Rev. Lett. 34 #15, 972 (1975).
5. D. Bogert et al. Phys. Rev. Lett. 31, 1271 (1973).
6. A. J. Buras et al. Phys. Lett. 47B, 251 (1973).
7. J. R. Elliott et al. Phys. Rev. Lett. 34, 607 (1975).
8. A. Wróblewski. Acta Physica Polonica B4, 857 (1973).
9. W. Thomé et al. Preprint submitted to Nucl. Phys. (June, 1977).
10. J. Babecki et al. Phys. Lett. 47B #3, 268 (1973).
11. G. W. Busza. Phys. Rev. Lett. 34, 839 (1975).
12. E. L. Berger et al. Nucl. Phys. B77, 365 (1974).
13. D. Fong et al. Phys. Lett. 53B, 290 (1974).
14. S. P. Denisov et al. Nucl. Phys. B61, 62 (1973).
15. W. Busza, Paper submitted to the XVIII Int. Conf. on High Energy Physics and Preprint of lectures given at the VII Int. Colloquium on Multiparticle Reactions, Tutzing, June 21-25 (1976).

16. A. Capella and A. Krzywicki. Preprint LPTPE-77/16.
17. R. Holynski, S. Krzywdzinski and K. Zalewski. Acta Physica Polonica B5, 321 (1974).
18. J. R. Florian. University of Washington Doctoral Dissertation, unpublished (1974).
19. L. Voyvodic. Data from W. Wolter; private communication.
20. E. M. Friedlander, M. Marcu and R. Nitu. Lettere al Nuovo Cimento (1973).
21. B. Furmanska et al. Preprint, Kraków (August, 1977).
22. N. N. Biswas. Private communication (University of Notre Dame, Notre Dame, Indiana).
23. Alma-Ata-Ga'china-Moscow-Tashkent Collaboration. Preprint (1977).
24. G. Baroni et al. Nucl. Phys. B103, 213 (1976).
25. B. Wosiek. Preprint, Report No. 930/PH, Kraków (September 1976).

BIBLIOGRAPHY

1. Adair, R. K. Phys. Rev. 172, 1370 (1968).
2. Afek, Y., et al. Preprint Technion-PH-48 (1976).
3. Albini, E. Nuovo Cimento 32A, 101 (1976).
4. Albrow, M. G. et al. Phys. Lett. 51B, 421 (1974).
5. Allaby, J. V. et al. 17th Int. Conf. on High Energy Phys., London (1974).
6. Alma-Ata-Budapest-Kraków-Dubna-Sofia-Tashkent-Ulan Bator Collaboration, Proc. 11th Int. Conf. on Cosmic Rays, Budapest (1969).
7. Alma-Ata-Moscow-Tashkent Collaboration, Preprint N77, Moscow (1977).
8. Amati, D. Nuovo Cimento 26, 896 (1962).
9. Amendolia, S. R., et al. PSB Collaboration, Phys. Lett. 48B #4, 359 (1974).
10. Babecki, J. et al. Phys. Lett. 47B #3, 268 (1973).
11. Babecki, J. et al. Phys. Lett. 52B #2, 247 (1974).
12. Barband, A. Phys. Rev. D3, 2227 (1971).
13. Barkas, Walter H. Nuclear Research Emulsion, Academic Press (1963).
14. Baroni, G. et al. Nucl. Phys. B103, 213 (1976).
15. Benecke, J. et al. Phys. Rev. 188 #5, 2159 (1969).

16. Berger, E. L. and A. Krzywicki. Phys. Lett. 36B, 380 (1971).
17. Berger, E. L. Phys. Lett. 43B #2, 132 (1973).
18. Berger, E. L. et al. Nucl. Phys. B77, 365 (1974).
19. Berlad, G., A. Dar and G. Eilam. Phys. Rev. D13 #1, 161 (1976).
20. Bertocchi, L. AIP Conf. Proc. #26 (1975).
21. Bialkowski, G., C. B. Chiu and D. M. Tow. Phys. Lett. 68B #5, 451 (1977).
22. Bialas, A. et al. Nucl. Phys. B48, 237 (1972).
23. Biswas, N. N. et al. Phys. Rev. Lett. 35 #16, 1059 (1975).
24. Biswas, N. N. Private communication.
25. Bogert, D. et al. Phys. Rev. Lett. 31, 1271 (1973).
26. Brodsky, S. J., J. F. Gunion and J. H. Kühn. Phys. Rev. Lett. 39 #18, 1120 (1977).
27. Buras, A. J. et al. Phys. Lett. 47B, 251 (1973).
28. Busza, W. Phys. Rev. Lett. 34, 839 (1975).
29. Busza, W. AIP Conf. Proc. #26 (1975).
30. Busza, W. Paper submitted to the XVIII Int. Conf. on High Energy Physics and preprint of lectures given at the VII Int. Colloquium on Multiparticle Reactions, Tutzing (June 21-25, 1976).

31. Butt, J. E. and D. T. King. AIP Conf. Proc. #12,
Particle and Field Subseries #4.
32. Calucci, G., R. Jengo and A. Pignotti. Phys. Rev.
D10, 1468 (1974).
33. Capella, A. and A. Krzywicki. Preprint LPTPE-77/16.
34. Capiluppi, P. et al. Nucl. Phys. B79, 189 (1974).
35. Chaney, D. et al. Phys. Rev. Lett. 40 #2, 71
(1978).
36. Chew, G. F. and A. Pignotti. Phys. Rev. Lett.
20, 1078 (1968).
37. Chew, G. F. and A. Pignotti. Phys. Rev. 176,
2112 (1968).
38. Chou, T. T. and C. N. Yang. Phys. Rev. Lett. 25
#15, 1072 (1970).
39. Cocconi, G. Phys. Rev. 111, 1969 (1958).
40. Cornell-FNAL-Kraków-MSU-Seattle Collaboration.
Deep-Inelastic Interactions of Tagged 150 GeV
Muon in Nuclear Emulsion Targets. E.382, pri-
vate communication.
41. Castagnoli, C. et al. Nuovo Cimento 10, 1539
(1953).
42. Czyzewski, D. and Rybicki. Nucl. Phys. B47, 633
(1972).

43. Dar, A. and Tran Thanh Van. Preprint Technion Ph-76-61.
44. Dar, A. and J. Vary, Phys. Rev. D6 #9, 2412 (1972).
45. Denisov, S. P. et al. Nucl. Phys. B61, 62 (1973).
46. De Wolf, E. et al. Nucl. Phys. B87, 325 (1975).
47. Dibon, H. et al. Phys. Lett. 44B, 313 (1973).
48. Drell, S. D. and T. M. Yan. Phys. Rev. Lett. 25, 316 (1970).
49. Eggert, E. et al. Nucl. Phys. B86, 201 (1975).
50. Elliott, J. R. et al. Phys. Rev. Lett. 34, 607 (1975).
51. Feinberg, E. L. Phys. Report 5C #5 (1972).
52. Ferbel, T. Recent Results from HBC at FNAL COO-3065-91 (1974).
53. Feynman, R. P. Phys. Rev. Lett. 23 #24, 1415 (1969).
54. Fialkowski, K. Phys. Lett. 41B, 379 (1972).
55. Fialkowski, K. Phys. Lett. 43B, 61 (1973).
56. Fishbane, P. M. and I. S. Trefil. Phys. Lett. 51B #2 (1974); Phys. Rev. Lett. 31 #11, 734 (1973); Nucl. Phys. B58, 261 (1973); Phys. Rev. D9 #1, 168 (1974).
57. Florian, J. R. University of Washington Dissertation, unpublished (1974).
58. Florian, J. R. et al. Phys. Rev. D13 #3, 558 (1976).

59. Fong, D. et al. Phys. Lett. 53B, 290 (1974).
60. Frazer, W. R. Rev. of Mod. Phys. #2, 284 (1972).
61. Frazer, W. R. et al. 13th International Cosmic Ray Conference, Denver, Colorado, 17-30 August (1973).
62. Friedlander, E. M., M. Marcu and R. Nitu. Lettere al Nuovo Cimento (1973).
63. Furmanska, B. et al. Preprint, Kraków (August 1977).
64. Gierula, J. and W. Wolter. Acta Physica Polonia B2, 95 (1971).
65. Goldhaber, A. S. Phys. Rev. D7, 765 (1973).
66. Good, M. L. and W. D. Walker. Phys. Rev. 120, 1857 (1960).
67. Gottfried, K. Phys. Rev. Lett. 32 #17, 957 (1974).
68. Gottfried, K. Ref TH 1735-CERN, CERN Preprint.
69. Hayakawa, S. Cosmic Ray Physics; Monographs and Texts in Physics and Astronomy vol XXII, Wiley-Interscience (1969).
70. Holynski, R., S. Krzywdzinski and K. Zalewski. Acta Physica Polonia B5, 321 (1974).
71. Jain, P. L. et al. Phys. Rev. Lett. 34 #15, 972 (1975).

72. Koba, Z., H. B. Nielsen and P. Olesen. Nucl. Phys. B40, 317 (1972).
73. Konishi, S., et al. Phys. Rev. D13 #7, 1826 (1976).
74. Koplik, J. and A. H. Mueller. Phys. Rev. D12 #11, 3638 (1975).
75. Landshoff, P. V. and J. Polkinghorn. Nucl. Phys. B32, 541 (1971).
76. Marton, L., Editor in Chief. Method of Experimental Physics, Nuclear Physics, 5A; Academic Press (1961).
77. Marton, L., Editor in Chief. Method of Experimental Physics, Nuclear Physics, 5B; Academic Press (1961).
78. Mueller, A. H. Phys. Rev. D2, 2963 (1970).
79. Mueller, A. H. Phys. Rev. D4, 150 (1971).
80. Nikolaev, N. N. Review paper given in International Seminar on particle-nucleus interaction, Miramere-Trieste, 10-15 June 1976.
81. Otterlund, I. Cosmic Ray Physics Report LUIP-CR-76-07 (1976).
82. Pirilä, P. Phys. Lett. 43B, 502 (1973).
83. Powell, Fowler and Perkins. The Study of Elementary Particles by the Photographic Method. Pergamon Press (1959).

84. Quigg, C. AIP Conference Proceedings #12 (1973).
85. Ranft, G. and J. Ranft. Phys. Lett. 45B #1, 43 (1973).
86. Rossi, Bruno. High Energy Particles; Prentice Hall, Inc. (1952).
87. Slattery, P. Phys. Rev. D7 #7, 2073 (1973).
88. Slattery, P. Phys. Rev. Lett. 29 #24, 1624 (1972).
89. Thomé, W. et al. Preprint, submitted to Nucl. Phys. (June 1977).
90. Voyvodic, L. Private communication: data, from W. Wolter.
91. Waddington, C. J. Supp. Nuovo Cimento 19, 37 (1961).
92. Weis, J. H. Acta Physica Polonica B7, 851 (1976).
93. Whitmore, J. AIP Conference Proceedings #12 (1973); Preprint NAL-Pub-73/70-EXP (1973).
94. Wilson, K. G. Cornell preprint CLNS-31 (1970).
95. Wosiek, B. Preprint, Report No. 930/PH, Kraków (September 1976).
96. Wróblewski, A. Acta Physica Polonica B4, 857 (1973).
97. Yodh, G. B. et al. Phys. Rev. Lett. 28 #15, 1005 (1972).

APPENDIX I:
MEASUREMENT OF THE TRACKS

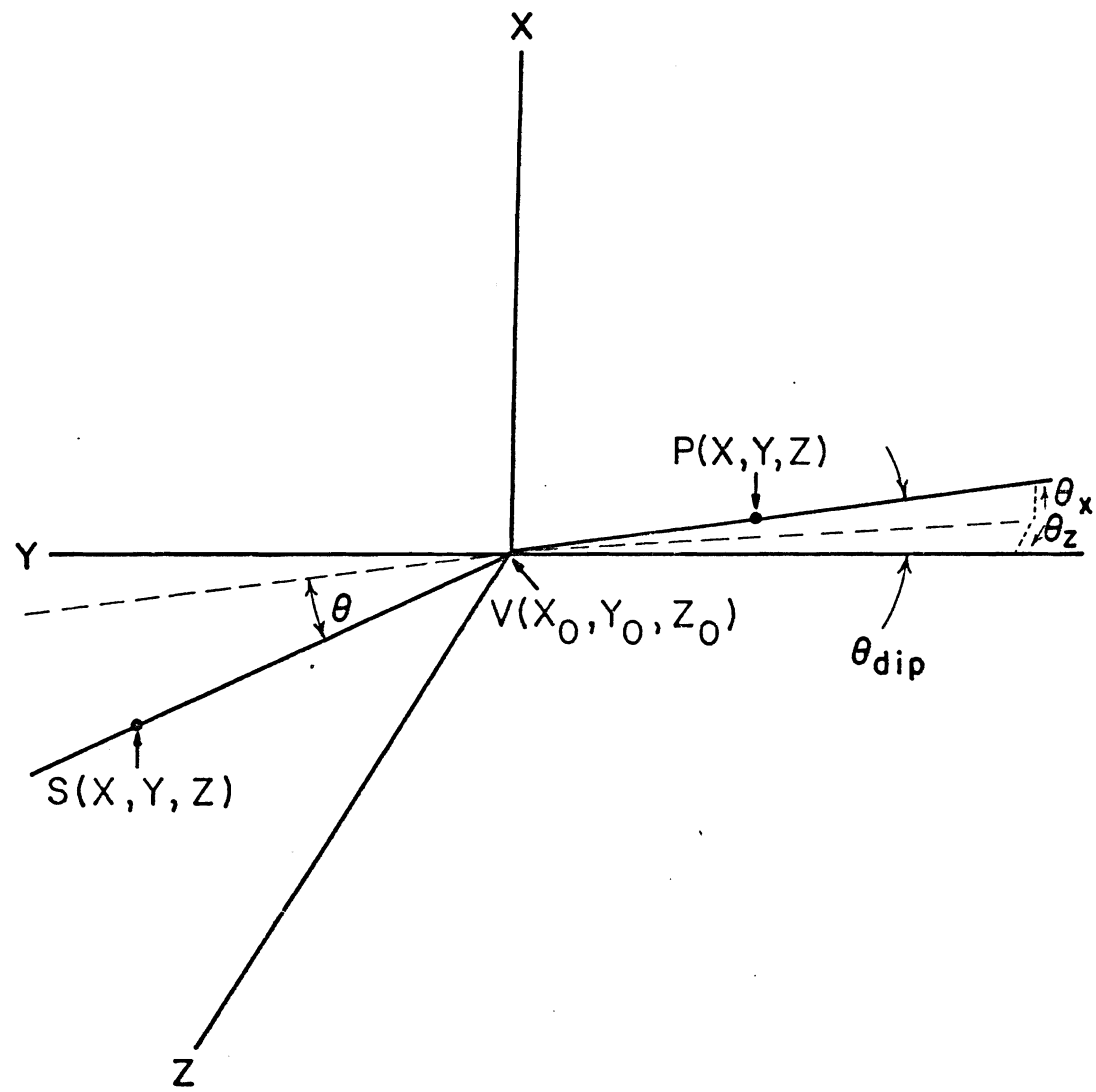
(A) Regular Measurement

This method is used when the tracks and emulsions are not seriously curved. Thus the minimum ionized track can be almost aligned along the scope coordinate. It is easier to measure an event when the primary is aligned to the scope coordinate and the vertex is located by the center of all the heavy tracks.

Take, for example, the measurement of the primary and a given track as shown in Figure 1. The x-y plane is that seen in the scope, and z is the vertical axis of the microscope. V is the vertex. To get the dip angle θ_{dip} , which is defined as the angle deflected from the horizontal plane, and the deflection angle θ of the slower track \overline{VS} from the primary track \overline{PV} , one needs to measure the coordinates of points S (x, y, z), V(x_0, y_0, z_0) and P(x, y, z). S and P are arbitrarily chosen from the shower track and the primary track respectively. For the sake of accuracy, it is preferred to choose point P three or four mm away from the vertex V, and S not too close to V.

FIGURE 1.

The spatial measurement of the primary and a given track.



Since the dip angle is small ($\leq 1.5^\circ$ for all the events found) it is legitimate to calculate it by calculating its x and z components. Thus

$$\theta_{\text{dip}} = [\theta_x^2 + \theta_z^2]^{\frac{1}{2}}$$

$$= \left[\left(\tan^{-1} \frac{(S.F.) (P_z - z_0)}{P_y - y_0} \right)^2 + \left(\tan^{-1} \frac{c(P_x - x_0)}{P_y - y_0} \right)^2 \right]^{\frac{1}{2}}$$

where S. F. is a shrinkage factor, differing with the type of emulsion;
 and c is a constant associated with the x-measurement; $c = .073$ in this experiment.

The deflection angle θ can also be derived by the cosine rule; thus, $\cos \theta =$

$$\frac{.073^2 (P_x - x_0) (S_x - x_0) + (P_y - y_0) (S_y - y_0) + (S.F.)^2 (P_z - z_0) (S_z - z_0)}{a^{\frac{1}{2}} b^{\frac{1}{2}}}$$

where $a = .073^2 (P_x - x_0)^2 + (P_y - y_0)^2 + (S.F.)^2 (P_z - z_0)^2$
 and $b = .073^2 (S_x - x_0)^2 + (S_y - y_0)^2 + (S.F.)^2 (S_z - z_0)^2$

(B) Double Measurement

When the tracks, due to the curvature of the emulsion, are very curved, it is improper to measure them by the aforementioned method. In order to reduce measurement error, a minimum ionized track which is parallel to and quite close to the primary track is chosen to serve as a reference coordinate.

Let L be the reference track by the event shown in Figure 2(a). In order to transform the tracks of the event to the reference coordinate from the microscope coordinate, it is necessary to take the coordinates of six points, P, v, S , and their corresponding points P', v', S' on L with the same y value.

Except for the vertex, a point with coordinates (x, y, z) is transformed to the new coordinates $(\Delta x, y, \Delta z)$ with

$$\Delta x = (x - x') - (x_0 - x'_0)$$

$$y = y$$

$$\Delta z = (z - z') - (z_0 - z'_0),$$

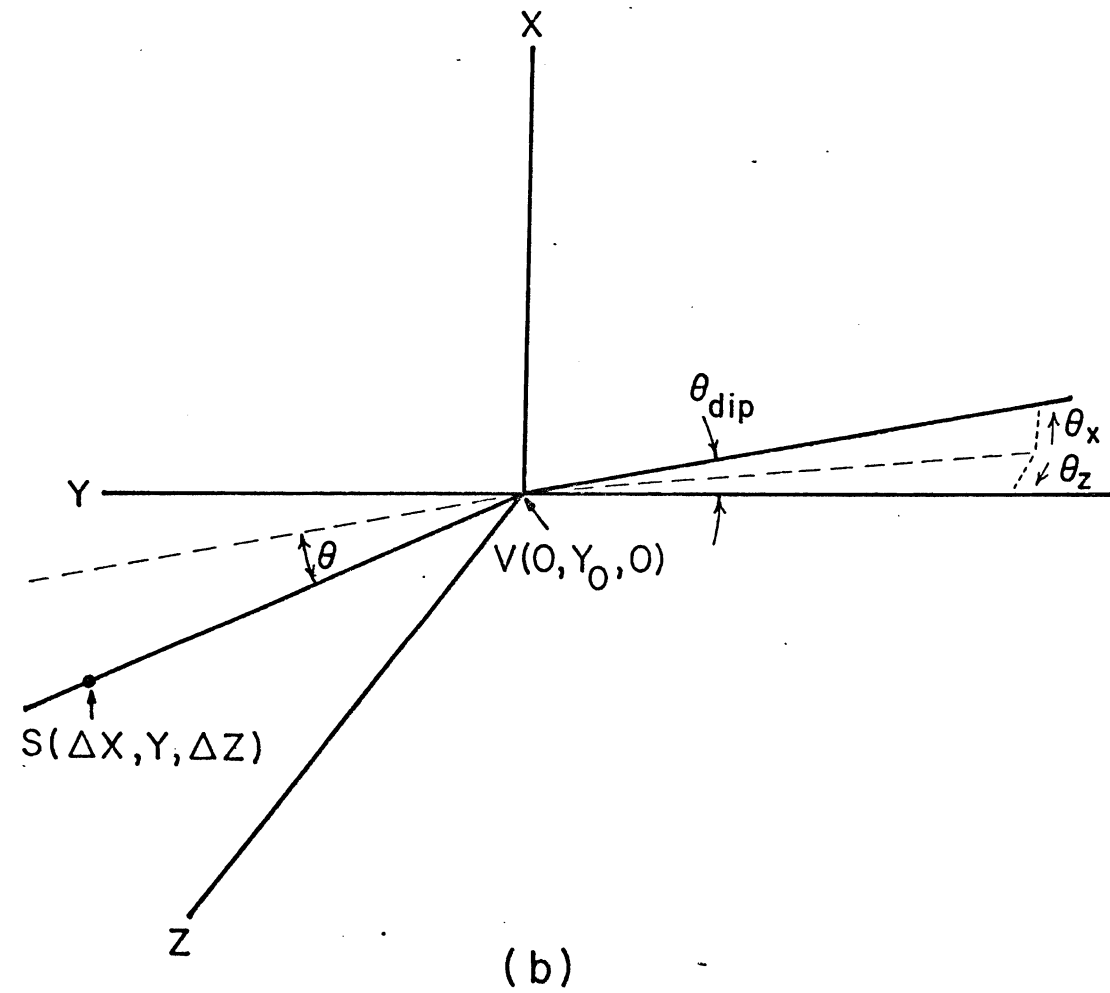
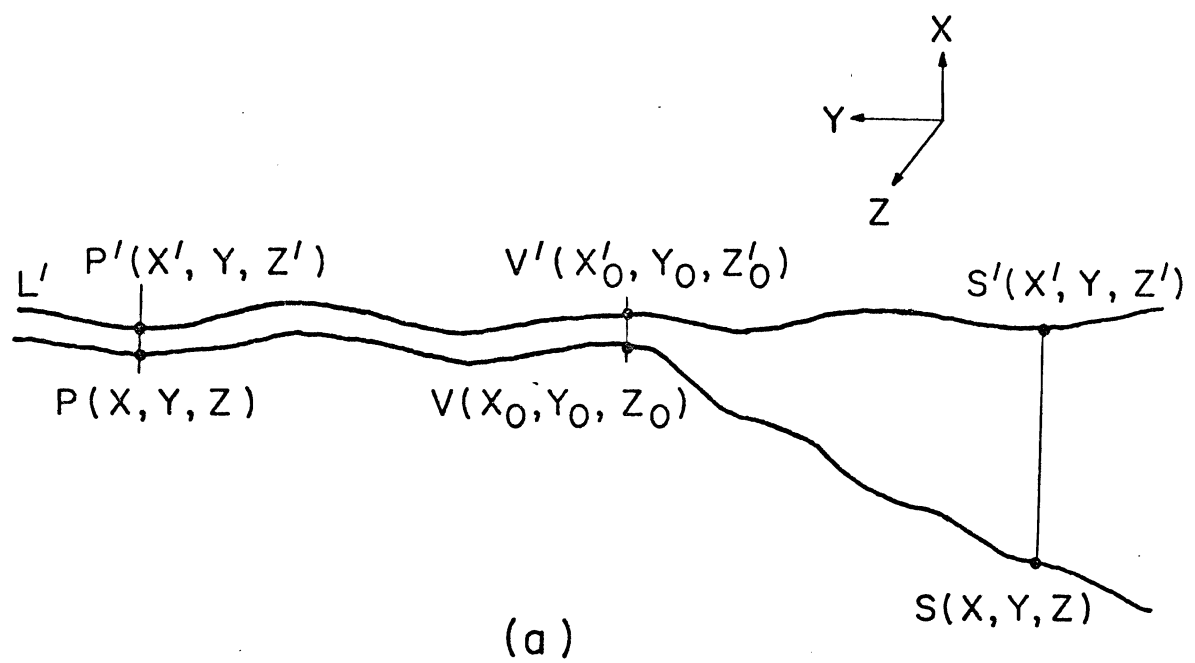
while the new coordinate for the vertex is $(0, y_0, 0)$. (See Figure 2(b).)

After the transformation, the dip angle of the primary and the deflection angle of the tracks from the

FIGURE 2.

The double measurement of tracks in the region where emulsion is very curved:

- (a) measured with a reference track L' ;
- (b) after transform to a new frame where L' is considered as a coordinate.



primary can also be derived from the formula described in part (A).

APPENDIX II:
SCANNING EFFICIENCY

This method of estimating scanning efficiency is based on the assumption that all the events inside the scanned region can be detected with the same probability in a specific scanning.

Let $P(P^*)$ be the probability of being found for each event in the first scanning (rescanning), and N be the true total number of events existing in the region concerned. We have

$$(A) \quad \left\{ \begin{array}{l} n_f = NP \quad \text{where} \\ n_m = N(1-P) \\ \Delta_{12}n = N(1-P)P^* \end{array} \right. \quad \begin{array}{l} n_f = \text{number of events} \\ \text{found in the first} \\ \text{scanning;} \\ n_m = \text{number of events} \\ \text{missed in the first} \\ \text{scanning; and} \\ \Delta_{12}n = \text{number of events missed in the} \\ \text{first scanning but found in the} \\ \text{rescanning.} \end{array}$$

Similarly, with the rescanning (asterisk superscripted) we have

$$(B) \left\{ \begin{array}{l} n_f^* = NP^* \\ n_m^* = N(1-P^*) \\ \Delta_{21}n^* = N(1-P^*)P \end{array} \right. \quad \begin{array}{l} \text{where } \Delta_{21}n^* = \text{number of} \\ \text{events missed in the} \\ \text{rescanning but found in} \\ \text{the first scanning.} \end{array}$$

From (A) and (B) it is trivial to derive

$$P = 1 - \frac{\Delta_{12}n}{n_f^*}$$

$$P = 1 - \frac{\Delta_{21}n}{n_f}$$

VITA

Myau-Yin (Phyllis) Lee [REDACTED]

[REDACTED] [REDACTED]

[REDACTED]. She [REDACTED]

[REDACTED] [REDACTED] received a B. S. degree from National Tsing Hua University, Hsinchu, Taiwan, in 1972. In the same year, she entered the United States and continued her studies in the graduate school of the University of Washington, Seattle.. [REDACTED] [REDACTED]

[REDACTED] [REDACTED]